5-1993

Internal Deformation, Evolution, and Fluid Flow in Basement-Involved Thrust Faults, Northwestern Wyoming

James V. Goddard

INTERNAL DEFORMATION, EVOLUTION, AND FLUID FLOW IN BASEMENT-INVOLVED THRUST FAULTS, NORTHWESTERN WYOMING

By

James V. Goddard

A thesis submitted in partial fulfillment
of the requirements for the degree

of

MASTER OF SCIENCE

in

Geology

Approved:

UTAH STATE UNIVERSITY
Logan, Utah

1993

ACKNOWLEDGMENTS

I extend most thanks and appreciation to Dr. James P. Evans for his inexhaustible resources, advice, patience, encouragement, and friendship throughout my graduate and undergraduate life. For providing many helpful and insightful suggestions with the research and the manuscript, I must also give much thanks to Dr. Craig B. Forster. Dr. Pete Kolesar and Dr. Tom Lachmar deserve my gratitude for reviewing this work and providing helpful suggestions. To Suzanne Astle, Clint Brown, Kelly Davis, and Darron Hinton, I extend my gratitude for their assistance in the laboratory and field. To my office mates, Clint Brown, Brain Hammond, and Dan Kendrick, I thank you for keeping me on my toes and adding a little levity during the course of my thesis work.

The food on my family's table and this research project were funded, through the kindness of Dr. Evans, by the National Science Foundation grant #EAR-9005087. Stipends from the Seely-Hinckley scholarship and a geology department fellowship also provided support.

To my patient and helpful wife, Tonya, I thank you for putting up with me and poverty while I finished school, and for providing me with constant incentive and motivation to finish my degree. Lastly, I thank my supportive parents for a proper, old-fashioned upbringing that instilled within me morals, work ethic, and the realization that I can do anything I want if I only put my mind to it.

CONTENTS

LIST OF TABLES

LIST OF FIGURES

Figure

ABSTRACT

Internal Deformation, Evolution, and Fluid Flow
in Basement-Involved Thrust Faults,
Northwestern Wyoming

by

James V. Goddard, Master of Science
Utah State University, 1993

Major Professor: Dr. James P. Evans
Department: Geology

An integrated field, microstructure, fracture statistic, geochemistry, and laboratory permeability study of the East Fork and White Rock fault zones, of similar age and tectonic regime but different structural level and hydrogeologic history, provides detailed information about the internal deformation and fluid flow processes in fault zones. The primary conclusions of this research are: 1) Fault zones can be separated into subzones of protolith, damaged zone, and gouge/cataclasite, based on physical morphology and permeability structure. At deep structural levels, gouge/cataclasite zones are more evolved (thicker with increased grain size reduction) due to strain localization, higher pressure and temperature, and fluid/rock interaction; 2) Deformation mechanisms evolved from primarily brittle fracturing and faulting in the damaged zone to extreme, fluid-enhanced chemical breakdown and cataclasis which localized strain in the fault core. Deformation in the deep-level-fault core may be a combination of frictional and quasi-plastic mechanisms, and is largely controlled by extremely fine-grained clays, zeolites, and other phyllosilicates that may have acted as a thermally pressurized, fluid-saturated lubricant; 3) Permeability in fault zones was temporally heterogeneous and anisotropic (permeability of damaged zone>protolith>gouge/cataclasite, permeability along fault> permeability across fault); 4) Volume loss was concentrated in the fault cores and was negligible at intermediate structural

levels and high at deep structural levels in the semi-brittle to brittle regime; 5) Fluid flow and solute transport were concentrated upwards and subparallel to the fault in the damaged zone; 6) Faults at both the local and regional scale acted as fluid flow conduit/barrier systems depending upon the evolutionary stage and interval in the seismic cycle; 7) Fluid/rock volume ratios, fluid flux, and fluid/rock volume ratios over time ranged from $\approx 10^3$ to 10^4, 10^{-6} ms^{-1} to 10^{-9} ms^{-1}, and 0.05 L/m^3 rock•yr to 0.50 L/m^3 rock•yr, respectively, suggesting that enormous quantities of fluids passed through the fault zones; 8) Box counting fractal analyses of fault zone fractures showed that fracture spatial and density distribution is scale-invariant at the separate scales of outcrop, hand-sample, and thin section, but self-affine from outcrop to thin-section scale; 9) Linear fractal analysis depicts clustering and density distribution as a function of orientation, and may be a quick, robust method of estimating two-dimensional fracture permeability; and 10) Fractal analysis of fractures is not a comprehensive statistical method, but can be used as another supplemental statistical parameter.

(155 pages)

INTRODUCTION

Understanding the influence of fluids and fluid circulation in the upper crust has long been problematic when describing structural and tectonic processes. Specifically, how do fluids affect the deformation, evolution, and propagation of fault zones in the shallow crust? Fluids likely penetrate and infuence the development of high angle normal faults and deep-rooted, low angle detachment faults (Reynolds & Lister 1987, Bruhn *et al.* 1990, Parry & Bruhn 1990, Glazner & Bartley 1991), reverse faults and thrust sheets (Sibson 1981, Engelder 1984, McCaig 1988, Sibson *et al.* 1988, Forster & Evans 1991), strike-slip faults (Sibson 1987, Chester & Logan 1986, Hickman 1991, Chester *et al.* 1993), regional metamorphism and ductile (mylonitic) shear zones (Kerrich 1986, Janecke & Evans 1988, O'Hara 1988, Sinha *et al.* 1988, Hanson 1992), and accretionary processes in active subduction zones (Moore 1989, Moore *et al.* 1991). Fluid circulation in crustal fault and shear zones likely affects the distribution of temperature, pressure (hydrostatic and lithostatic), and composition of deforming faults, which in turn influence the dominant deformation mechanisms and fault rheology. This could lead to weakening of fault-influenced rocks and localization of slip in fault zones, and subsequently increase the potential for seismic rupture (Bruhn *et al.* 1990, Parry & Bruhn 1990, Sibson 1991, Chester *et al.* 1991, Sibson 1992).

The distribution of vein, fault, and fracture systems associated with fault zones, to a large extent, controls the permeability structure of crystalline rocks in the upper crust (Sibson 1981, Barton *et al.* 1987, Bruhn & Yonkee 1988, McCaig 1988, Sibson *et al.* 1988, Barton & Hsieh 1989). Field, microstructural, geochemical, and stable isotope studies show that faults and shear zones may serve as pathways for focused fluid flow with the onset of pervasive, interconnected fracturing at micro- to map scale in an otherwise extremely low permeability protolith, or act as a fluid flow barrier when fault-related fractures are healed and/or sealed with vein deposits, or when very fine-grained fault products (e.g., gouge and cataclasite) inhibit fluid circulation (Chester & Logan 1986, Forster & Evans 1991, Chester *et al.* 1993). Fault zones are likely a combination

fluid flow conduit/barrier system that differs spatially and temporally during the life of the fault depending on the rate of fault evolution, internal morphology, and seismic history (Forster & Evans 1991, Sibson 1992).

Fluid circulation enhances deformation, dissolution, transport, and deposition of minerals in rocks within and adjacent to fault zones (Kerrich 1986, Evans 1990a). Fluids infiltrating fault zones often drastically change the style of deformation by altering the behavior and assemblage of minerals and the rates of chemical and mechanical processes during progressive deformation, e.g., cataclasis, mylonitization, solution transport, microfracturing, strain softening, dissolution, volume loss, thermal pressurization, hydrolytic weakening of feldspars, ductility of quartz, and recrystallization (Engelder 1984, Mitra 1984, Chester & Logan 1986, Sinha *et al.* 1986, Sibson 1987, Janecke & Evans 1988, Losh 1989, O'Hara & Blackburn 1989, Brantley *et al.* 1990, Evans 1990a, Glazner & Bartley 1991, Chester *et al.* 1993). Petrologic, geochemical, and isotopic studies of fault and shear zones mostly in regional metamorphism and mylonitic shear zones indicate the potential for very high water-rock ratios (10^1 - 10^4) and large fluid-related rock volume loss (>70%) in fault zones during evolution (Mitra & Frost 1981, Engelder 1984, Mitra 1984, Grant 1986, Kerrich 1986, O'Hara 1988, Sinha *et al.* 1988, Losh 1989, O'Hara & Blackburn 1989, Glazner & Bartley 1991). These results suggest that extremely large volumes of fluid may have circulated through the fault system, subsequently altering the behavior of the fault. Potential sources for these fluids that influence faults and shear zones at depths ranging from a few kilometers to <10 kilometers include meteoric water, metamorphic fluid, connate fluid, sedimentary basin fluid, and upwelling hydrothermal fluid associated with plutonism (Engelder 1984, Kerrich 1986, Reynolds & Lister 1987, McCaig 1988, Forster & Evans 1991).

OBJECTIVES

The primary purpose of this research is to resolve the deformation and permeability history of selected Laramide-age basement rock-involved, dominantly brittle thrust fault zones in the Rocky Mountain foreland province. Precambrian granite and gneiss have been thrust over Paleozoic and Mesozoic sedimentary basins with slip occurring on moderately dipping thrust faults and steeply dipping reverse faults (Mitra 1984, Brown 1988, Evans in press).

The two faults analyzed were the White Rock thrust in the northwestern Wind River Range thrust system and the East Fork fault system in the Washakie Range thrust system in northwestern Wyoming (Fig. 1). These faults are ideal because they are simple structures with fairly well defined histories and contain abundant evidence for syntectonic fluid flow. Initial evidence of the presence of fluids includes: 1) syntectonically deposited, deformed, and faulted quartz, iron oxide, chlorite, and laumontite veins; 2) the abundance of clay and other phyllosilicates in the fault interior relative to the protolith wall rock.

Because rates and directions of fluid flow cannot easily be directly measured in active fault zones, detailed analyses of the paleohydrogeologic characteristics of exhumed fault zones can shed light on the influence of fluids on faults. Well-exposed, exhumed faults should provide a geologic record of the paleopermeability structure, physical extent of fluid-rock interaction, and fluid volume and flux. To accomplish these results, this project incorporates: 1) detailed field and statistical characterization of fault zone fracture and vein systems using both conventional and new fractal techniques to identify the likely fluid pathways within the fault zones; 2) fault zone petrology and microstructure to determine the fluid influence on mineral breakdown, solute transport, and deformation mechanisms; 3) X-ray diffraction and fluorescence geochemistry to delineate fault zone minerology, volume change, and fluid/rock ratios; and 4) *ex situ* laboratory permeability testing of fault rocks taken from different zones and orientations within the fault to determine the relative spatial permeability structure of the fault.

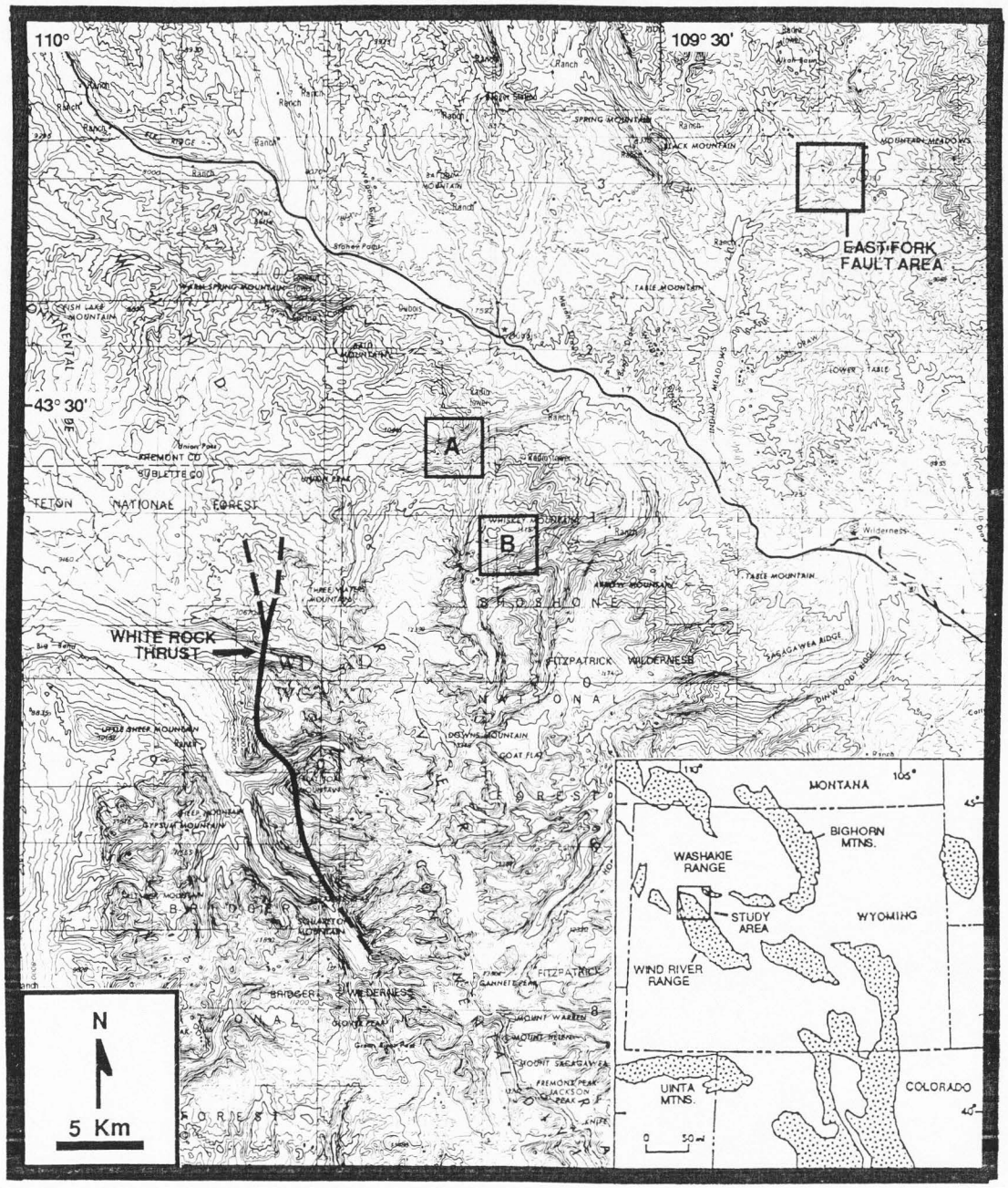

Fig. 1. Wyoming location map of the White Rock thrust and East Fork fault study areas. Map also shows location of DuBois (1990) (**A**) and Mitra & Frost (1981) (**B**) study areas. Stippled areas on inset map indicate mountain ranges associated with Laramide-age basement rock uplifts.

The specific goals of this project are:

1) Establish spatial and temporal characterization of fluid flow through fractures, veins, and faults at micro- to outcrop-scale.

2) Determine the influence of fluids on deformation mechanisms in mostly brittle faults.

3) Estimate bulk-rock volume losses associated with fault zone fluid flow.

4) Estimate the volumes of fluid that likely circulated through a fault zone and show how fluid flow may have varied spatially and temporally both within the fault zone and at different structural levels.

5) Obtain lab-derived permeability values of fault zone rocks to estimate the relative local permeability structure across a fault zone.

6) Integrate these results into a working physical model that characterizes fluid flow through brittle to semi-brittle fault zones at shallow crustal levels.

Previous studies deriving quantitative estimates of fluid circulation have dealt primarily with ductile deformation in mylonites. This study focuses on fluid flow estimates derived from brittle to semi-brittle fault zones.

LOCATION AND GEOLOGIC SETTING

Field work was concentrated in the northern Wind River Range thrust system and the Washakie Range thrust system in northwestern Wyoming (Fig. 1). Exposures of the White Rock thrust are located in the Bridger Wilderness area about 1.5 miles east of Green River Lakes in the northwestern tip of the Wind River Range in northwestern Wyoming. The major traces of the White Rock fault are located within the Green River Lakes 7.5' topographic quadrangle, Wyoming.

Outcrops of the East Fork fault system are located about 10 miles upstream on the East Fork of the Wind River in the Washakie Range of north central Wyoming. Specific field areas are

located within the Bain Draw 7.5' topographic quadrangle, Wyoming, R.5W, T7N, sections 5, 6, 7, and 8; and the Castle Rock 7.5' topographic quadrangle, Wyoming, R.5W, T.8N, section 32.

Southwest-directed faults in both areas evolved for ≈ 20 my during the late Cretaceous to early Eocene Laramide Orogeny and are located in the Rocky Mountain foreland province (Dickinson *et al.* 1988). Faults with small to large displacements (<5 meters to >10 kilometers) formed in Archean granite and gneiss (Mitra 1984, Evans in press). These areas were chosen for the excellent three-dimensional exposure of fault zones, which facilitated detailed mapping and sampling. In addition, the regional geology and structural geology are well-constrained (Mitra & Frost 1981, Mitra 1984, Evans 1987, Evans 1988, Mitra *et al.* 1988, Evans 1990a, Evans in press).

The Wind River Range and Washakie Range are part of the basement-involved Laramide Foreland of the Rocky Mountain Cordillera. The basement rock, primarily Precambrian granite and gneiss, was uplifted along large reverse faults during the Laramide Orogeny. The two major faults of the Wind River and Washakie thrust system are the Wind River fault and the EA faults (Mitra & Frost 1981, Mitra 1984, Mitra *et al.* 1988, Evans in press) (Fig. 2). The Wind River thrust is responsible for about 21 km of displacement and has placed Precambrian basement rocks atop Paleozoic and Mesozoic sediments of the Green River basin (Mitra 1984) (Figs. 2 & 3). The thrust sheet consists of a double plunging anticline that involves both basement and cover rocks and plunges to the north at the northern end of the Wind River Range and to the south at the southern end.

The EA thrusts, the major faults in the Washakie Range, place Precambrian granite and gneiss over Paleozoic and Mesozoic sedimentary rocks of the Wind River basin (Evans, in press) (Fig. 2). Both the EA and Wind River thrusts have few outcrops and are delineated primarily by seismic profile and drill hole data.

The White Rock thrust is a probable imbricate to the Wind River thrust (Mitra & Frost 1981, Mitra 1984, Mitra *et al.* 1988) (Fig. 3). Based on the offset of Paleozoic and Mesozoic

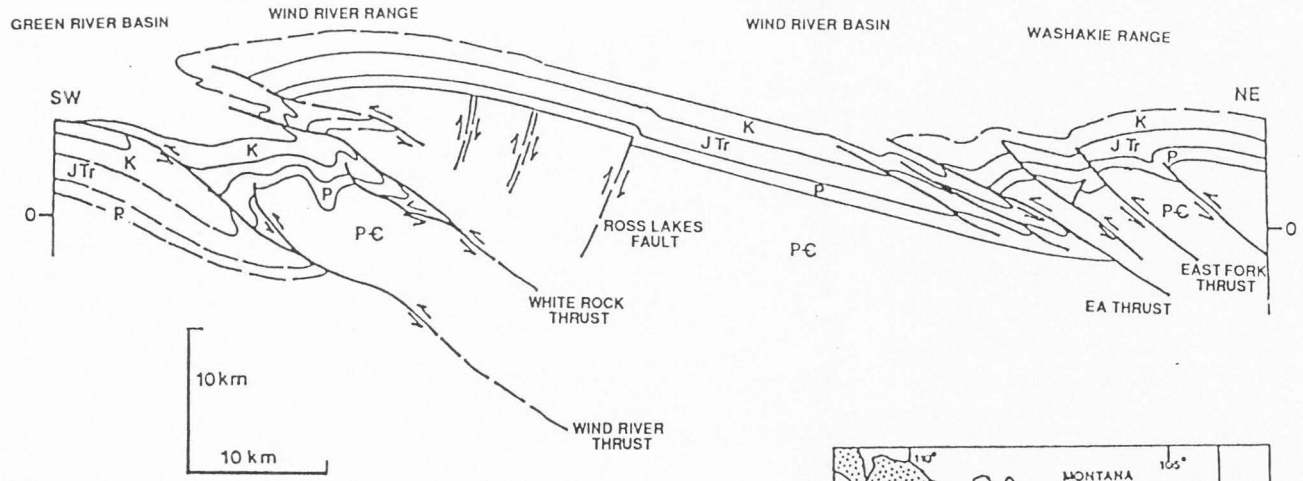

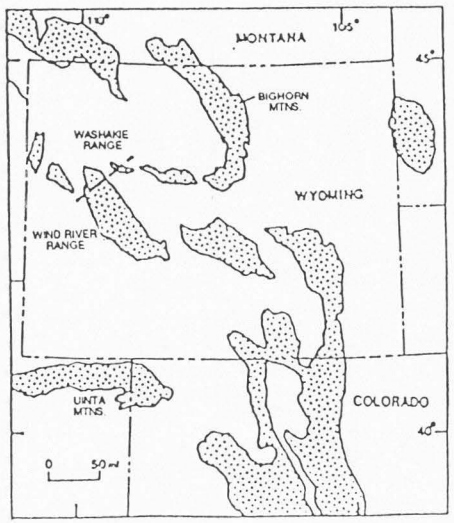

Fig. 2. Downplunge projection (looking north) of the northern part of the Wind River Range and the Washakie Range showing the relation between Paleozoic and Mesozoic cover and Precambrian rock uplifts. Rock units are: PC, Precambrian granite and gneiss; P, Paleozoic sedimentary rocks; JTr, Jurassic-Triassic sedimentary rocks; K, Cretaceous sedimentary rocks. Downplunge projection is based on Mitra (1984), DuBois (1990), Evans (in press), and projections done for this project. Approximate location of section line shown on inset index map. Work by DuBois (1990) and Mitra & Frost (1981) were located near the Ross Lakes fault area.

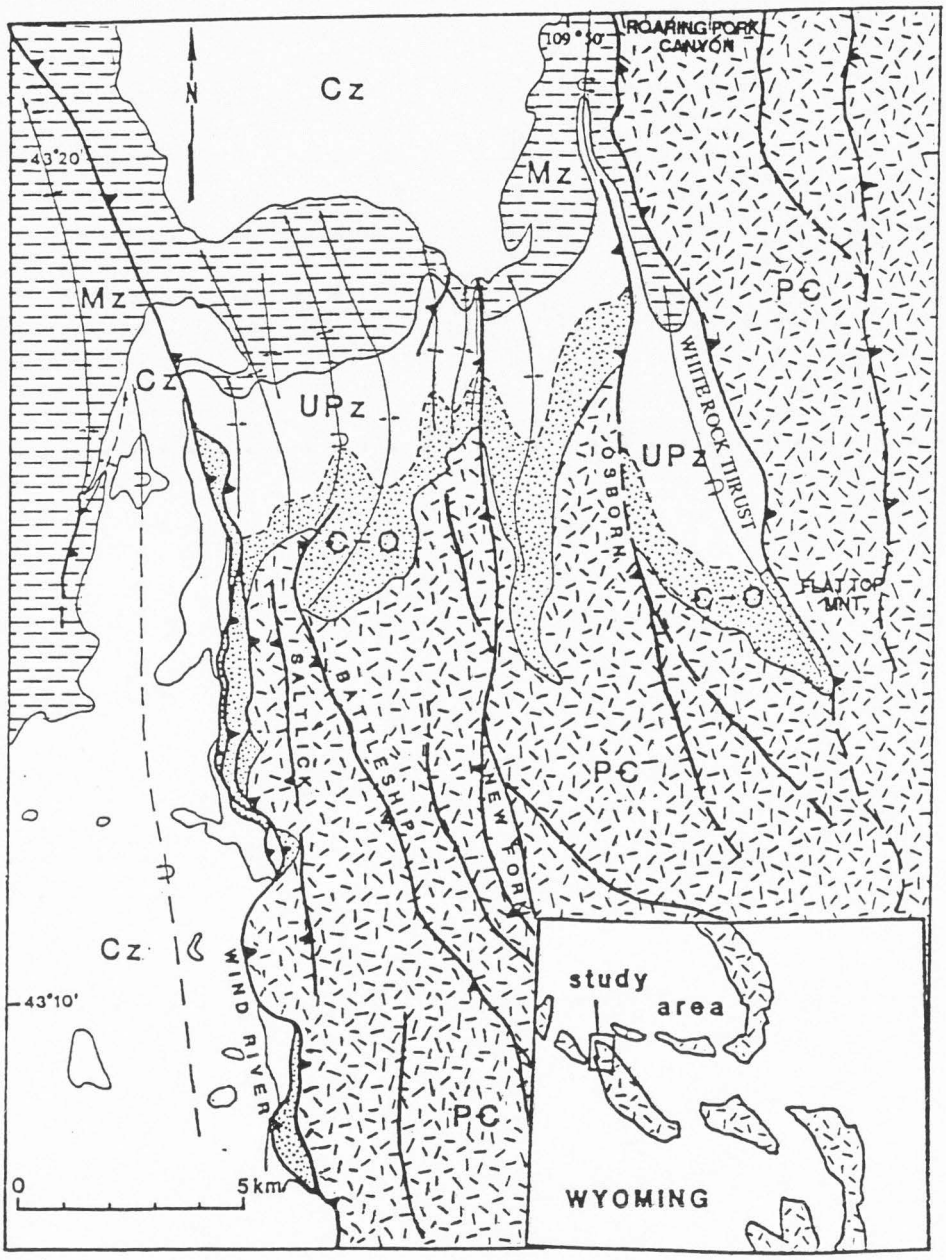

Fig. 3. Generalized geologic map of the White Rock thrust study area in the northwestern Wind River Range. Map shows major faults (Wind River and White Rock) and anastomosing shear zones (Osborn, New Fork, Battleship, Saltlick) within the Precambrian basement, and north-plunging folds (both upright and overturned) in the sedimentary cover (based on Richmond (1945)). Symbols: PC = Precambrian, C - O = Cambrian-Ordovician, UPz = Upper Paleozoic, Mz = Mesozoic, and Cz = Cenozoic. Field work was concentrated between Roaring Fork Canyon and Flat Top Mountain.

beds, the White Rock thrust has a displacement of about 8 km, and places Precambrian granitic basement atop overturned Paleozoic and Mesozoic sedimentary rocks (Fig. 4). Restored cross sections suggest that the fault had an overburden of 10 -12 km at the time the Precambrian basement rocks were breached in the Laramide Orogeny (Mitra 1984). The thickness of the cover rocks could have been less over the entire life of the thrust if the overriding thrust sheet experienced erosion during uplift. Evidence for fluid infiltration into this fault zone includes intense and extensive laumontite veins (Fig. 5), chlorite veins, and the syntectonic alteration of feldspars in the core of the fault to phyllosilicates, namely kaolinite, montmorillonite, and other clays. Because of the relative inaccessibility of this fault, research primarily involved field observations, microstructure, and geochemistry, with only minor fracture statistical analyses and no lab permeability testing.

The East Fork fault system is northeast of the EA thrusts (Fig. 6). Faulted and folded Archean granite and gneiss in the cores of large folds have been thrust 10-17 km southwest during the Laramide Orogeny (Evans 1990a). Exhumed fault zones in the East Fork area, based on restorable cross sections, formed at a depth of 6-10 km, and have basement granite and gneiss in both the footwall and hanging wall (Evans in press)(Fig. 7a). Preliminary evidence of fluid infiltration into this fault zone include folded and faulted quartz veins (Fig. 7a), iron-oxide-coated fractures, and syntectonically altered feldspars to phyllosilicates, namely kaolinite (Evans 1990a). Primary research on this fault includes fracture analysis, geochemistry, and lab permeability tests.

Aside from normal geothermal gradients and intra-fault friction, no other heat sources were likely present during fault evolution. Additional heat sources, i.e., magmatism, could increase fault zone temperatures and introduce up-welling fluids into the faults, which could further complicate calculations related to fluid circulation.

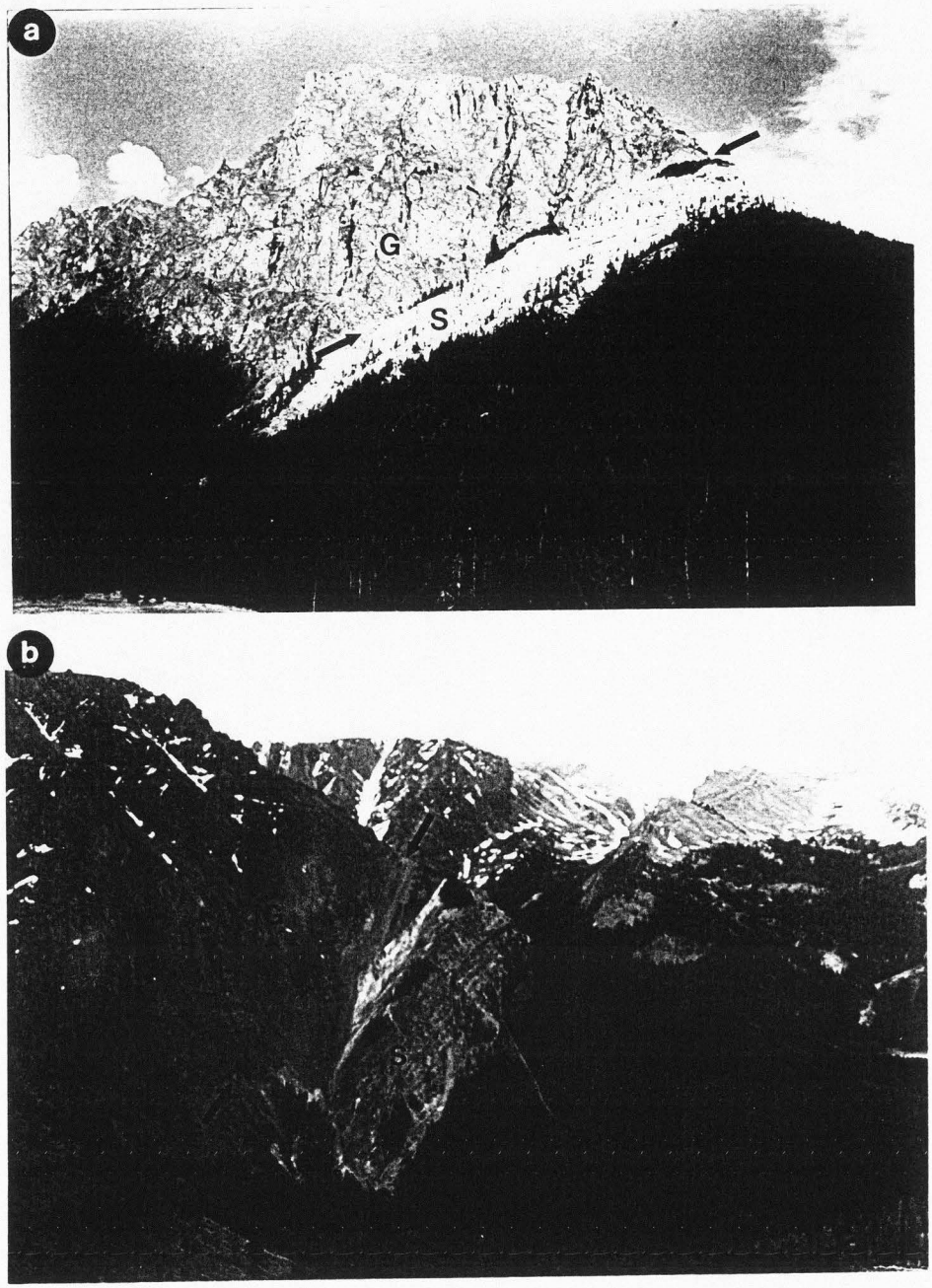

Fig. 4. Prominent exposure of the White Rock thrust in the northern end of the Wind River Range ≈ 2 km east of Green River Lakes. (**a**) View of the White Rock thrust (arrows) on Flat Top Mountain looking to the east. Precambrian granites (G) have been thrust to the southwest over Paleozoic and Mesozoic sedimentary rocks (S). (**b**) Same scene as (**a**) looking to the south across Clear Creek canyon.

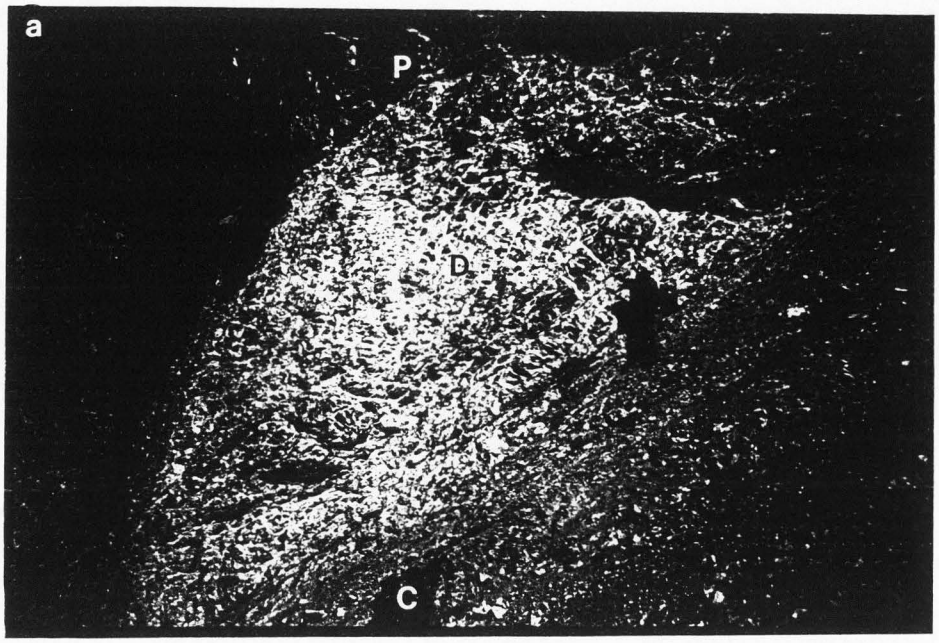

Fig. 5. Outcrop photographs illustrating evidence of syntectonic fluid flow in the White Rock fault zone. (**a**) Intricate network of white laumontite veins in the damaged zone (D) adjacent to protolith granite (P) and the fault core (C).View is approximately head-on to the fault. (**b**) Outcrop of damaged zone (D) with abundant, white, cross-cutting laumontite veins. Note sharp contact between damaged zone and relatively undeformed protolith granite (P). Most laumontite veins are at a shallow angle to the fault. The fault core is under feet in the talus slope. (**c**) Outcrop of subsidiary-faulted damaged zone showing intricate network of cross-cutting laumontite veins. Note hammer for scale.

Fig. 5. (continued).

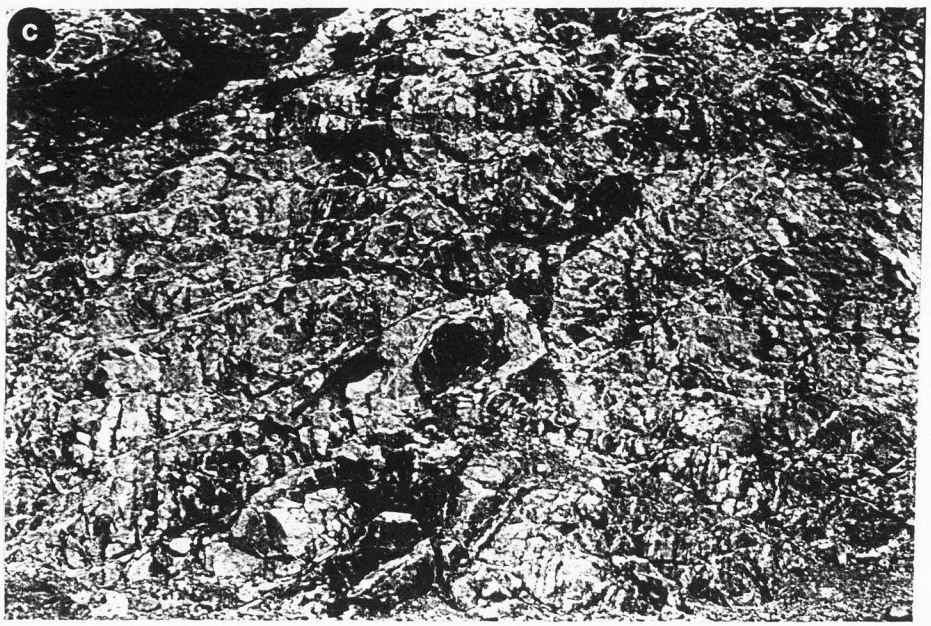

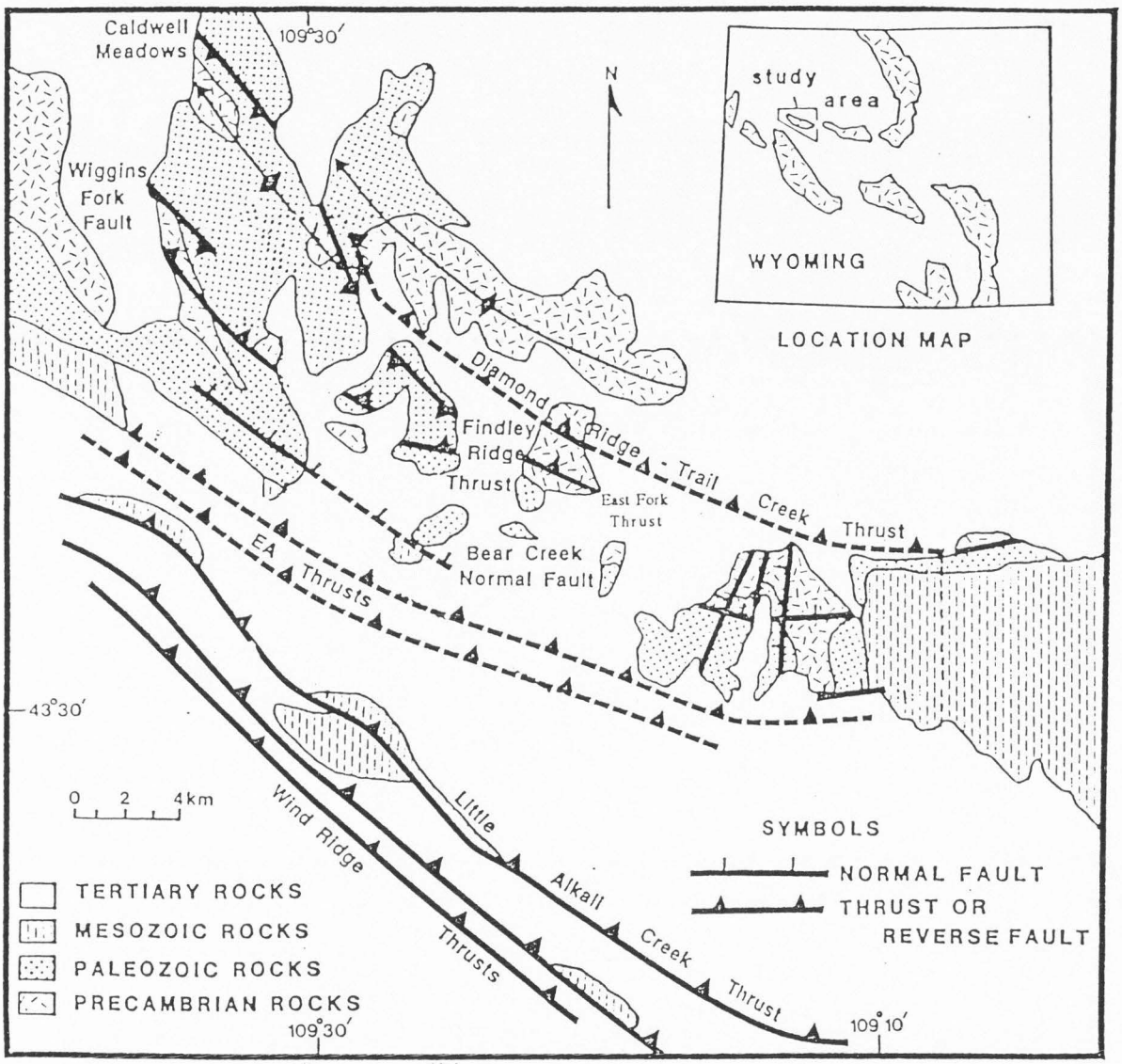

Fig. 6. Generalized geologic map showing the location of the East Fork study area (after Evans (in press)). Lower thrust sheet consists of Precambrian through Jurassic rocks thrusted to the southwest along the EA thrusts. The upper sheet consists of Precambrian and Paleozoic rocks thrusted to the southwest along the Diamond Ridge thrust. The East Fork faults (center) are exposed in Precambrian granites that have been incised by the East Fork of the Wind River and its tributaries.

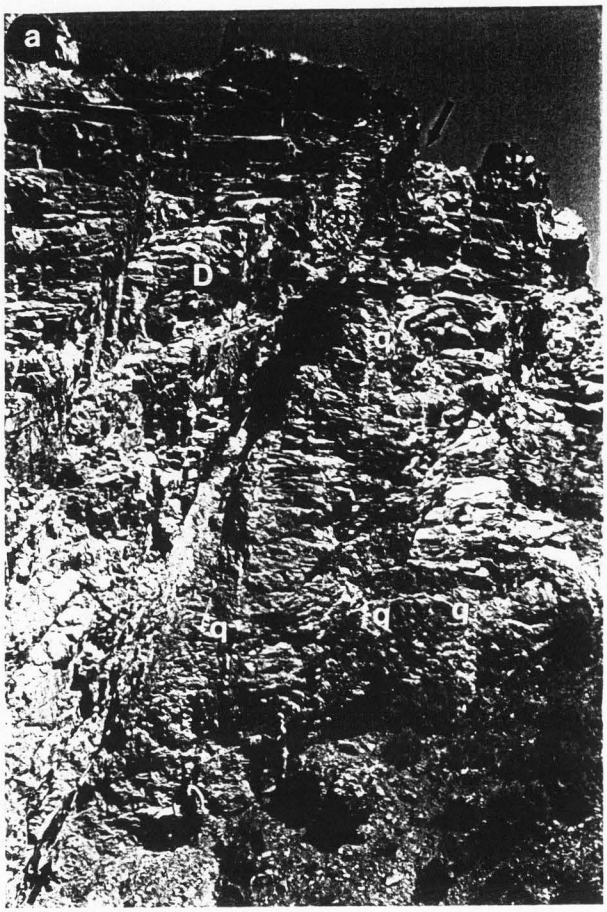

Fig. 7. Outcrop photographs showing faults found in the East Fork fault system. (**a**) Outcrop of a typical large-displacement fault zone showing gouge and cataclasite zone (arrows) bounded by adjacent damaged zones (D). Faults are bounded on both sides by Precambrian granite. View looking to the east. Sense of slip is top to the southwest. Note white, fault-sub-parallel to low angle, late stage quartz veins (q) in the damaged zone. (**b**) Zone of narrowly spaced, planar faults (arrows) in granite with top to the southwest sense of slip. View is to the east. These faults have well-preserved slickenlined fault surfaces. (**c**) East Fork large-displacement fault zone in granite showing a foliated gouge and cataclasite zone (G), large, fault-parallel quartz vein (q), and the adjacent damaged zones (D). Note the brecciated clasts (c) of gouge, cataclasite, and damaged zone floating in the large quartz vein (q). View is to the east. Sense of slip is top to the southwest. Note hammer for scale near the bottom of the large quartz vein.

Fig. 7. (continued).

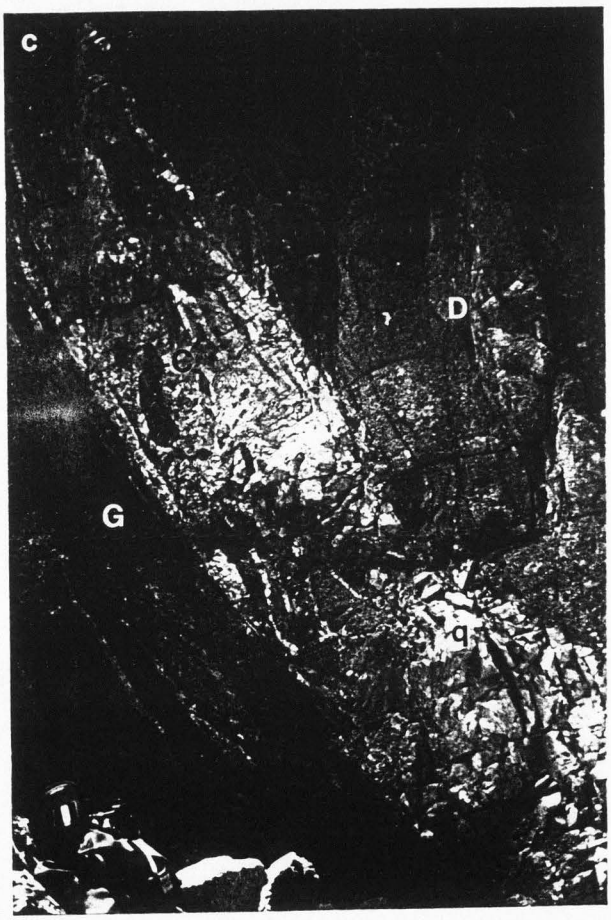

PREVIOUS WORK

Richmond (1945) mapped the geology around the Green River Lakes area, including the White Rock Thrust (Fig. 3). Several sets of anastomosing faults and shear zones were mapped that propagate through the Precambrian basement rocks and terminate into anticlines in the overlying sedimentary cover.

Mitra (1984) characterized the deformation mechanisms associated with the White Rock thrust based on fracture types dominant in the crystalline basement rocks. Mitra points out that grain size reduction led to eventually higher strains, and dislocation creep in later stages of the fault led to strain softening, allowing large displacements to be accommodated along narrow zones of high strain. Subsequent research on the White Rock thrust found in this paper compliments the work of Mitra (1984) by adding additional findings from field mapping, petrographic studies, and geochemical analyses.

Mitra *et al.* (1988) discussed the type of deformation in the Wind River Range, showing that large folds in the cover sedimentary rocks are directly related to major deformation zones in the Precambrian basement rocks. Basement deformation is characterized by localized strain softening (from cataclasis and diffusional creep) in narrow zones, while internally the basement blocks bounded by these narrow zones were deformed by fracturing and faulting.

Mitra and Frost (1981) described three different episodes of deformation present in the Precambrian rocks of the Wind River uplift. Two Precambrian ductile deformation events were characterized by recrystallized mylonite zones and chlorite- and actinolite-rich zones of greenschist retrogression. The third and youngest episode formed under Laramide-age zeolite facies metamorphism and is characterized by brittle faulting, fracturing, granulation, and mineral alteration in the presence of small amounts of fluid. At least seven sets of Laramide deformation zones were delineated within the basement rocks which may have accommodated approximately 10% shortening.

DuBois (1990) describes the Laramide deformation and paleohydrogeologic flow patterns in steeply dipping, shallow-level faults near Ross Lakes in the northeastern Wind River Range, Wyoming, between the White Rock thrust and East Fork faults (Fig. 2). He characterizes Laramide deformation as mostly brittle as defined by zones of cataclasis and intense fracturing that, at some locations, has reactivated Precambrian chlorite-rich mylonite zones. At least two episodes of fluid flow were determined based on the cross-cutting relationships and compositional variation of vein sets. Additional evidence for Laramide fluid flow is abundant fracture porosity, advanced feldspar alteration, and kaolinite development.

Dickinson *et al.* (1988) discussed the types, ages, and extents of sedimentary basins derived from Laramide uplifts. Based on these studies, inception and termination of deformation in the Wind River and Washakie uplifts occurred about 70 my to 50 my ago, respectively.

Evans (1988, 1990a) conducted detailed microstructural analyses on the East Fork Fault granites and determined that feldspar grains were weaker than quartz grains at temperatures below 325°C and at depths shallower than 8 km. Feldspars deformed extensively, fracturing along cleavage planes during grain-size reduction. Eventually, feldspars altered to kaolinite. Quartz deformed by brittle fracturing and eventually formed irregularly shaped pods of fractured quartz grains floating in a feldspar and clay matrix. Foliation developed along high-strain weak zones. Cataclasis is the dominant deformation mechanism in quartzo-feldspathic rocks at shallow crustal level. Evidence for fluid interaction in these rocks includes syntectonic alteration of feldspars to clays, the presence of iron oxides, and late stage faulted and folded quartz veins.

Evans (in press) described the geology, deformation mechanisms, and kinematics in the Washakie Thrust system. The leading edge of the thrust system collapsed from normal faults. Deformation of Precambrian rocks occurred by slip along faults and zones of cataclasis which dip northeast or by steep southwest-dipping antithetic faults. These faults bound relatively undeformed and intact blocks of basement rock. Initially, broad folds formed in the system, then

subsequent slip cut the limb of the Precambrian-cored fold to translate the thrust sheet southwest over sedimentary rocks in the Wind River Basin.

Forster & Evans (1991) present a preliminary compilation of field observations, laboratory permeability tests, and fluid-flow modeling studies of the paleohydrology of the East Fork Fault system in an effort to estimate the permeability of faults and the affect that fault permeability structure has on regional fluid flow. Faults in the East Fork fault system consist of low permeability gouge zones adjacent to a higher permeability damaged and fractured zone. Lab tests of cores of different zones in the fault showed a difference in permeability of two orders of magnitude between the gouge zone and the damaged zone. In addition, permeability was maximum parallel to the plane of the fault and least perpendicular to the plane of the fault. Regional modeling based on a throughgoing thrust fault, footwall sedimentary rocks, and a crystalline thrust sheet showed that the bulk permeability of a fault zone can strongly influence the regional-scale fluid flow, pressure, and thermal regimes. Local variations in fault zone permeability influence fluid transit times, but have little overall affect on regional-scale distribution of temperature and pore pressure.

In order to discriminate brittle to semi-brittle Laramide deformation found in the study areas, it is important to note that Precambrian deformation is primarily ductile, consisting of chlorite-rich zones of mylonite and and other regions of recrystallization (Mitra & Frost 1981, DuBois 1990), and Laramide deformation occurred at much lower temperatures and pressures and is primarily brittle to semi-brittle, consisting of brittle faulting and fracturing with associated cataclasis (Mitra & Frost 1981, Mitra 1984, DuBois 1990, Evans 1990a).

METHODS

FIELD WORK

Field work involved micro-to outcrop-scale mapping of well exposed, representative areas within the East Fork and White Rock fault zones. Detailed mapping along traverses perpendicular to faults allowed for better characterization of the distribution of structural and hydrogeologic properties within the fault zones. Outcrop-scale mapping of the distribution of fractures, veins, and faults that acted as likely fluid pathways during fault evolution was accomplished by rough sketch, mapping from 1 m x 1 m grid (10-cm cells), and mapping from enlarged photographs. Oriented samples were collected for subsequent hand-sample-scale fracture mapping, thin-section analysis, geochemistry, and lab analysis of fault rock permeability. Because of the remote locality of the White Rock thrust, samples suitable for lab permeability tests were not acquired.

Field work allowed for the macroscopic characterization of: 1) the hydraulically important fracture and vein distributions along the faults; 2) orientation and temporal cross-cutting relationships of faults, fractures, and veins; 3) vein fillings; 4) the variation in fault size and internal character along strike and structural level; and 5) the distribution and volume of alteration products. The purpose of detailed mapping of fault zones is not to map every crack in and around the fault, but to sample and map such that representative zones in the fault can be characterized.

MICROSTRUCTURE

Because microstructural analyses on the East Fork fault zone rocks have previously been done by Evans (1988, 1990a, in press), only the White Rock fault was microstructurally characterized. Using standard methods, 70 oriented thin sections (7.6 cm x 2.5 cm & 4.6 cm x 2.5 cm) were made from oriented samples taken from the White Rock thrust. Frequently, the

sample preparation consisted of impregnation with epoxy because of the incohesive or brittle nature of the fault-related rocks. In order to adequately characterize the different fault-related foliations and microstructures, thin-sections were oriented perpendicular to the fault plane, and either parallel or perpendicular to the primary slip direction of the fault (top to southwest) (see Fig. 8 for sampling scheme). Directed and reflected light optical microscopy was used to determine the extent of fluid interaction with dominant deformation mechanisms and fault rheology. Specifically, thin sections were used to illustrate: 1) the gradational change of deformation types from protolith to fault core; 2) fault mineralogy and texture; 3) fracture type; and 4) vein systems and their cross-cutting relationships.

FRACTURE ANALYSES

The contribution of fracture networks to fluid flow and the physical properties of rock is not a function of the fractures at any one particular scale, but rather the sum of the contribution of fractures at all scales (Barton *et al.* 1991). Different scales are likely more important than others depending upon the type of fluid interaction taking place. For instance, fluid flow and solute transport are likely greater through large fractures at the macroscopic scale, while fluid/rock reactivity is likely greatest in small, dense fractures at the microscopic scale. Several factors, including the amount and degree of fracture interconnection, dominant orientations, density, clustering, and aperture, strongly affect, and may even dominate, both rock mass permeability and fluid/rock reactivity in many cases (LaPointe 1988, Barton & Hsieh 1989). Scale variation and spatial clustering leads to patches of high and low hydraulic conductivity. Dead-end fracture traces contribute to the fluid storage capacity and fluid/rock chemical reactivity of the network, but do not allow for fluid flow across the network. Hence, accurate characterization of fracture parameters is vital. In addition to this general goal, specific objectives of this research are to: 1) characterize fracture "filledness" (i.e., the way in which fractures fill space) and clustering; 2) characterize the complexity of a fracture network that may otherwise become washed out using

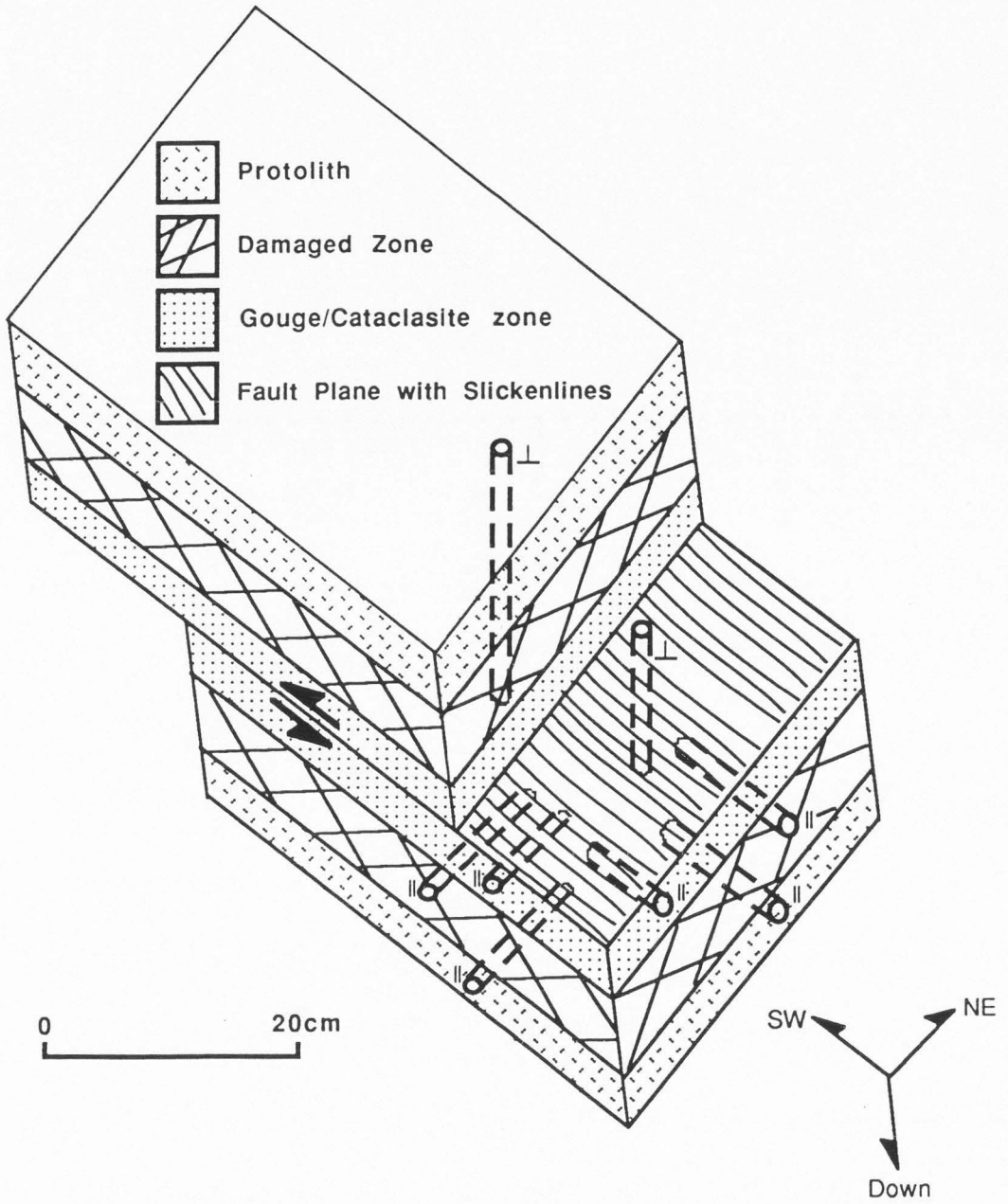

Fig. 8. Simplified block diagram of a typical fault zone depicting a typical progression from protolith to damaged zone to gouge/cataclasite zone. Depending upon the size of the fault, the scale of diagram could be from map to microscale. Faces of the block diagram illustrate the typical orientations of both thin sections and fracture trace maps relative to the fault plane and slip direction. Diagram also illustrates the typical sampling scheme used when removing core for permeability testing. Cores (dashed tubes) were extracted from the protolith, damaged zone, and gouge/cataclasite zone at angles either perpendicular (⊥) (long axis of the core is perpendicular to the fault plane) to the fault plane or parallel (||) to the fault plane.

conventional statistics; 3) attempt to determine if sampling and characterization at one scale can be extrapolated to other scales; and 4) develop additional fracture parameters for input into numerical models. This may bring synthetically generated fracture networks closer to resembling natural fracture networks by adding another constraint to the modeling process.

Because of the excellent accessibility of the East Fork area, we collected ≈ 30 oriented samples up to 50 cm x 50 cm for fracture analysis. Fracture and vein networks, traced from oriented (in the same manner as thin sections, see Fig. 8) outcrop photos, slabbed hand-sample faces, and enlarged photonegatives of thin sections taken from undeformed protolith, fractured (damaged) zone, and gouge and cataclasite zones, were meticulously mapped, digitized, and subjected to conventional fracture statistics and fractal analysis. Conventional statistical analyses consisted of histograms that depict the distribution of fracture trace length and orientation (Howard & Nolen-Hoeksema 1990, Goddard & Evans 1991). This was accomplished using FAS, Fracture Analysis Systems, a digitizing and fracture statistics program developed by Joseph V. Gardner. Also, digitized fracture data were transferred to the spreadsheet programs of QuatroPro and Kaleidagraph, and histograms depicting fracture length and orientation distributions were generated.

Fractal Geometry

Fractal analysis, using the box counting method (LaPointe 1988, Barton & Hsieh 1989, Goddard & Evans 1991) and the Cantor dust method (Velde *et al.* 1990, Goddard & Evans 1991), are used to test and characterize: 1) fracture network self-similarity or scale-invariance; 2) the directional nature of the fractal dimension; 3) the spatial distribution of a fracture network; and 4) interconnectivity of fractures, veins, and faults.

Fractal analysis is a branch of mathematics that has been used to quantify complex geologic patterns in nature (Mandelbrot 1982, Feder 1988). The basic concept of fractal analysis is that: 1) a phenomenon (in this case, fractures) will retain the same characteristics at different scales in the same manner (scale-invariant or self-similar), thus rises the need for geologists to

use a scale (hammer or ruler) so as to avoid misinterpretation of the scale of a geologic photo; and 2) a phenomenon will sustain distinct characteristics in the way in which it "fills" space. For example, a straight line drawn on a piece of paper fills a page differently than a chaotic, irregular curve. The major descriptive variable in fractal geometry is the fractal dimension, which is used as a measure of the scaling and "filledness" of the phenomenon. Fractal (derived from the word fractional) is a term devised by Mandelbrot (1982) for describing the geometric properties of irregular fragments. Conventional Euclidean notions of dimension describe objects in Cartesian space using discrete integer dimensions, i.e., a point has the integer dimension of 0, a line has a dimension of 1, a square on a plane a dimension of 2, and a solid cube the dimension of 3. However, irregular natural phenomena rarely possess integer dimensions, but rather possess fractional dimensions that fall somewhere between these integer values. Fractal geometry is a means to measure fractional dimensions.

The fractal dimension is a function of the geometric dimensions in which the analysis is projected. Volume analysis (3-D) of irregular events gives fractal dimensions between 2 and 3, surface analyses (2-D) give dimensions between 1 and 2, a linear analysis (1-D) gives values between 0 and 1. If the irregular event is fractal, then the fractal dimension should arguably be the same in any projection, i.e., 0.5 in one dimension, 1.5 in two dimensions, and 2.5 in three dimensions (Feder 1988).

A fractal event occurs as a power of the dimension of observation (Mandelbrot 1982, Feder 1988):

$$N = R^{-D}, \qquad (1)$$

or equivalently,

$$D = \log N / \log(1/R), \qquad (2)$$

where **D** is the fractal dimension, **R** is the dimension, or scaling, of the measurement, and **N** is the number of occurrences of whatever is being measured, in this case, fractures. The fractal

dimension, **D**, is typically determined by plotting **N** against **(1/R)** in log-log space over several scales (Fig. 9). If a well-fit straight line (rule of thumb: $r^2 \geq 0.98$ (Barton & Hsieh 1989, Velde *et al.* 1990)) can be projected through the points on the plot, then the analysis describes a fractal distribution (or power law distribution in linear space). If the relation is a normal, or Gaussian, distribution, the points will describe a curve (Fig. 9). The present study uses several approaches of fractal analysis applied to the problem of describing fracture networks at the scale of thin section to outcrop, and is an initial attempt to illustrate possible practical uses of fractal analysis in the study of fractured rock.

Previous Fracture Fractal Work

Because fractal analysis of fractures is a relatively new and unexplored field, little previous work exists. Barton & Larsen (1985) studied outcrops and road cuts in a Miocene volcanic tuff unit at Yucca Mountain, Nevada. Fractures, ranging in length from 0.20 to 200 m, were subjected to a two-dimensional fractal box counting analysis. They reported scale invariant fractal dimensions over the scale of their observations. After reevaluating their data with improved techniques of box counting, they calculated fractal dimensions ranging from 1.6 to 1.7 (Barton & Hsieh 1989, Barton *et al.* 1991).

LaPointe (1988) presented a method to compute an index of fracture density using fractal geometry. The box-density method evaluates the number of fractures per unit area of rock, then the unit area size is varied to determine the fractal nature. Fractal dimensions from this study ranged from 2.37 to 2.69. This method depicts the spatial and density distribution of a fracture network.

Chiles (1988) used the box counting method to analyze fracture patterns along mine drift walls in granite. He concluded that a combination of fractal and geostatistical models can be used to describe fractures in granites, but acknowledged that the fractal analysis technique he used has shortcomings and is very susceptible to both sampling and methodological errors. For example, he sampled fractures only over one order of magitude in the vertical direction, then

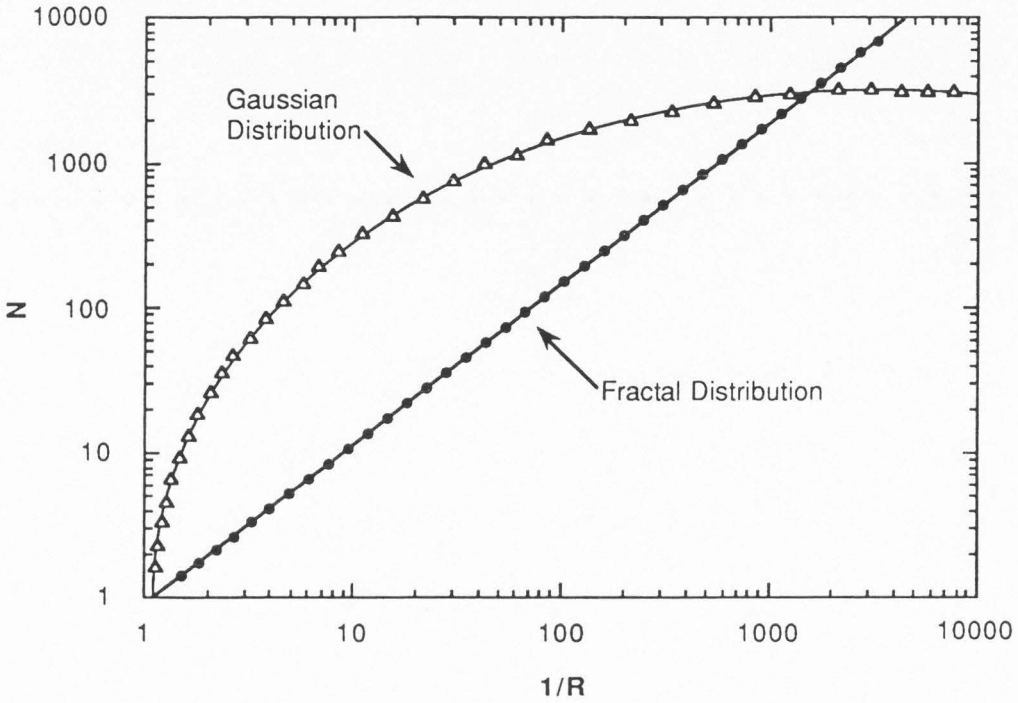

Fig. 9. Plot showing the contrast between a fractal distribution (straight) as opposed to a Gaussian or normal distribution (curved) in log-log space.

proceeded to use cell sizes smaller than the smallest fracture trace length, and he extrapolated his results over a scale larger than he observed (Barton *et al.* 1991), which inherently deceased the accuracy of the measurements.

Velde *et al.* (1990) and Velde *et al.* (1991) are the only previously published fractal analyses of fracture spacing along a linear sample. They measured the fractal dimension in terms of the probability of finding a fracture-free zone in the following length unit to be measured. In order to study the effect of anisotropy in fracture patterns, they measured line samples at various orientations on two-dimensional fracture-trace maps. The fractal dimension for a given fracture network varied by as much as 0.33 for the most anisotropic fracture networks. The range of fractal dimensions was 0.10 to 0.68. They conclude that fractures measured in their study were fractal and the fractal dimension varies as a function of orientation. Harris *et al.* (1991) criticized the linear method found in Velde *et al.* (1990), suggesting that the range of scales used to test the fractal nature of the fractures was inadequate, and that the method depicts the directionality of the fractal nature only in limited cases. Velde & Dubois (1991) agree with the comments of Harris *et al.* (1991) and indicate that they already remedied most of the shortcomings of the method in Velde *et al.* (1991).

Goddard & Evans (1991) studied the effect of different orientations relative to a fault zone on fracture statistics using conventional statistical methods and the box counting, box density, and a modified linear fractal analysis. They found that fractures examined were fractal and scale-invariant from thin-section to hand-sample scale. Also, fractal dimensions differed as a function of orientation of the face from which the fractures were mapped. The linear fractal analysis revealed that the fracture fractal dimension is anisotropic in that it varies with different azimuthal measurement directions. They concluded that a combination of statistics and fractal geometry can help to accurately describe the geometry, and spatial distribution of fractures over different scales.

Other studies on the fractal nature of fractures include Turcotte (1986), Vignes-Alder *et al.* (1991), Barton & Zoback (1992), Davy *et al.* (1992), and Matsumoto *et al.* (1992).

Fractal Analyses

Determination of the three-dimensional fractal dimension could be made if a complete surveying of fractures were possible. But here, data are limited to two-dimensional fracture surveys of outcrop faces, slabbed hand-sample faces, and thin sections.

Fracture trace maps used for conventional statistical analyses were also used for fractal analyses. Fractal analyses were originally produced by hand, then when the technique was tested and improved, the maps were digitized using FRAX, a program developed for numerical fracture fluid flow modeling by Mark Hulik and Craig Forster. The digitized data from FRAX were then input into CANTD, a linear fractal analysis program developed by the author and encoded in FORTRAN by Dr. Craig Forster.

To test the usefulness of different fractal methods in describing fracture distributions, this study incorporates two fractal box counting methods as described by LaPointe (1988) Barton & Hsieh (1989), respectively, as well as a linear Cantor dust method as described by Velde *et al.* (1990) and Goddard & Evans (1991).

Two-dimensional fractal analyses

To help describe the two-dimensional spatial distribution of fractures, the box counting method was used (Barton & Hsieh 1989). The analysis is based on the power law equation:

$$N = R^{-D},$$

which can be simplified to:

$$D = \log N / \log(1/R),$$

in which **D** is the fractal dimension, **R** is the scale of observation (cell size), and **N** is the number of fracture events related to scale **R**. The technique involves superimposing square grids of various sized square cells over a fracture network (Fig. 10). The smallest cell size should be no

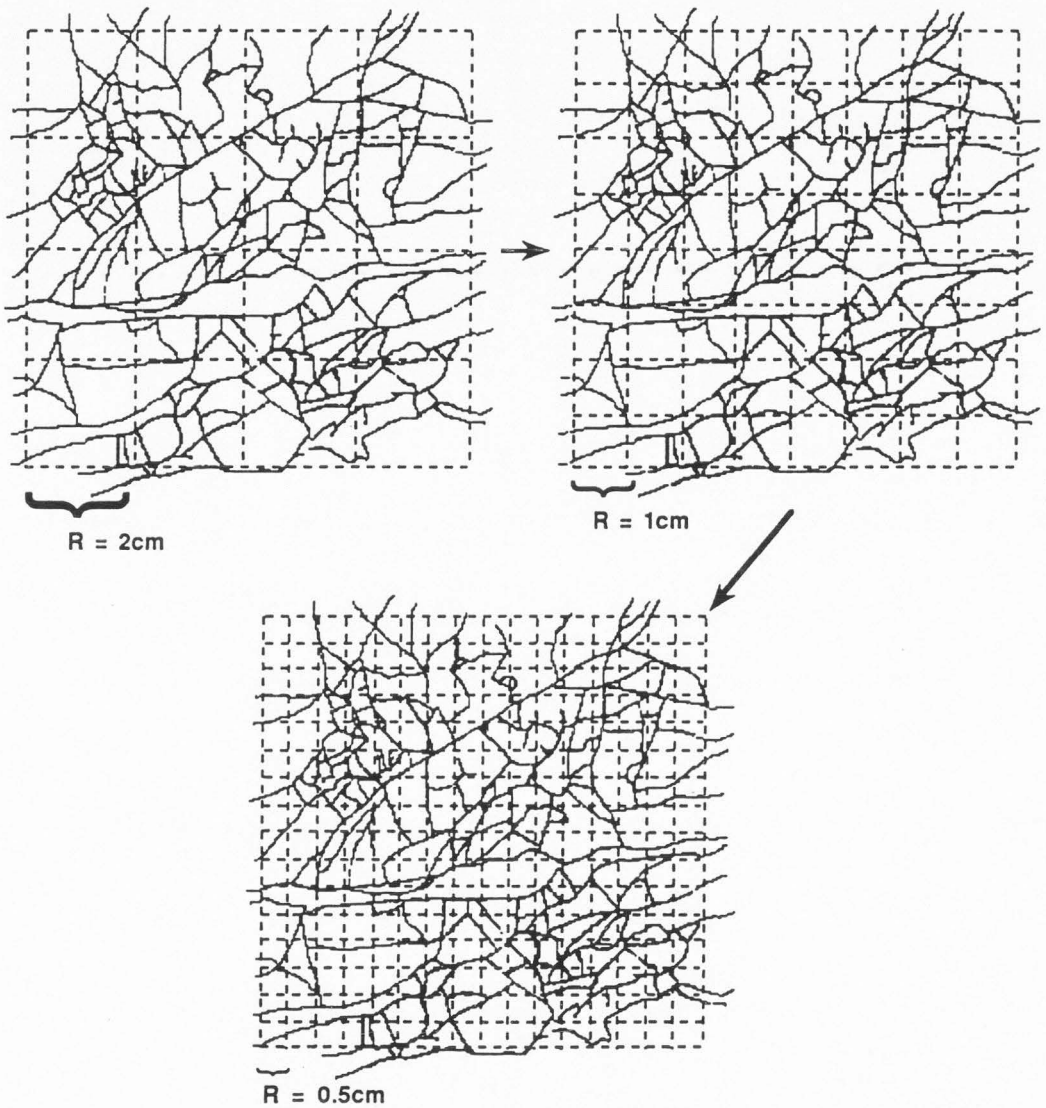

Fig. 10. Plot illustrating the manner in which a square grid is superposed onto a fracture trace map using the box counting method. The scale of grid (R) changes from 2 cm to 0.5 cm. Note that the grid is fully contained within the trace map.

smaller than the shortest fracture in the network (otherwise the scale of the method would be less than the scale of the fractures), while the largest cell size should be smaller than the size at which all cells are occupied (if all cells are filled, **N** simply describes the number of cells in the grid and not the filledness of the network). Barton & Hsieh (1989) suggest that the grid should be oriented such that for each cell, **N** is at a minimum. This is an unexplained convention used by Barton & Hsieh (1989) (see also Barton *et al.* 1991). To be consistent, the grid was oriented on planes illustrated in Fig. 8 such that a side of the square grid was parallel to the plane of the fault. The grid should also lie entirely within the fracture network. Using the Barton box counting method, **N** is the number of cells that contain, or are intersected by, at least one fracture (Barton & Hsieh 1989) (Fig. 11). Calculation of **N** using the LaPointe method is more involved (LaPointe 1988), but more completely measures both the fracture spatial and density distributions. The LaPointe box counting method uses a variation of the Barton box counting method in which the number of fractures contained within each cell is counted. The procedure involves overlaying a sequence of square grids of different cell size and counting the number of fractures in each occupied cell. For each cell size, the maximum number of fractures in one cell is divided by the number of cells on one side of the grid. This value is then used to normalize the data for each cell in the grid, such that the sum of the normalized count is stored as **N(R)** (Fig. 11). This procedure takes into account the number of fractures in a network. The fractal dimension is calculated using equations 1 and 2 where **N(R)** is in place of **N.** the value, **R**, for both methods is simply the length of a side of a cell in a grid.

Once **N** and **N(R)** are calculated over several cell sizes (**R**), **N** and **N(R)** are plotted against (**1/R**) in log-log space (Fig. 9). If the distribution of data points can be best fit by a straight line (r^2>0.98) of constant slope over the scale studied, then the distribution of fractures in that 2-D area is fractal and scale-invariant. The slope of the best fit line is the fractal dimension. The Barton method can produce fractal dimensions of 1<D<2, in that the procedure is characterizing the distribution of fractures between one- and two-dimensional space. The LaPointe method will

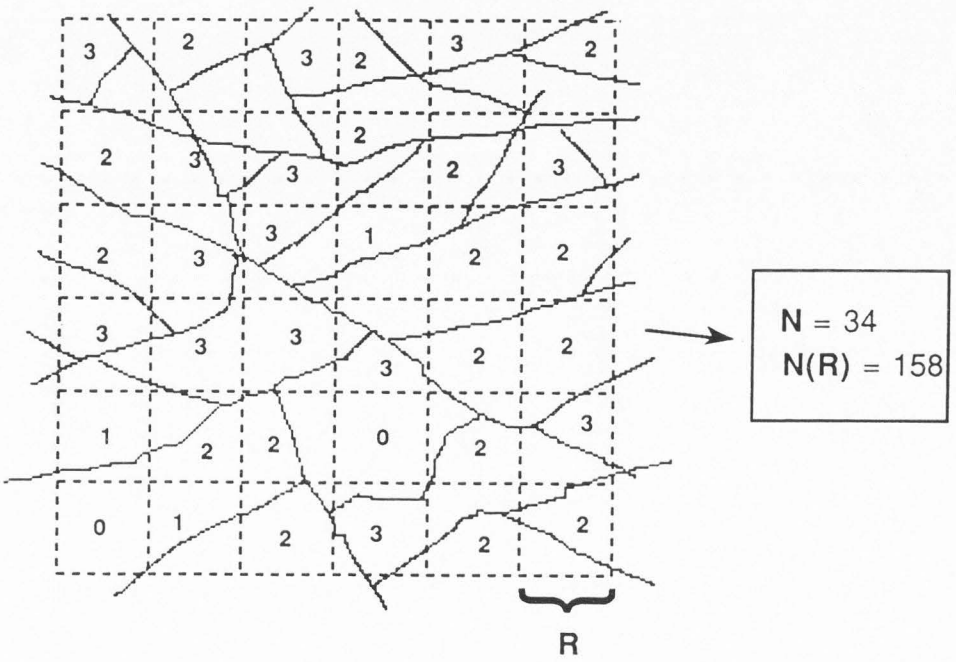

Fig. 11. Fracture trace map, overlaid with a grid of scale **R**, illustrating the difference between **N** of the Barton box counting method and **N(R)** of the LaPointe box counting method. N is simply the number of cells containing one or more fractures. **N(R)** is the value obtained based on the following steps: 1) counting the number of fractures within each cell; 2) normalizing by dividing the maximum number of fractures by the number of cells along one side of the grid, in this case 6/3 = 0.5; 3) then each cell is assigned a value based on this normalization such that a cell containing 3 fractures would be assigned a maximum of 6 (number of cell on a side), 2 fractures = 4, 1 fracture = 2; 4) the values for each cell are summed to give a value of **N(R)**. For this example, **N** = 34 and **N(R)** = 158.

produce fractal dimensions of $2<D<3$, in that the calculation of **N(R)** (using fracture quantity) ostensibly adds a third dimension by integrating fracture density. The Barton and LaPointe box counting methods provide fractal dimensions that seemingly quantify the spatial and density distributions of fractures. The actual physical meaning of the fractal dimension is yet unknown; however, comparison of dimensions of different networks can help to define possible significance.

Linear fractal analyses

The Cantor dust method (Velde *et al.* 1990, Goddard & Evans 1991) is applied using a linear analysis of a two-dimensional fracture trace map. The advantage of a linear analysis is that the analysis line can be oriented in different azimuths in the two-dimensional map in order to take into account the orientation contrast in the fracture pattern. Because fracture fluid flow is directional, it is convenient to describe the filledness with respect to orientation. The fractal equation used for the linear fractal analysis is similar to the LaPointe box counting equation such that:

$$\mathbf{D = \log N(X)/\log(1/X),} \qquad \mathbf{(3)}$$

where **D** is the fractal dimension describing the distribution of fractures along a segmented analysis line, **X** is the size (scale) of a line segment, **N(X)** is the normalized value describing the clustering of fractures along the segmented analysis line with respect to the scale (**X**).

The method is simple. A sampling line is superimposed onto a fracture trace map, divided into segments, and the number of fracture intersections occurring within each segment is recorded (Fig. 12, step 1). The length of the analysis segment is successively changed on the analysis line and the operation is repeated at each segment scale. We further analyze the directionality by rotating each line segment 180 degrees and at 20° to 30° intervals (Fig. 13) and the sequence of operations necessary to determine **N(X)** is recalculated over several cell sizes.

The linear analysis of **N(X)** is similar to the two-dimensional analysis of **N(R)** used by LaPointe (1988). The calculation involves the normalization of data to the line segment that

CALCULATION OF N(X)

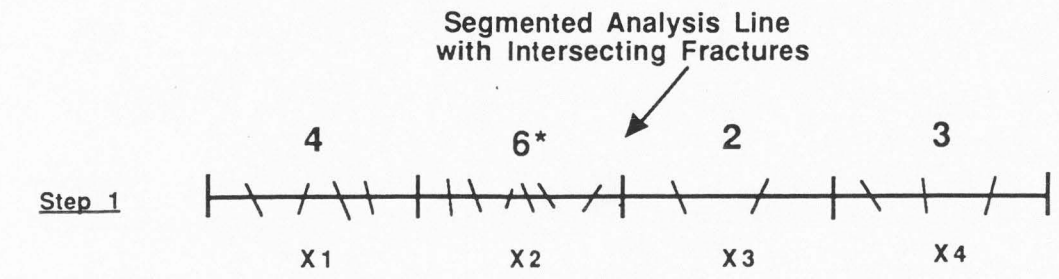

Step 2

$$\text{Y-SCALE INCREMENT} = \frac{\text{Maximum \# of fracture intersections}}{\text{\# of line segments}}$$

$$= 6/4$$

$$= 1.5$$

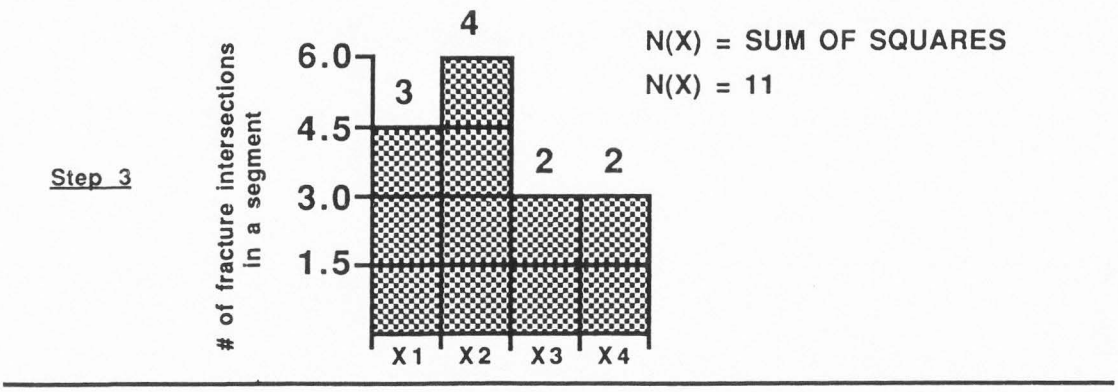

Step 4 **Repeat steps 1-3 over different line segement lengths.**

Fig. 12. Graphic illustrating the calculation of **N(X)** using the linear fractal analysis derived from this research. Step 1: First, the total number of fracture intersections are counted within each line segment. Step 2: the fracture sums are normalized to the line segment that contains the maximum number of fracture intersections. The normalization is simply the maximum number of fracture intersections within a line segment divided by the total number of line segments along the analysis line. Step 3: The one-dimensional data are then transferred to a two-dimensional representation, or histogram, in which the X-axis is proportional to the number of line segments and the Y-axis is the normalized number of fractures. Next, the number of fractures within each line segment is plotted on the histogram. This is accomplished by filling cells or squares on the histogram. A square is filled when the number of fracture intersections falls within a Y-axis increment. The sum of all the filled squares on the histogram is **N(X)**. Step 4: The steps 1-3 are then repeated at a different segment length.

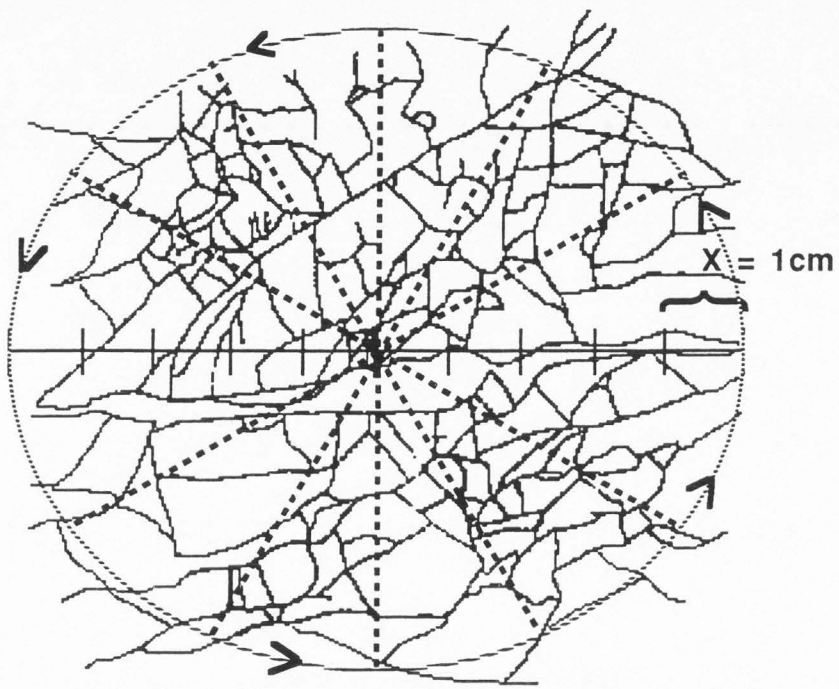

Fig. 13. Plot illustrating the manner in which a segmented analysis line is superposed and rotated onto a fracture trace map. Rotational axis is in the center of the line.

contains the maximum number of fracture intersections. First, the total number of fracture intersections is counted within each line segment (Fig. 12, step 1). These one-dimensional data are then normalized and transferred to a two-dimensional representation, or histogram, in which the X-axis is proportional to the number of line segments and the Y-axis is the normalized number of fractures. The normalization takes place in the calculation of the Y-axis increment, which is simply the maximum number of fracture intersections within a line segment divided by the total number of line segments along the analysis line (Fig. 12, step 2). Next, the number of fractures within each line segment is plotted on the histogram (Fig. 12, step 3). This is accomplished by filling cells or squares on the histogram. A square is filled when the number of fracture intersections falls within a Y-axis increment. The sum of all the filled squares on the histogram is **N(X)**. The procedure is then repeated at a different segment scale.

Once **N(X)** is calculated over several cell sizes, **N(X)** is plotted against **(1/X)** in log-log space (e.g., Fig. 9). Again, if the distribution of data points can be best fit by a straight line of constant slope over the scale studied, then the distribution of fractures along that segmented analysis line is fractal and scale-invariant. Likewise, the slope of the line is the fractal dimension and should range between 1 to 2. In practice, **logN(X)/log(1/X)** slopes were obtained using linear least-squares regression, where **D** values were retained only if the value of r^2 was greater than 0.98. Although it is a linear analysis, the two-dimensional calculation of **N(X)** changes the range **D** from 0<**D**<1 (point<**D**<line) to 1<**D**<2 (line<**D**<plane). There is no formal statistical confirmation of the calculation of **N(X)**, but Hestir (pers. comm.) suggested that the method is likely valid.

Because the Velde et al. (1991) counting method fails to account for fracture density variations along the analysis line (Fig. 14a), the counting method was modified in order to depict fracture clustering. Let us consider the extreme cases for a one-dimensional analysis. For a uniform distribution of fractures over a scale of **X**, each line segment contains the same number of fracture intersections, and so **N(X)** is proportional to the number of line segments, and **D** $\rightarrow$ 2

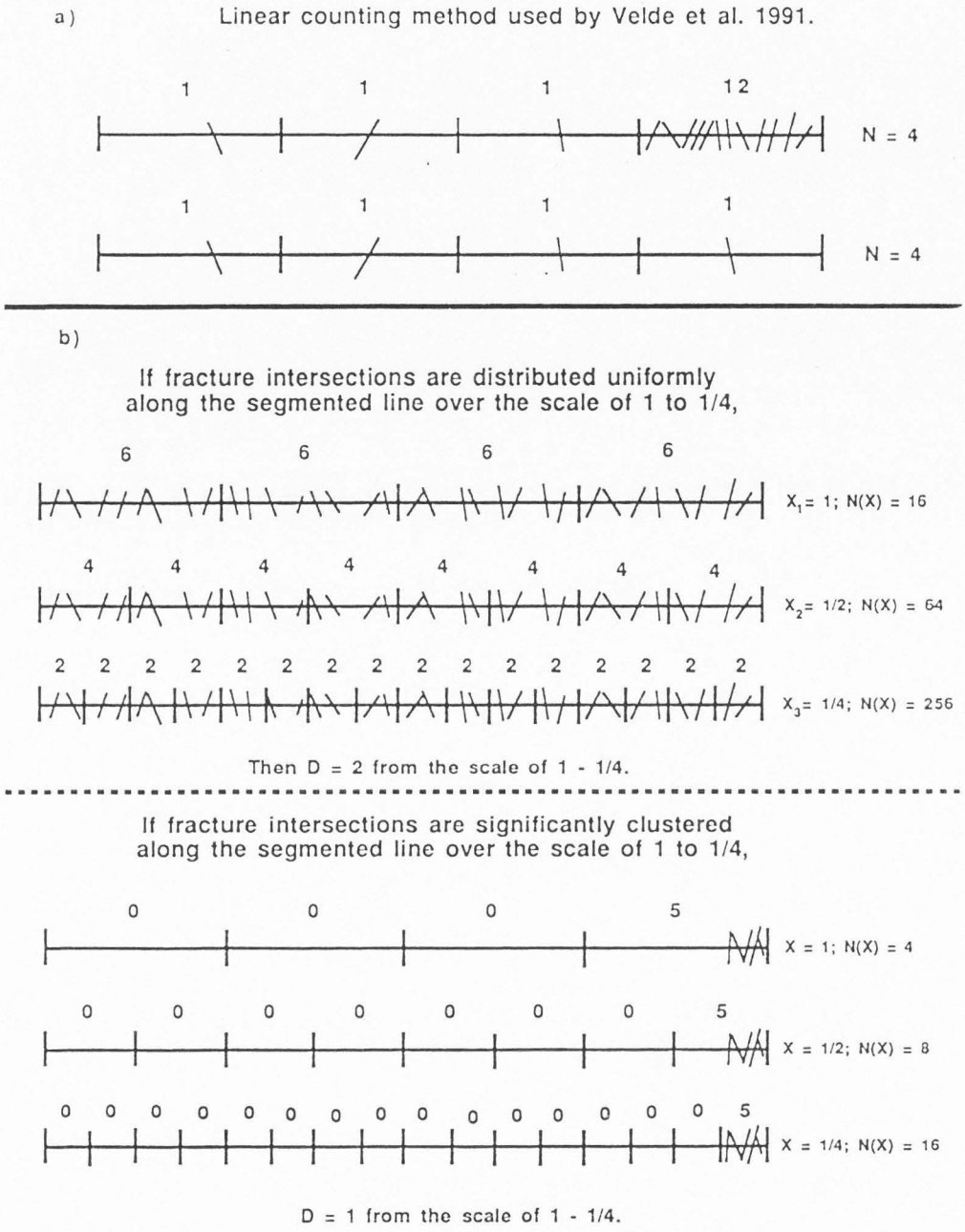

Fig. 14. Graphic illustrating some advantages of the linear fractal technique. (**a**) The shortcoming of the Velde & Dubois (1991) counting method. This method provides the same value of **N** for both examples, even though the fracture distribution along those lines are clearly different. (**b**) Graphic illustrating the difference in fractal dimension between a hypothetical uniform distribution of fracture intersections and an extremely clustered distribution of fracture intersections. **X** ranges from a scale of 1 to 1/4 along a segmented line. When fractures are uniformly distributed in linear space, $D \rightarrow 2$. When fractures are extremely clustered in linear space, $D \rightarrow 1$. Natural fracture distributions are rarely this uniform or clustered and have fractal dimensions between 1 and 2. Thus, this method depicts the clustering of fractures.

(Fig. 14b). For extreme clustering of fractures over a scale of **X**, only one or a few segments along the line contain all fractures, and so **N(X)** is proportional to the number of line segments containing fractures, and **D** $\rightarrow$ 1 (Fig. 14c). Thus, care must be taken to calculate **N(X)** over a range of cell sizes.

Linear fractal analysis characterizes the degree of relative clustering along an analysis line, but does not take into account fracture quantity encountered along that same line. That is, an analysis with 10 fractures can have the same **D** value as an analysis with 20 fractures so long as the clustering is relatively similar. Clearly, the network with 20 fractures will intuitively have a higher permeability than the network with 10 fractures, assuming constant effective aperature. To take this into account, the entire fractal distribution is normalized to the analysis line containing the maximum fracture intersections. Each fractal dimension, corresponding to a different orientation, is normalized to the maximum number of fracture intersections ([# of intersections along a line i / max. # of intersections]x$\mathbf{D}_i$). This normalized value, **D'**, depicts both clustering and fracture quantity as it varies with orientation. Then **D** and **D'** are plotted as a vector in the direction in which it was measured. This vector depiction better accentuates subtle differences characterized by the method (e.g., orientation, clustering, frequency) (Fig. 15).

The aforementioned techniques were applied to 14 fracture trace maps ranging from outcrop- to thin-section scale. Frequency histograms, box counting fractal dimensions, linear fractal dimensions depicted as vectors, and normalized linear fractal dimensions also depicted as vectors are produced and illistrated in the results section.

FAULT GEOCHEMISTRY

Brittle fault zones are often characterized by the presence of gouge or cataclastic fabrics. The textural development of such fabrics is often enhanced by the presence of a fluid phase (Janecke & Evans 1988, Evans 1990a). These fabrics retain a sharp textural and chemical discontinuity, suggesting that solute transport was focused and parallel to the tectonic layering.

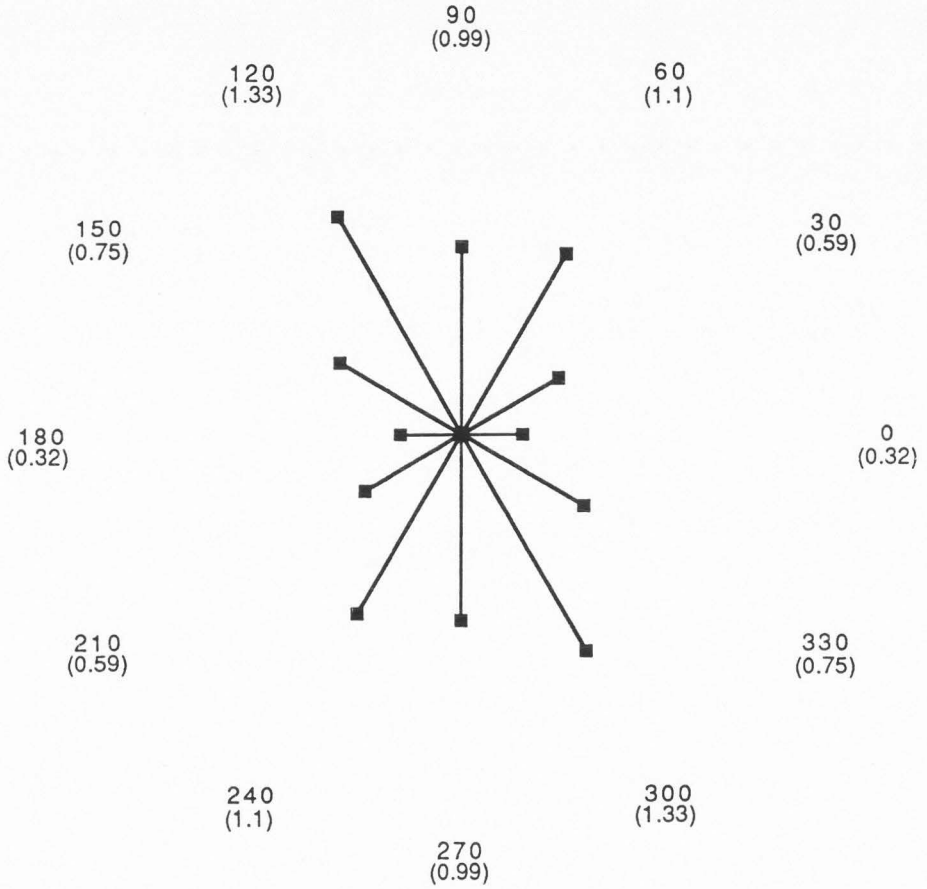

Fig. 15. Sample plot showing final product of the linear fractal analysis. Plot is a normalized fractal ellipse for network CC13. Normalized fractal dimensions, in parentheses below vector orientation, are plotted as a vector. This plot suggests greatest connectivity, uniformity, and fracture density between 0° - 30° or 180° - 210° and 150° - 180° or 330° - 360°.

Some fault zones are characterized by the involvement of fluids that cause a drastic change in the fault zone rheology and the style of deformation by altering the assemblage of minerals and the rates of chemical and mechanical processes during progressive deformation. The presence of a fluid phase during deformation enhances solution transport, microfracturing, and recrystallization. Such chemically active zones generate mineral assemblages that record the deformation and fluid flow history of the fault zone. To adequately characterize the geochemistry of these distinct mineral assemblages, X-ray diffraction and fluorescence spectrometry were used on both the East Fork and the White Rock fault rocks.

X-ray diffraction was used to determine microscopically unobservable mineralogical compositions of vein filling, alteration products, gouge, and cataclasite at different locations within the fault zones. Whole rock geochemistry (major-, and trace-element composition) of fault-related rocks was determined using X-ray fluorescence spectrometry. These data revealed relative concentrations of immobile and mobile constituents within the fault zone, which led to the calculation of fluid/rock ratios and approximate relative volume loss in the fault zone in a similar fashion as Gresens (1967), Grant (1986), O'Hara (1988), O'Hara & Blackburn (1989), and Sinha *et al.* (1988). These authors use quantitative whole rock geochemistry, using major- and trace-element analyses, to characterize fluid/rock interaction in ductile and mylonitic shear zones and during regional metamorphism. They utilize geochemical equations to estimate relative volume losses or gains of ductile and mylonitic shear zone rocks and the subsequent fluid/rock ratios required to produce the inferred volume losses or gains. Similar techniques are used here to determine volume changes and fluid/rock ratios.

X-ray Diffraction (XRD)

X-ray diffraction analyses were done on most fault-related rocks in the White Rock fault zone to determine the presence of clay minerals and other microscopically indiscernible minerals. Protolith samples were also analyzed to determine if the fault zone clays were pre-deformational relicts.

Approximately 10 grams of fault rock fragments were powdered using a porcelain mortar and pestle until the entire sample passed though a 0.124-mm mesh sieve. Oriented mounts were made by mixing a portion of the sieved powder with de-ionized, distilled water, and depositing approximately 2 ml of slurry on a glass X-ray slide. The slurry on the slide was allowed to dry at room temperature until all moisture was evaporated. X-ray spectra were produced for each sample using Ni-filtered Cu Kα radiation. Initial spectra were obtained from 3° - 61° 2θ at a step of 0.05°, then, to differentiate prominent clay spectral peaks, the samples were reanalyzed from 3° - 15° at a step of 0.02°. Oriented mounts were glycolated by placing them in a desiccator containing ethylene glycol and heating the desiccator in an oven at ≈ 65°C for ≈ 4 hours. Samples suspected of containing montmorillonite were reanalyzed from 3° - 15° at a step of 0.02° to detect a peak shift from ≈ 14 Å to ≈ 17 Å. Lastly, the glycolated oriented samples were heated in an oven at ≈ 550°C for one hour in order to desiccate any water remaining in the crystal structure of the kaolinite clays. The presence of kaolinite was confirmed if the ≈ 7 Å peak disappeared as a result of heating at ≈ 550°C. Other clays and phyllosilicates were determined similarly based on the response of spectral peaks to the aforementioned steps as described in Starkey *et al.* (1984).

X-Ray Fluorescence (XRF)

Protolith and progressively deformed samples were powdered using a SPEX mixer/mill grinder so that the entire sample passed through a 0.115-mm mesh. Care was taken to ensure that representative portions of the different fault zone textures and compositions were separated and powdered.

The powdered samples were analyzed using standard XRF techniques at X-Ray Assay Laboratories (XRAL) in Ontario, Canada. XRAL provided weight percent data for all submitted samples on major elements (SiO_2, TiO_2, Al_2O_3, Fe_2O_3, MnO, MgO, CaO, K_2O, Na_2O, P_2O_5, & LOI) and parts per million data for detectable trace elements (Rb, Sr, Cr, Zr, Y, Nb, & Ba) (Table 1 & 2).

Table 1. Whole rock chemical analysis of the East Fork thrust granites and associated fault rocks.

	protolith	damaged zone			
SAMPLE	EFP-YR	EF2A-dam	EF2-dam.	EF4A-dam.	EFJE4-dam
SiO_2(wt%)	72.7	73.3	70.9	74.3	71.1
TiO_2	0.164	0.231	0.224	0.234	0.166
Al_2O_3	14.1	13.2	13.0	13.1	13.7
Fe_2O_3	1.14	1.29	1.73	1.61	3.20
MnO	0.01	0.01	0.03	0.02	0.03
MgO	0.28	0.20	0.78	0.44	0.28
CaO	1.47	0.63	1.70	0.70	1.68
Na_2O	3.51	3.54	2.92	3.17	3.31
K_2O	3.93	4.91	4.58	4.50	3.87
P_2O_5	0.05	0.05	0.03	0.03	0.04
LOI	1.45	1.20	3.70	1.62	1.75
Total	99.0	98.8	99.9	100.0	99.3
Rb(ppm)	90	107	100	104	96
Sr	230	146	233	226	258
Y	<10	<10	<10	<10	27
Zr	155	164	189	199	226
Cr	<10	10	57	54	<10
Nb	21	19	25	<10	19
Ba	1590	1690	1640	1650	1120

	vein	damaged/gouge		gouge/cataclasite		
SAMPLE	EF2-vein	EF2-88	EF14a-88	EF2c-91	EFJE-2	EF4B
SiO_2(wt%)	96.6	79.0	77.4	78.6	75.3	75.6
TiO_2	0.018	0.115	0.186	0.156	0.190	0.179
Al_2O_3	1.50	10.7	12.1	10.2	12.4	12.4
Fe_2O_3	0.03	0.65	1.36	1.30	1.96	1.17
MnO	0.01	0.01	0.02	0.01	0.01	0.01
MgO	0.08	0.21	0.44	0.20	0.45	0.14
CaO	0.21	0.39	0.76	0.40	0.51	0.27
Na_2O	0.28	1.19	3.61	2.13	0.82	2.75
K_2O	0.71	5.59	0.34	4.01	3.66	4.82
P_2O_5	0.02	0.03	0.04	0.05	0.05	0.05
LOI	0.47	1.15	3.80	1.35	3.50	1.39
Total	100.0	99.3	100.1	98.6	99.0	99.0
Rb(ppm)	31	163	31	91	106	89
Sr	<10	79	125	83	200	107
Y	<10	<10	<10	10	13	<10
Zr	<10	59	111	116	133	144
Cr	<10	<10	18	<10	<10	<10
Nb	19	28	24	<10	20	15
Ba	432	1700	159	1380	1210	1650

Table 2. Whole rock chemical analysis of the White Rock thrust granites and associated fault rocks.

	protolith		protocataclasite					vein
SAMPLE	WR7-91	WRe-92	WR6-91	WR13-91	WR8a-91	WR5-91	WR16-91	WR4-91
SiO_2(wt%)	68.5	70.3	63.2	65.2	66.9	67.7	65.3	54.3
TiO_2	0.366	0.274	0.162	0.529	0.112	0.174	0.334	0.172
Al_2O_3	16.2	14.5	16.7	15.6	15.8	14.5	15.4	19.2
Fe_2O_3	3.59	1.72	3.08	3.13	1.66	1.41	2.58	1.52
MnO	0.03	0.02	0.02	0.04	0.01	0.01	0.03	0.03
MgO	0.70	0.66	0.24	1.78	0.22	0.44	0.97	0.75
CaO	4.22	1.44	1.05	2.42	0.91	1.89	2.57	8.98
Na_2O	4.65	3.36	1.97	3.23	2.02	1.90	2.75	1.86
K_2O	1.36	5.64	10.3	5.17	9.12	6.98	4.99	1.74
P_2O_5	0.18	0.12	0.21	0.17	0.11	0.07	0.13	0.07
LOI	0.77	1.30	0.77	1.55	0.90	3.70	3.50	10.9
Total	100.4	99.7	98.4	99.2	98.3	99.2	98.9	99.6
Rb(ppm)	50	99	149	96	142	132	96	32
Sr	462	396	476	417	403	362	297	280
Y	16	19	38	15	<10	<10	<10	<10
Zr	194	130	29	59	12	82	214	19
Cr	24	<10	<10	12	<10	<10	<10	<10
Nb	16	14	15	21	29	31	22	13
Ba	461	2770	5660	2710	4540	3360	2280	392

	vein	cataclasites				ultracat.	protocat.
SAMPLE	WR19-91	WR15-91	WR10-91	WR8b-91	WR14b-91	WRf-92	WR1-91
SiO_2(wt%)	56.6	59.3	58.3	59.1	58.6	57.6	67.6
TiO_2	0.225	0.746	0.529	0.433	0.602	0.728	0.283
Al_2O_3	19.0	16.3	16.2	16.3	15.1	14.9	14.5
Fe_2O_3	1.79	6.64	4.80	4.80	5.56	5.40	2.41
MnO	0.02	0.08	0.06	0.05	0.05	0.05	0.02
MgO	0.91	2.34	1.77	1.42	2.12	2.49	0.66
CaO	8.02	6.37	3.91	2.76	4.45	4.65	1.24
Na_2O	0.95	4.29	1.95	2.00	1.97	2.38	2.20
K_2O	2.57	1.58	5.19	6.93	3.07	3.01	7.29
P_2O_5	0.08	0.29	0.31	0.33	0.28	0.30	0.10
LOI	10.0	2.45	5.08	3.70	7.95	8.05	1.75
Total	100.3	100.6	98.5	98.3	100.0	99.8	98.3
Rb(ppm)	59	31	103	126	81	76	168
Sr	286	1130	351	370	599	425	170
Y	<10	63	39	36	38	53	<10
Zr	119	233	136	119	179	224	245
Cr	12	47	51	17	24	54	<10
Nb	15	19	<10	25	34	28	19
Ba	634	429	2410	3340	1200	1430	1320

Several geochemical techniques discussed below were employed to determine: 1) the response of whole rock chemistry to varying fluid assisted deformation processes within the fault zone; 2) volume losses or gains in the fault zone relative to the protolith granites; and 3) fluid/rock ratios (Gresens 1967, Grant 1986, Sinha *et al.* 1986, O'Hara 1988, O'Hara & Blackburn 1989).

Because of the apparent open-system behavior of the fault zones, the calculation of systematic changes in the gain or loss of elements requires that a reference frame be established for normalizing the data. All analysis techniques are contingent upon selecting, as rationally as possible, a reference element or oxide that remained constant and immobile throughout deformation. Analyses are normalized and calculated relative to this immobile constituent. Microscopic analyses of protolith and fault rocks reveal that minerals such as ilmenite, Fe-Ti oxides, rutile and sphene remain chemically unaltered throughout deformation. These phases are generally thought to be refractory and insoluble, particularly at the lower temperatures and pressures (350°C to 200°C), and the process of silica and feldspar dissolution and transport would tend to increase their concentrations. These residual minerals have been comminuted, but do not appear to have been chemically altered due to fluid-rock interactions. For this study, Ti (as TiO_2) is inferred to be the most immobile constituent within the fault zone. Also, previous geochemical studies of metasomatized rocks and shear zones suggest the immobility of Ti as well as Mg, Mn, Zr, Y, and P (but to a lesser degree) (Cann 1970, Correns 1978, Herrmann 1978, Dostal *et al.* 1980, Hanson 1980, Floyd & Winchester 1983, Winchester & Max 1984, Sinha *et al.* 1986, Vocke *et al.* 1987, O'Hara 1988, O'Hara & Blackburn 1989, Glazner & Bartley 1991). Thus, this work assumes that high-field-strength cations (e.g., Ti) were largely immobile and that their apparent enrichment is due to large volume losses (of SiO_2 and alkalies) in the cataclasites. Some authors assume Al (as Al_2O_3) immobility (e.g., Sinha *et al.* 1986), but large amounts of Al-rich laumontite veins in the fault cores and damaged zones preclude this possibility.

Note that weight percent and parts per million data are used for concentrations (**C**) in the following geochemical equations, and that subscripts of **Si** and **Ti** refer to concentrations of SiO_2 and TiO_2.

Gresens Analysis

Quantitative evaluation of chemical mass transport in brittle fault zones requires knowledge of the composition of rocks in the original and altered states, together with the constraints on any possible volume changes. Gresens (1967) suggested incorporating specific gravity data into two-way mass-balance calculations, such that fixing either volume change or the behavior of one component (TiO_2 in this case) during a reaction provides a unique solution. Gains or losses of other components can then be calculated assuming that the volume change is a factor (f_V) common to the behavior of all components.

For the alteration of protolith (**pr**) to fault rock (**fa**), with possible volume change, Gresens' basic formula is:

$$a[f_V(g^{fa}/g^{pr})C_n^{fa} - C_n^{pr}] = X_n. \qquad (4)$$

where g is the specific gravity, f_V is the volume factor, **C** is the concentration, **n** is the subscript for the component, **a** is the reference mass of the original sample, and **X** is the gain or loss of the component relative to the reference mass. Specific gravities for protolith and fault rocks were determined with a Jolly balance. If **a** = 100 g, as is convenient if using whole rock chemical analyses summed to 100 weight percent, the equation becomes:

$$100g[f_V(g^{fa}/g^{pr})C_n^{fa} - C_n^{pr}] = X_n. \qquad (5)$$

For any metasomatic transformation of parent rock to altered product, volume factors, f_V, may be computed which correspond to the isochemical behavior of individual components. Clustering of the volume factors of several immobile components (such as TiO_2, Fe_2O_3, MgO, MnO, P_2O_5) provides a rational basis for estimating the volume change of the reaction as a whole. Thus, if Ti immobility is assumed, the f_V value corresponding to isochemical behavior can be calculated:

$$f_{VTi} = (C_{Ti}^{pr}/C_{Ti}^{fa})(g^{pr}/g^{fa}). \qquad (6)$$

Ideally, f_v for the other assumed immobile constituents (TiO_2, Fe_2O_3, MgO, MnO, Sr, P_2O_5) should cluster around the same value.

Furthermore, rigorous calculations of chemical mass balance require that the series of altered rocks, along with the unaltered precursor, belonged to an initially chemically uniform population. It is important to emphasize that the observed metasomatically altered products represent specified finite changes relative to the precursor, but that such changes may have been arrived at via a complex sequence of incremental chemical transfers (Gresens 1967).

Once a legitimate volume factor is calculated for the fault system, a balanced chemical equation using mass gains or losses per 100 g of protolith can be calculated by solving for $\mathbf{X_n}$ per 100 g of rock using equation 5.

Grant Analysis

Rearrangement of equation 5 provides a simple and direct graphical method for considering the changes in mass or volume and concentrations that may arise in metasomatic alterations (Grant 1986). In general, concentrations (**C**) of protolith rocks and fault rocks are plotted against each other and a reference line corresponding to a zero concentration change (an immobile isocon) is determined by a best fit to the immobile element data (the best fit line is forced through the origin). This is simply a graphical simultaneous solution to equation 5 for the zero concentration change. The slope of the immobile isocon reveals the mass change and, if the density of the protolith and fault rocks is known, the volume change in the alteration. Once the immobile isocon is chosen, one can determine the gains and losses of each constituent relative to concentrations in the original rock, graphically or by calculation. An immobile isocon slope of one indicates isovolumetric conditions, that is, volumetric concentrations remained constant throughout deformation. The two major steps are the initial choice of the protolith for the altered rocks and the choice of an immobile isocon. A probable immobile isocon can be best-fit to the assumed immobile constituents, if they cluster around the same slope. This technique allows for easy visualization of the relative behavior of different constituents from protolith to fault

zone and may aid in determining the immobile constituents. This graphical method nicely depicts relative enrichments (slope of constituent > slope of isocon) and depletions (slope of constituent < slope of isocon).

If constant mass is assumed (Grant 1986),

$$C^{fa} = C^{pr}. \quad (7)$$

If constant volume is assumed (Grant 1986),

$$C^{fa} = (g^{pr}/g^{fa})C^{pr}. \quad (8)$$

Assuming certain elements were totally immobile, like Ti, the amount of mass loss (M_ℓ), relative to constant mass, and volume loss (V_ℓ), relative to constant volume conditions, required to produce the observed enrichments can be calculated from the following expressions (Grant 1986):

$$M_\ell = [(1/S)-1]x100, \quad (9)$$

$$V_\ell = [(1/S)(g^{fa}/g^{pr})-1]x100. \quad (10)$$

where **S** is the slope of the determined immobile isocon (e.g., $S \approx (C^{fa}_{Ti}/C^{pr}_{Ti})$, and M_ℓ and V_ℓ are in percent loss or gain (see Fig. 16 for sample plot). From this information, f_v then can be determined:

$$f_v = (1/S)(g^{pr}/g^{fa}). \quad (11)$$

Sinha Analysis

Sinha *et al.* (1986), like Grant (1986), describes a method of graphically depicting percent gains or losses of constituents relative to the protolith after normalization to an inferred immobile constituent. This method, unlike the Grant method, depicts the gradual variations from protolith to fault core, as opposed to showing the relationship of only the protolith and fault core. Percentage change ($\%_c$), assuming Ti immobility, is calculated using the following equation:

$$\%_c = [(C^{fa}_n/C^{pr}_n)(C^{pr}_{Ti}/C^{fa}_{Ti}) - 1]x100, \quad (12)$$

where $-\%_c$ = a loss relative to the protolith for the **n**th constituent, $+\%_c$ = a gain relative to the protolith for the **n**th constituent.

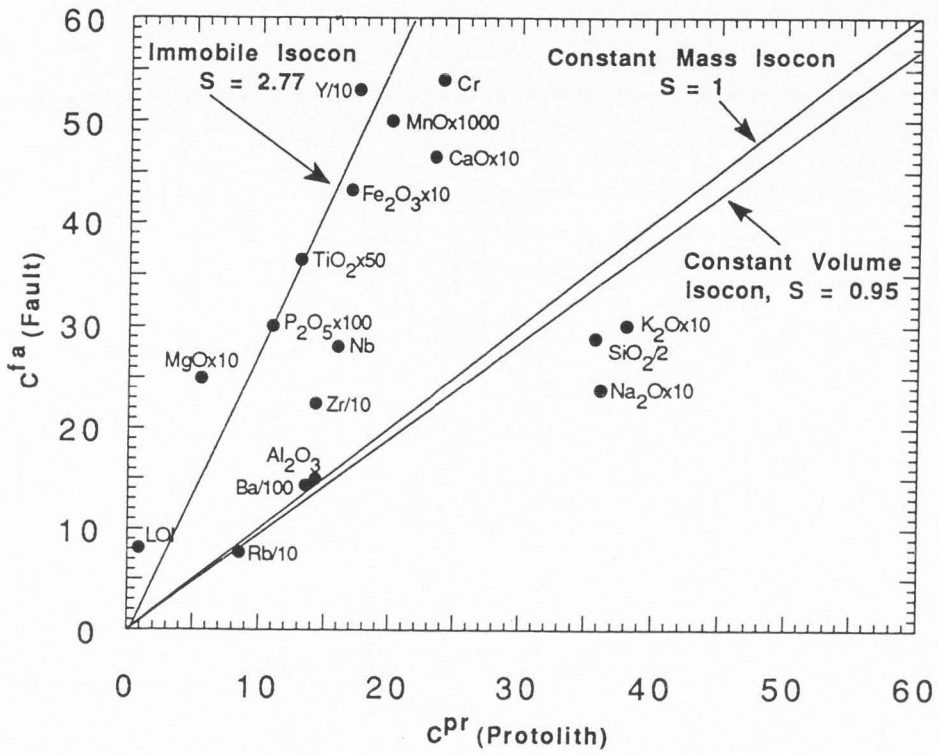

Fig. 16. Sample Grant Diagram showing average composition of a protolith versus average composition of a fault rock. Concentrations (**C**) are in wt% (oxides) and ppm (trace elements) scaled arbitrarily (so as to maintain slope) to fit on the plot. For example, SiO_2 wt% of protolith and fault is ≈ 70% and 60%, respectively. These values are then scaled by a factor of 1/2 to fit on the graph. The slope of the constant mass isocon is always 1.0. The slope of the constant volume isocon is based on the density ratio between the fault and the protolith. The slope of the immobile isocon is derived from a best-fit through the immobile components.

Fluid/Rock Ratios

Assuming Ti immobility, the weight and volume of fluid required to produce estimated volume losses can be calculated on the basis of silica loss from the fault zone. Silica is used in this case because: 1) of evidence of its mobility; 2) of large losses relative to the protolith; 3) it is volumetrically greater than any other component; and 4) extensive research has been done on silica solubility at a range of temperatures and pressures (Walther & Helgeson 1977, Barnes 1979, Rimstidt & Barnes 1980, Fournier & Potter 1982). Techniques in calculating fluid/rock ratios were extracted from Sinha *et al.* (1986), Wood & Walther (1986), O'Hara (1988), O'Hara & Blackburn (1989).

Fluid/rock ratio calculations discussed hereafter are based on a synthesis of techniques used by Gresens (1967), Sinha *et al.* (1986), Grant (1986), Wood & Walther (1986), O'Hara (1988), O'Hara & Blackburn (1989). The fluid/rock weight ratio (N_W) is calculated using the equation:

$$N_W = L_{Si}/C^f_{Si}(1 - s), \qquad (13)$$

where L_{Si} is the loss of silica in the fault relative to the protolith granite measured in grams of silica lost per 100 grams of rock, C^f_{Si} is the concentration (solubility) of silica in the fluid in grams of silica per grams of solute as calculated using the silica solubility equation in Fournier & Potter (1982), and **s** is the fractional saturation of the fluid with respect to silica.

If a loss of silica is apparent from equation 5, then:

$$L_{Si} = X_{Si} = [f_{vTi}(g^{fa}/g^{pr})C^{fa}_{Si} - C^{pr}_{Si}], \qquad (14)$$

per 100 g of protolith, where:

$$f_{vTi} = (C^{pr}_{Ti}/C^{fa}_{Ti})(g^{pr}/g^{fa}). \qquad (15)$$

Substitution of equation 15 into equation 14 leads to:

$$L_{Si} = X_{Si} = [C^{fa}_{Si}(C^{pr}_{Ti}/C^{fa}_{Ti}) - C^{pr}_{Si}], \qquad (16)$$

per 100 g of protolith.

Based on cross-section restorations, assuming an average geothermal gradient of ≈30°C/km, and deformation textures and styles within the fault zones, temperatures in the fault zones when the Precambrian granites were breached and the faults began to popagate are assumed to have been no greater than 350°C for the White Rock thrust and no greater than 250°C for the East Fork thrust. Temperatures likely decreased as deformation progressed due to uplift and erosion. Using the equation in Fournier & Potter (1982) relating silica solubility in water from 25°C to 900°C, the solubility of the silica in the White Rock and East Fork faults can be estimated (Table 3).

Table 3. Temperatures and corresponding silica solubilities (specific volume of water assumed to be ≈ 1) used in fluid/rock ratio equations (Fournier & Potter 1982).

Temp. (°C)	Solubility
350	$2.5g/kg = 2.5x10^{-3}g/g$
300	$1.4g/kg = 1.4x10^{-3}g/g$
250	$0.76g/kg = 7.6x10^{-4}g/g$
200	$0.38g/kg = 3.8x10^{-4}g/g$
150	$0.15g/kg = 1.5x10^{-4}g/g$

Saturation of fault zone fluids with respect to silica in the fault zones is assumed to range from 0% - 90%. Fluid likely encountered silica throughout its path in the fault zone. Saturation was likely low during initial infiltration, then gradually increased to saturation as the fluids flowed through the fault zone. Then, as the saturated fluids migrated upward along the faults, temperature and pressure decreased, fluids became supersaturared with respect to silica, and silica was deposited in fractures and in gouge/cataclasite zones. This produces an inherently complex series of saturation changes in time and space. Note that when saturation becomes 100%, equation 13 is not applicable because the fluids can no longer dissolve and transport more silica. This also suggests that fluid/rock ratios calculated from equation 13 provide only a

minimum fluid/rock ratio, taking into account only the fluid that was chemically active and not the fluid that was chemically inert with respect to silica but still flowing through the fault zone.

Equation 13 can be broken down such that:

$$N_W = L_{Si}/C^f_{Si}(1 - s),$$

$$N_W = \text{(g silica lost/100g rock)/[(g silica/g fluid)(1 - s)]}$$

$$N_W = \text{[weight of fluid/weight of rock] dimensionless.}$$

Calculation of the fluid/rock volume ratio (N_V) is similar to equation 13 with the exception that appropriate quantities are divided by their densities (ρ), resulting in volumes:

$$N_V = L_{Si}(\rho^{pr}/\rho^{SiO2})/C^f_{Si}(\rho^{H20}/\rho^{SiO2})(1 - s), \quad (17)$$

$$N_V = L_{Si}(\rho^{pr})/C^f_{Si}(1 - s), \quad (18)$$

$$N_V = N_W\rho^{pr}, \quad (19)$$

$$N_V = \text{cm}^3 \text{ of fluid/cm}^3 \text{ of rock,}$$

$$N_V = \text{[volume of fluid/volume of rock] dimensionless,}$$

where $\rho^{pr} \approx g^{pr}$ and $\rho^{H20} \approx 1.0\text{g/cm}^3$.

Sinha-type diagrams, Grant-type diagrams, balanced component equations, and fluid/rock weight and volume ratios have been produced for the East Fork and White Rock Fault using the aforementioned techniques.

PERMEABILITY TESTING

Steady-state gas and water permeability tests on oriented cores (see Fig. 8 for sampling scheme) taken from protolith, damaged zones, and gouge and cataclasite zones in the East Fork fault further constrained the relative permeability structure as it varies within and along fault zones. Nineteen core samples with a diameter of 2.5 cm and lengths of 3-10 cm were tested at Terra Tek, Inc. of Salt Lake City at ambient temperatures and pressures. Seven samples were previously tested by Forster & Evans (1991) and 12 samples were tested for this project. Permeability results can be compared to corresponding hand-sample, thin-section, and outcrop

fracture analyses and previously calculated core permeability values (Brace 1984, Morrow *et al.* 1984, Morrow & Byerlee 1988, Forster & Evans 1991, Lockner *et al.* 1991, Clauser 1992). Laboratory permeability testing, however, will not reproduce the exact thermal and hydrologic conditions during fault evolution. Hence, core permeability test results may yield somewhat higher permeability values than expected if syntectonic conditions are assumed. Yet, results obtained from the tests should provide rough estimates of the relative permeability structure of different zones within a fault that can be compared with other lab and modeling results. Some thin sections were made from permeability-tested cores to determine the fracture pattern responsible for the resultant permeability values.

RESULTS

FIELD AND MICROSTRUCTURAL ANALYSES

East Fork Fault

Detailed field, microstructural, and XRF studies on the East Fork fault system were previously accomplished by Evans (1988, 1990a, in press). A description of those results, supplemented with observations resulting from this research, is summarized below.

The deepest structural level (≈ 8 km) in the Washakie thrust system is exposed in the East Fork fault system. The East Fork of the Wind River has eroded through Paleozoic rocks of the EA and Diamond Ridge thrust sheets to expose faults in Precambrian crystalline rocks (Fig. 6). East Fork faults are either narrow, well-defined faults or wide zones of gouge. Some faults zones are made of narrow faults spaced 1 cm to 1 m apart, and these zones are up to 30 m wide (Fig. 7b). Narrow faults consist of well foliated, indurated (silica cementation), fine-grained gouge and cataclasite with sharp contacts. Wide, large displacement (0.1 km to 4 km) faults, which are responsible for emplacement and imbrication of the thrust sheet, consist of fine-grained gouge and cataclasite, with crude to well defined foliation. The wide gouge zones are up to 6 m wide and separate lozenges of fractured and altered protolith (Fig. 7a, c, & d).

Regardless of the scale, the faults typically are internally zoned. These zones can be roughly separated into: 1) unaltered protolith; 2) fractured and faulted damaged zone (Fig. 7a & c); and 3) gouge and cataclasite zones (Fig. 7a & c). The unaltered granitic protolith primarily consists of coarse-grained microcline, plagioclase, quartz, and biotite with accessory minerals of rutile, hematite, ilmenite, and other opaque Fe-Ti oxides. The fractured damaged zone composition is identical to the protolith, except kaolinite and iron oxide filling is present in the fractures. Subsidiary faults in the damaged zone are often subparallel (± 30° to the fault plane) to the main fault plane. Within the fault gouge and cataclasite, microcline, plagioclase, quartz, and

biotite are chemically altered to sericitized feldspar, kaolinite, and iron oxide staining from the liberation and mobilization of Fe from biotite.

Faults in the East Fork zone dip 30° to 70° northwest or northeast, and mark the continuation of the Diamond Ridge fault and related faults in the internal part of the thrust sheet (Evans in press). Slickenlines show that the motion along the faults was dominantly dip slip and indicate that the slip direction ranged from south to southwest (Evans in press). Narrow, small-displacement (grain-scale to 30 cm) faults, which likely accommodated much of the internal deformation within the thrust sheet, are characterized by discrete bounding slickenside surfaces or by narrow zones of foliated cataclasite. With increased slip, feldspars altered to phyllosilicates and grain size were further reduced as slip was concentrated along narrow faults (Evans 1988 & Evans 1990a). Wide gouge zones developed by roughly the same process. Wide zones commonly display an irregular, wavy texture. This is likely a result of syntectonic alteration of feldspar to phyllosilicates, and cyclic fracturing and healing of quartz within the faults. Fault boundaries range from sharp to gradational, and grooved, polished, and slickenlined surfaces are common.

Fault gouge and cataclasite are red to maroon. This is likely a result of syntectonic alteration of biotite and hornblende, subsequently liberating and mobilizing magnesium and iron. The iron oxides were likely fluid-transmitted into intergranular fractures and disseminated into the fine-grained gouge and cataclasite.

Based on field observations, fracture and subsidiary fault density increases toward the fault zone. Likewise, transgranular, fault-subparallel fracture density also increases toward the core. Visual observations and fracture orientation statistics suggest that fracture patterns perpendicular to the slip direction and the plane of the fault are roughly orthogonal, while fracture patterns parallel to the slip direction and perpendicular to the plane of the fault are approximately diamond shaped. Fractures tend to nucleate at, and propagate along, mica-rich zones and feldspar cleavage planes. Quartz veining through fractures is pervasive at both the macroscopic

and microscopic scale in the damaged zone, suggesting high permeability, transportability and chemical reactivity of material through this zone. In addition, the quartz veins are layered with iron oxides and magnetite, suggesting at least two temporally distributed episodes of fluid flow. Conversely, the cataclasite zones are characterized by a lack of veins, suggesting low permeability and transportability, albeit chemical reactivity of material likely was high in this zone. Induration of the gouge and cataclasite with silica cement suggests that fluid saturation and fluid/rock chemical interaction was prevalent in these zones without the capacity to transport. These observations indicate that fluid-rock interaction was concentrated in the core and the damaged zone, and transport was concentrated in the damaged zone.

Because feldspars are volumetrically dominant, brittle deformation and comminution of feldspars were the dominant deformation mechanisms. Feldspars deformed by comminution from extension and shear fractures primarily along cleavage planes. Quartz deformed primarily by brittle fracture. Syntectonic alteration of feldspars to clay minerals resulted in the formation of a crude foliation. Crystal plasticity and diffusional mass transfer were likely unimportant in these rocks during the Laramide deformation event.

The foliation in the fault gouge and cataclasite is defined by alignment of phyllosilicates, segregation and elongation of minerals, fractures and faults that are nearly parallel to the fault boundaries, and seams of secondary and opaque minerals in the faults. The development of phyllosilicates was likely syntectonic because: 1) there is an increase in the amount of phyllosilicates with increased feldspar deformation; 2) alignment of kaolinite grains increases with increased strain in the faults; 3) little kaolinite or weathering rims on feldspar is observed in the protolith; and 4) phyllosilicates are kinked, folded, and locally faulted. Kink bands and folds are not present in deformed feldspars, thus it is not likely that kaolinite replaced feldspars after deformation.

Slightly deformed late-stage quartz veins are abundant and parallel to or cut through wide gouge zones. Quartz veins are mostly parallel to or oriented at a shallow angle to faults, and

range from grain-scale thickness up to 1 m (Fig. 7a, c, & d). Some quartz veins contain clasts of fractured damaged zone and gouge/cataclasite zone breccia, which suggests that implosion brecciation may have been present (Sibson 1986) (Fig. 7d). Quartz veins are likely syntectonic because they are: 1) truncated by Tertiary (Eocene) sediments and volcanics; 2) locally folded and faulted; 3) subparallel to faulting events; and 4) truncate and are truncated by gouge and cataclasite zones.

White Rock Fault

The White Rock Thrust is macroscopically expressed as a ≈ 50 m thick zone of strong deformation at most outcroppings (Fig. 17a). However, the most intense deformation is concentrated in a zone less than 10 m thick. Fault outcroppings are best exposed where Precambrian granite overrides the massive, competent Madison Formation limestone below Flat Top Mountain (Figs. 3 & 4). Minimal weathering and subjective erosion in these areas facilitate fault exposure. Traces of the main fault strike approximately north-northwest and dip ≈ 20° to 70° (Fig. 18a-b)(variation in dip is likely due to localized thrust ramping) and movement along the fault is principally dip-slip (Fig. 18c). Structural level ranged from ≈ 10 km at Flat Top Mountain up to 8 km near Roaring Fork Canyon (Fig. 3).

Like the East Fork faults, the White Rock thrust is also internally zoned with respect to structure. Fault zone size in this study is macroscopically defined as the volume of rock that exhibits a greater intensity of brittle and cataclastic deformation than is typical of the surrounding protolith (e.g., Chester & Logan 1986). The zones can be separated into: 1) relatively unaltered protolith (Fig. 5a & 17b); 2) fractured, veined, and faulted damaged zone (Fig. 5a); and 3) crude to well foliated gouge, protocataclasite, cataclasite, and ultracataclasite (henceforth termed the fault core)(Fig. 17b).

The unaltered protolith compositionally ranges from granitic to adamelitic, and primarily consists of microcline (≈ 35%), plagioclase (≈ 30%), quartz (≈ 27%), and biotite/chlorite (≈ 5%) with accessory minerals of rutile, hematite, ilmenite, and other opaque Fe-Ti oxides (≈ 3%) (Fig.

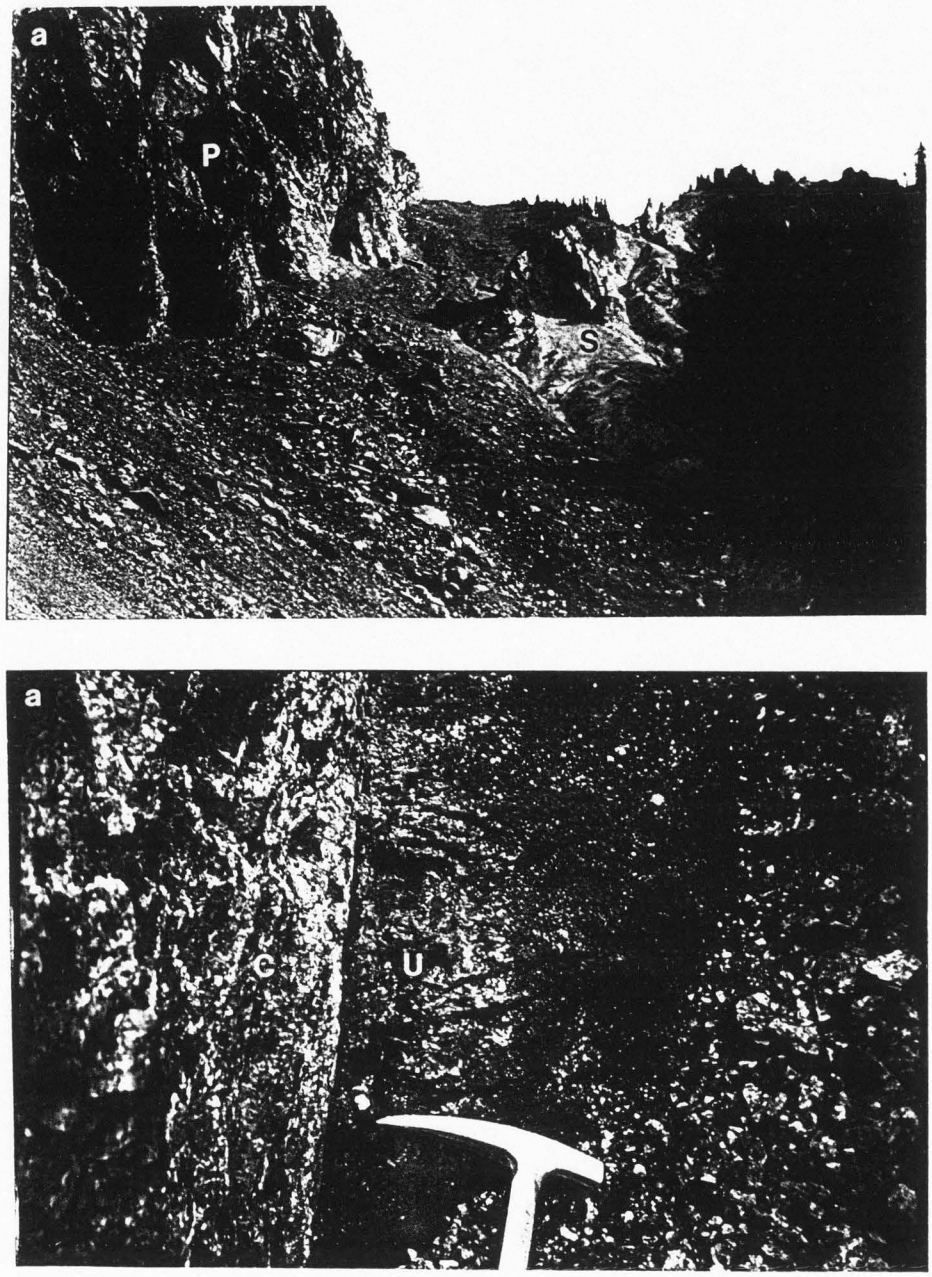

Fig. 17. Outcrop photographs of the White Rock thrust on Flat Top Mountain. (**a**) View to the south of White Rock fault zone (F). Zone is ≈ 50 meters wide and is bounded by protolith granite (P) in the hanging wall and Paleozoic sedimentary rocks (S) in the footwall. (**b**) Outcrop of a thick ultracataclasite zone (U) in sharp contact with a cataclasite zone (C). The ultracataclasite continues to the right under the talus.

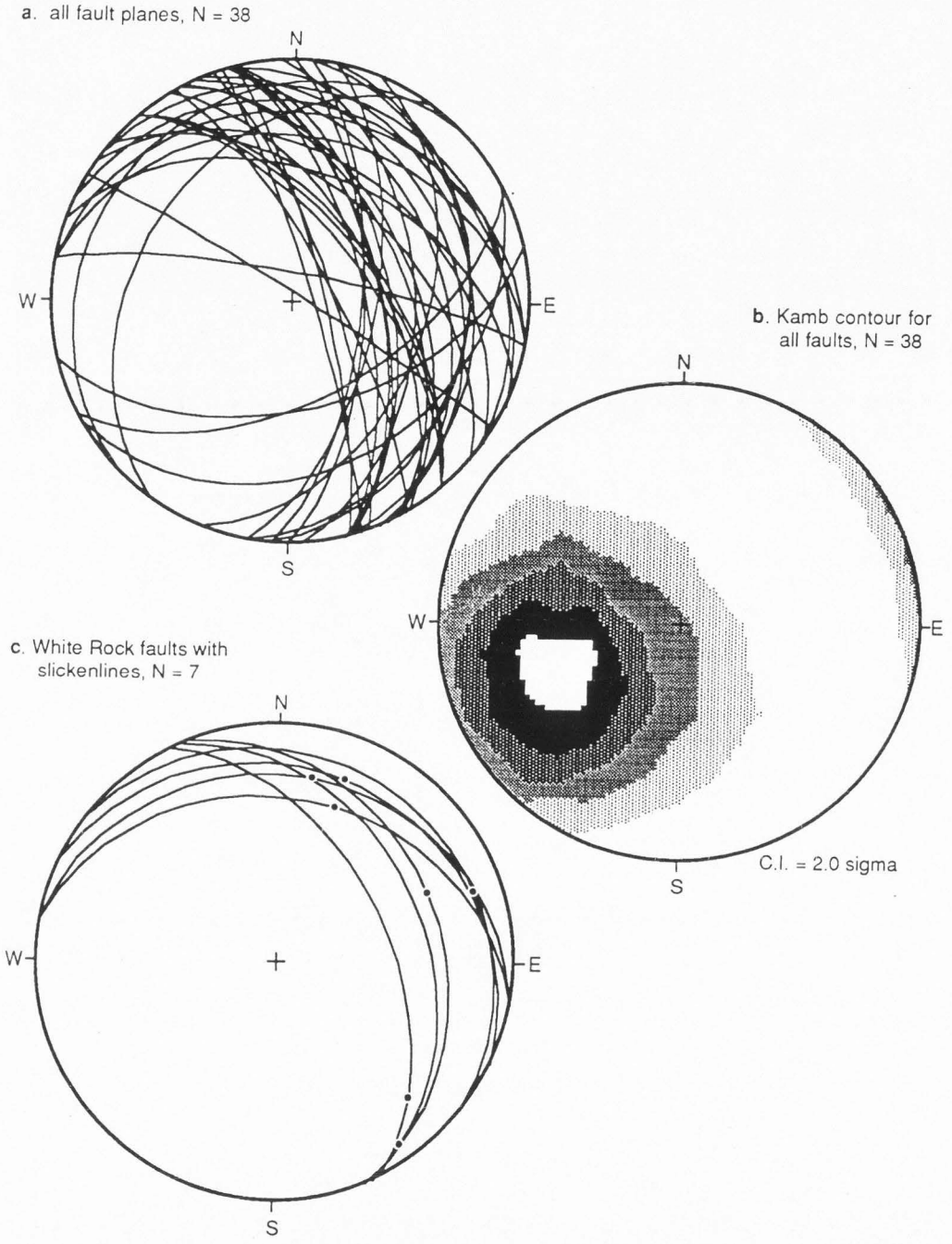

Fig. 18. Lower Hemisphere equal area projection (north at top) of fault data from the White Rock thrust. (**a**) Stereogram of fault planes. Faults strike mostly north-northwest and dip from 20° to 80° to the east. (**b**) Kamb contour of poles to fault planes. (**c**) Stereogram of faults with slickenlines. Faults show primarily dip-slip motion.

19a). The protolith is essentially unaltered, with the exception of rare kink banding in feldspars and undulose extinction and subgrains in quartz, which are likely a remnant of Precambrian deformation (Mitra & Frost 1981). Diagrams for estimating composition by volume were used to determine rough mineralogical percentages (Compton 1985).

The fractured damaged zone composition is nearly identical to the protolith, except abundant zeolite (mostly laumontite) fillings are present in fractures (Fig. 5a), and feldspars are moderately sericitized. Subsidiary faults, fractures, and veins in the damaged zone are often subparallel, or at a shallow angle, to the main fault. Fractures tend to nucleate and propagate along zones of relative weakness, e.g., feldspar cleavage planes and micas.

The core of the fault zone is either a narrow zone of intense deformation (producing non-foliated to very-foliated ultracataclasites 0.5 to 10 m thick), or anastomosing narrow zones (less than 0.5 m thick) of intense deformation (ultracataclasites) surrounding lenses of somewhat less deformed, macroscopically veined, non-foliated to crudely foliated cataclasites and protocataclasites. Foliation in the ultracataclasite is defined by syntectonic alignment of iron oxides, clay, and mica minerals. The core is bounded by a thick damaged zone (1 to 40 m thick) consisting of sets of fault-subparallel, phacoidal fractures and veins, thin, localized zones of cataclasite, and small displacement subsidiary faults (grain-scale to meter-scale). At some locations along the fault, the macroscopic contact between relatively unaltered protolith granite and intensely altered fault core is sharp (Fig. 5a). The contact is typically characterized by a narrow zone (1 to 10 cm thick) of cataclasites or ultracataclasites signifying a narrow zone of localized slip at the edge of the fault zone.

Microstructure

The cataclasites and ultracataclasites from the core of the White Rock thrust exhibit significant alteration and different elemental abundances than the protolith, reflecting concentrated cataclasis, fluid/rock chemical reaction, and solute transport and deposition by fluids. Within the fault core, microcline, plagioclase, quartz, and biotite/chlorite are chemically

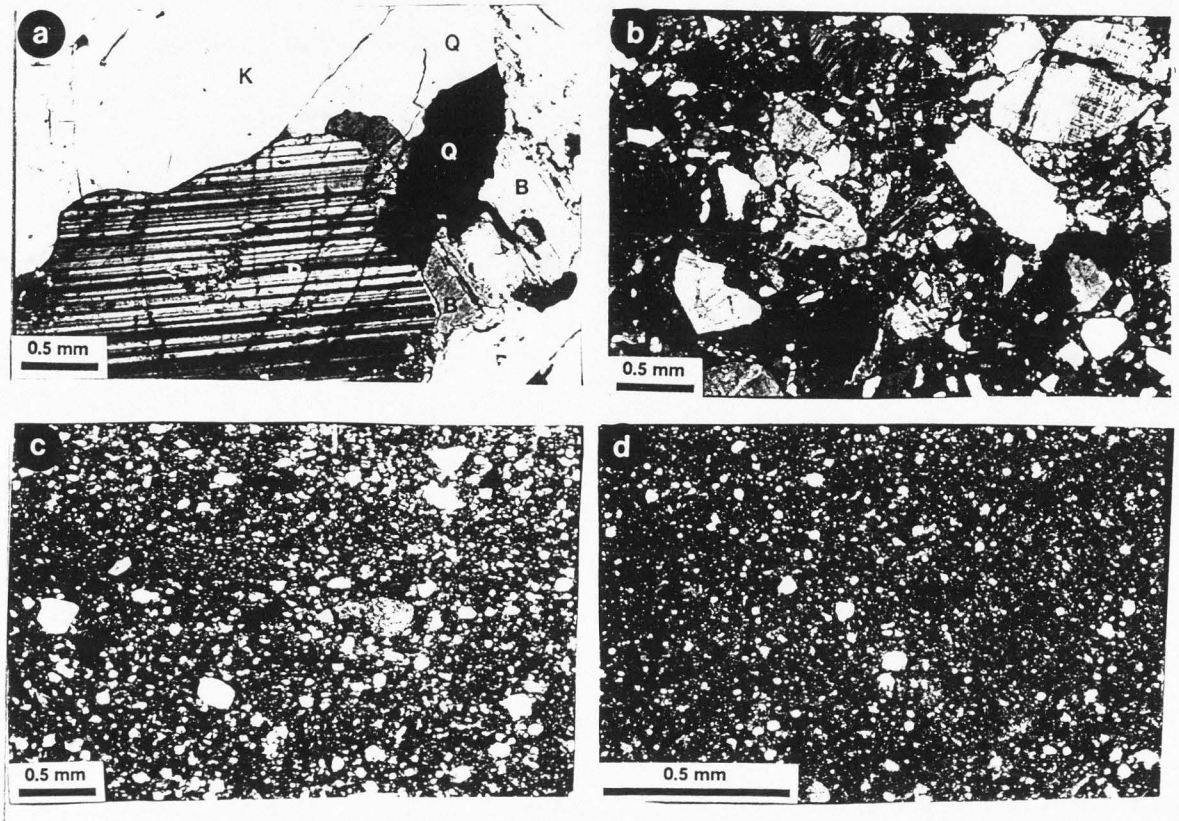

Fig. 19. Photomicrographs of typical White Rock fault zone textures. All photos taken with cross polarized light. (**a**) Protolith sample showing abundant K-feldspar (K) (mostly microcline), plagioclase (P), and quartz (Q) with minor biotite (B). Aside from minor intragranular fracturing, the protolith is basically unaltered. (**b**) Sample from protocataclasite zone. Note the decrease in grain size and the complete lack of intact grain assemblages. Sample is undergoing increased comminution. (**c**) Sample from cataclasite zone. Framework grains are mainly microcline with quartz, opaque minerals, and feldspar floating in a non-foliated matrix of fine grained mica and clay. (**d**) Sample from ultracataclasite zone showing minor framework grains (≈ 10%) of feldspar, opaque minerals, and quartz floating in a very fine grained, non-foliated matrix of clay, zeolites, and other phyllosilicates.

altered to sericitized feldspar, laumontite, montmorillonite, kaolinite, and iron oxide staining from the liberation of Fe from biotite. The protocataclasite and cataclasite matrix, albeit the grain-size is close to the limits of optical resolution, is made up mainly of comminuted quartz and feldspar (microcline & plagioclase), fine-grained micas (mostly biotite and chlorite), kaolinite, laumontite, and minor iron oxides and opaque minerals (Fig. 19b & c). X-ray diffraction was used to determine mica, zeolite, and clay content. Larger clasts of feldspar, quartz, and opaque minerals make up the framework.

The ultracataclasite matrix (material not resolvable by petrographic microscope) is made up mainly of ultra-fine-grained micas (mostly biotite), montmorillonite, laumontite, kaolinite, and minor iron oxides, quartz, and feldspars (Fig. 19d). The grain-size of the ultracataclasite matrix is beyond the limit of optical resolution, consequently X-ray diffraction was utilized to determine the composition. The ultracataclasites are composed of ≈ 1-10% framework (grains defined by petrographic scope) and ≈ 90-99% matrix. The framework is composed of ≈ 30% microcline, ≈ 30 % opaques (Ti minerals), ≈ 25% quartz, and ≈ 15% plagioclase. A relatively similar distribution of framework percentages exists in the cataclasite, suggesting that opaque minerals and microcline are the most stable minerals in the fault with quartz and plagioclase being more susceptible to chemical and brittle breakdown. The high percentage of chemically unaltered opaque minerals supports the inference that Ti-bearing minerals remained relatively chemically immobile throughout deformation (Fig. 20). The ultracataclasite is distinguished at the macroscopic scale by an extremely fine grain size, black to brown color, and the lack of porphyroclasts (Fig. 17c). Coincidentally, the White Rock ultracataclasite possesses nearly identical structure, fabrics, matrix, framework, and vein compositions as ultracataclasites from the San Gabriel strike-slip fault in southern California (Chester *et al.* 1993). Although the stress regimes differ (compressional versus strike-slip), this suggests that intrafault deformation, chemical, and fluid processes acting upon a comparable quartzo-feldspathic protolith along the White Rock fault may have been similar to those acting along the San Gabriel fault.

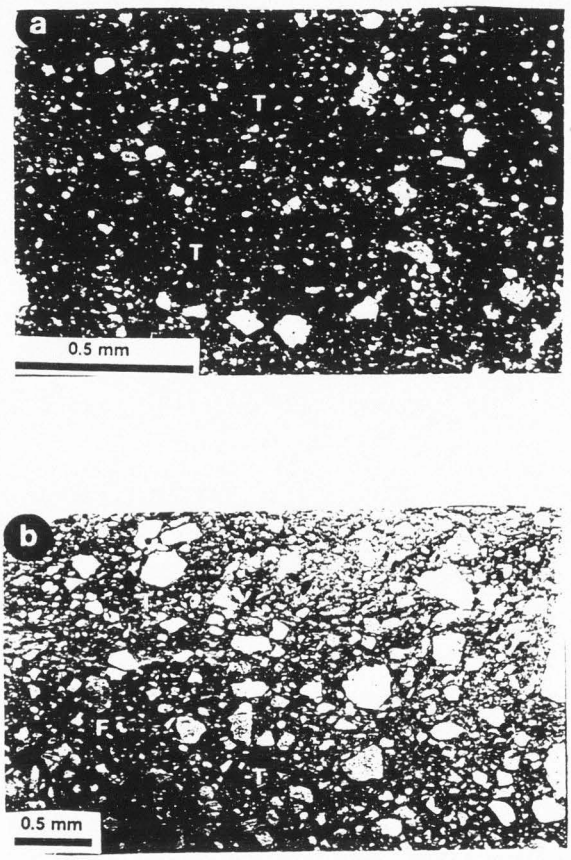

Fig. 20. Photomicrographs of ultracataclasite (**a**) and cataclasite (**b**) of the White Rock thrust. Photos show the concomitant enrichment of immobile, refractory, Ti-bearing, opaque minerals (T) floating in the matrix. Photos taken under plane polarized light. Note the crude foliation defined by the black Fe-rich veins (F) and the lack of chemical breakdown of the opaque minerals (T) in the ultracataclasite and cataclasite.

Because biotite is a weaker mineral relative to quartz and feldspar when subjected to cataclasis in the presence of fluids, it undergoes deformation at a much earlier stage. Hence, It played an important role both in terms of the deformation mechanisms and the resultant composition of the ultracataclasites. During early stages of deformation, biotite was faulted, folded, kinked, and bent as a result of the surrounding brittle failure of quartz and feldspar (Fig. 21a-d). At deformation stages between proto- and ultracataclasite, biotite was sheared (Fig. 21e) into the matrix and occasionally was stuffed (interpenetrated) by floating framework grains (Fig. 21f). Eventually, biotite makes up a large proportion of the matrix (Fig. 21g), and subsequently becomes even more susceptible to cataclastic and fluid-related breakdown into clay and other phyllosilicates.

Deformation mechanisms

The White Rock fault zone likely grew in thickness with time. That is, strain, in the form of fracturing and early-stage-cataclasis, was distributed fairly equally throughout the fault zone during the initial stages of fault evolution. This equal partitioning of strain allowed for the propagation of deformation into unaltered protolith wall rock with increasing dispacement (e.g., Hull 1988, Evans 1990b). With increasing time and deformation, the fault core developed advanced stages of comminuted material in the form of cataclasite and ultracataclasite. This process substantially weakened the highly deformed core relative to the protolith or the propagating damaged zone, and allowed for the accommodation of progressively larger strain and slip to become localized in the core. This, in effect, may have halted, or at least reduced, the often cited linear relationship between fault zone widening and displacement (see also Evans 1990b). As indicated by samples from the edges of the fault zone, deformation starts with inter- and intra-granular fracturing in both feldspars and quartz. With increased deformation, a series of closely spaced inter-granular fractures develop. These fractures generally show small amounts of shearing displacement. The fractures develop in a phacoidal pattern, eventually forming lenticular fragments. Such fragmentation, together with frictional sliding on fractures at both the

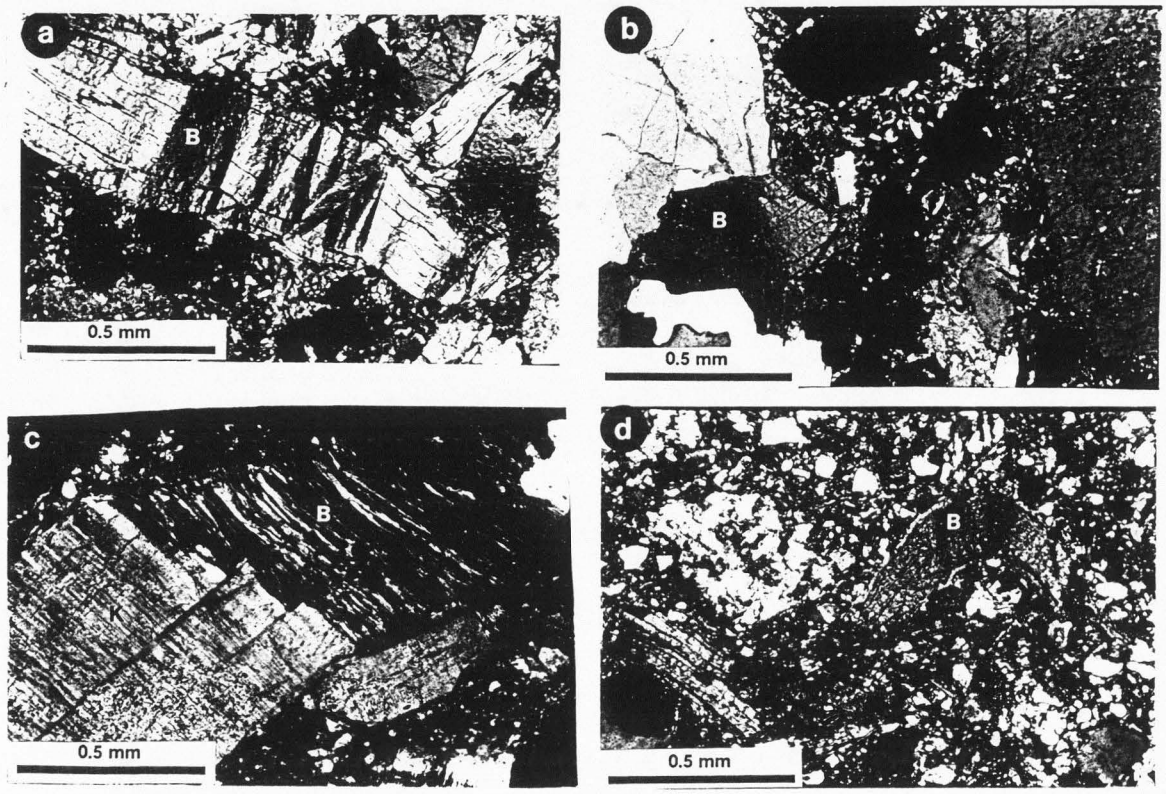

Fig. 21. Photomicrographs illustrating the progressive deformation types of biotite from the damaged zone to the ultracataclasite zone of the White Rock thrust. During the initial stages of deformation biotite (B) becomes kinked (**a**), bent (**b**), microfaulted (**c**), and folded (**d**) as a result of the surrounding brittle and cataclastic failure of quartz and feldspar. At the protocataclasite stage, biotite is sheared (**e**) and incorporated into the matrix, and occasionally is stuffed (interpenetrated) (**f**) by porphyroclasts of feldspar and quartz. Eventually, biotite makes up a large proportion of the matrix (**g**) where it becomes more susceptible to chemical breakdown.

Fig. 21. (continued).

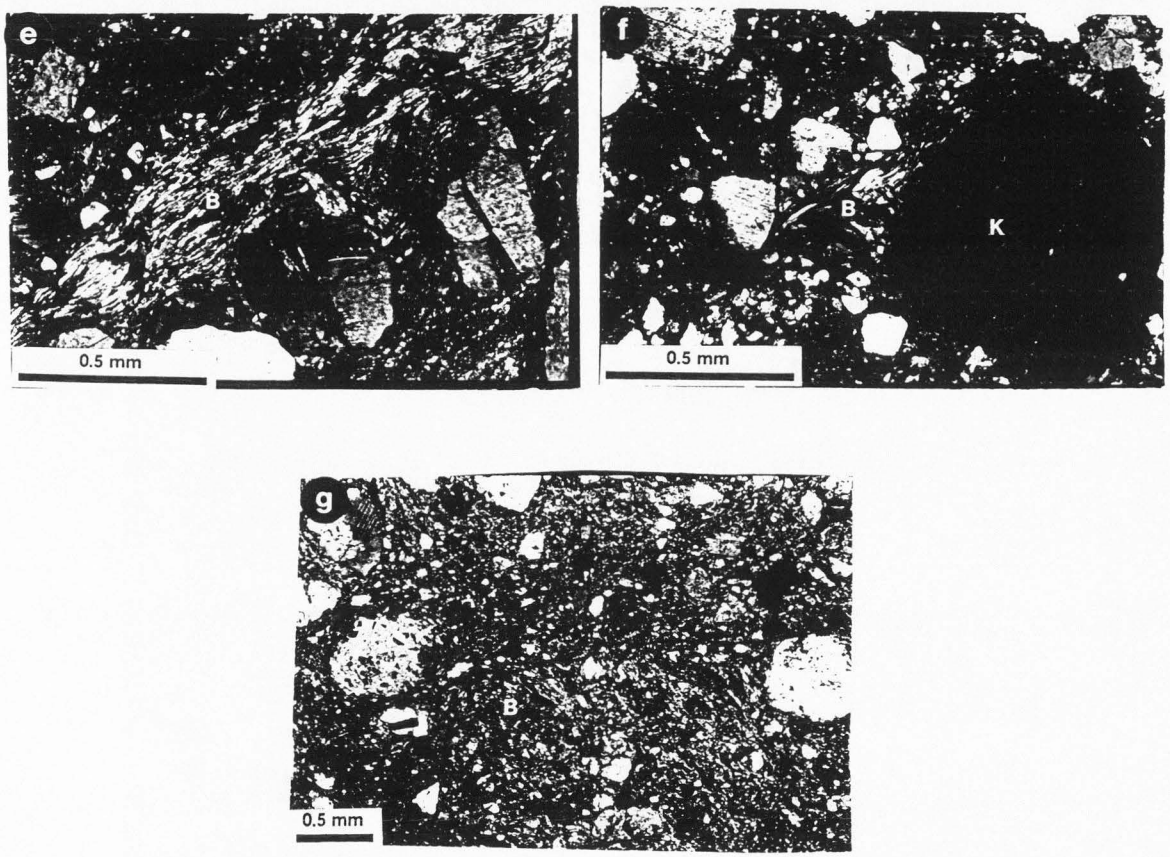

outcrop and grain scale, results in feldspar and quartz comminution and an overall reduction in grain size, leading to the formation of gouge, cataclasite and ultracataclasite in the core. Brittle fracturing and chemical breakdown continued to reduce the overall grain-size of the rock, until large, brittle framework grains are "floating" in a fine-grained cataclasite matrix. The coarse grains may continue to fracture, but these fractures are often stopped, or at least obliterated, at grain-matrix boundaries, due to ultracataclastic deformation in the fine-grained, comminuted matrix. Continued brittle breakdown of the framework grains from protocataclasite to ultracataclasite suggests that the core of the fault was under extremely high pressures. When this fine-grained condition was reached, the behavior of the matrix controlled the overall mechanical behavior of the rock. Figure 22 is a microstructural summation of the transition from unaltered protolith to ultracataclasite.

The distribution of matrix components in the ultracataclasites is indicative of some type of particulate flow mechanism (ductile ?) accompanied by grain-boundary sliding. This likely occurred under thermal pressurization in the presence of a fluid and at low effective stress (see also Chester *et al.* 1993). The low effective stress, in conjunction with high pore-fluid pressures, would allow the porphyroclasts of both the soft relict cataclasites and the hard quartz and feldspars to behave as relatively rigid, brittle particles, even to the extent that brittle fracturing occurred in the porphyroclasts while they were suspended in the matrix.

Mitra (1984) characterized the deformation within the White Rock thrust on the basis of mostly brittle or mostly ductile fracture types. The edge of the White Rock thrust is characterized by brittle fractures with little or no evidence of plastic deformation, and by the onset of grain-size reduction and strain hardening. The fractures eventually propagated under ductile conditions,with coarse grains forming a stress supported framework surrounded by a fine matrix that behaved in a ductile manner. As grain-size reduction continued, brittle grains of quartz and feldspar floated in a ductile matrix. At this point, the matrix controlled the rock behavior. The matrix was likely ductile because it flowed around brittle fragments and showed evidence of

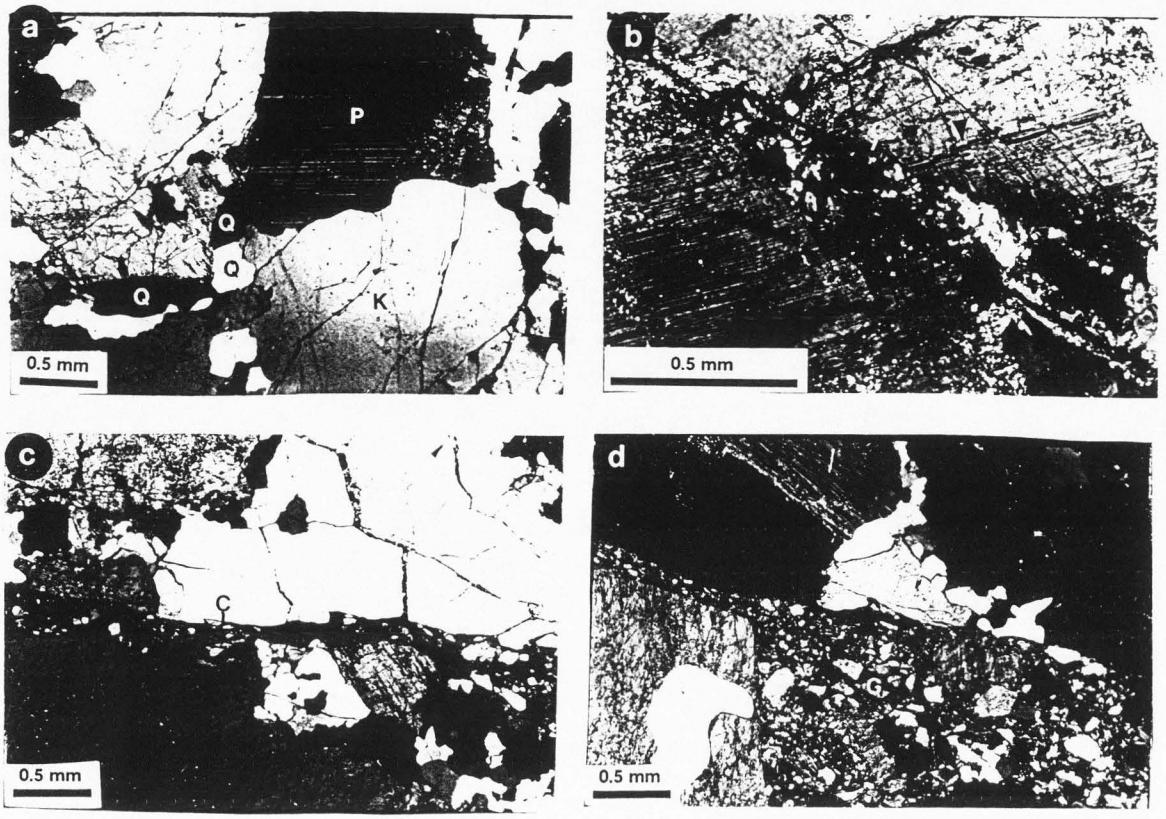

Fig. 22. Photomicrographs showing progressive deformation of rocks from protolith to ultracataclasite along the White Rock thrust. (**a**) Protolith sample showing abundant K-feldspar (K) (mostly microcline), plagioclase (P), and quartz (Q) with minor biotite (B). Protolith has only minor inter- and intragranular fracturing (cross polarizers). (**b**) Initiation of large throughgoing fractures and adjacent microfaulting (arrows) in the damaged zone with small amounts of cataclasis (C) (cross polarizers). (**c**) & (**d**) Small protocataclasite zone (C) developing in a microfault in the damaged zone (cross polarizers). Note the increased comminution of feldspar and quartz. (**e**) Deformation starts to become localized in the protocataclasites (P)(cross polarizers). Note the small zone of cataclasite (C) in which slip becomes focused and comminution is concentrated. As deformation progresses, (**f**) strain again becomes localized in the cataclasite (C), in which ultracataclasite (U) begins to form (plane polarizers). (**g**) Ultimately, this ultracataclasite zone (U) widens as strain and slip are concentrated within it (cross polarizers). At this point, matrix makes up ≈ 90% - 95% of the rock and controls the deformation of the fault. (**h**) Laumontite vein (L) cutting a K-feldspar grain (K) in the damaged zone of the White Rock thrust (cross polarizers). Note the granular nature and the presence of cleavage in the laumontite grains.

Fig. 22. (continued).

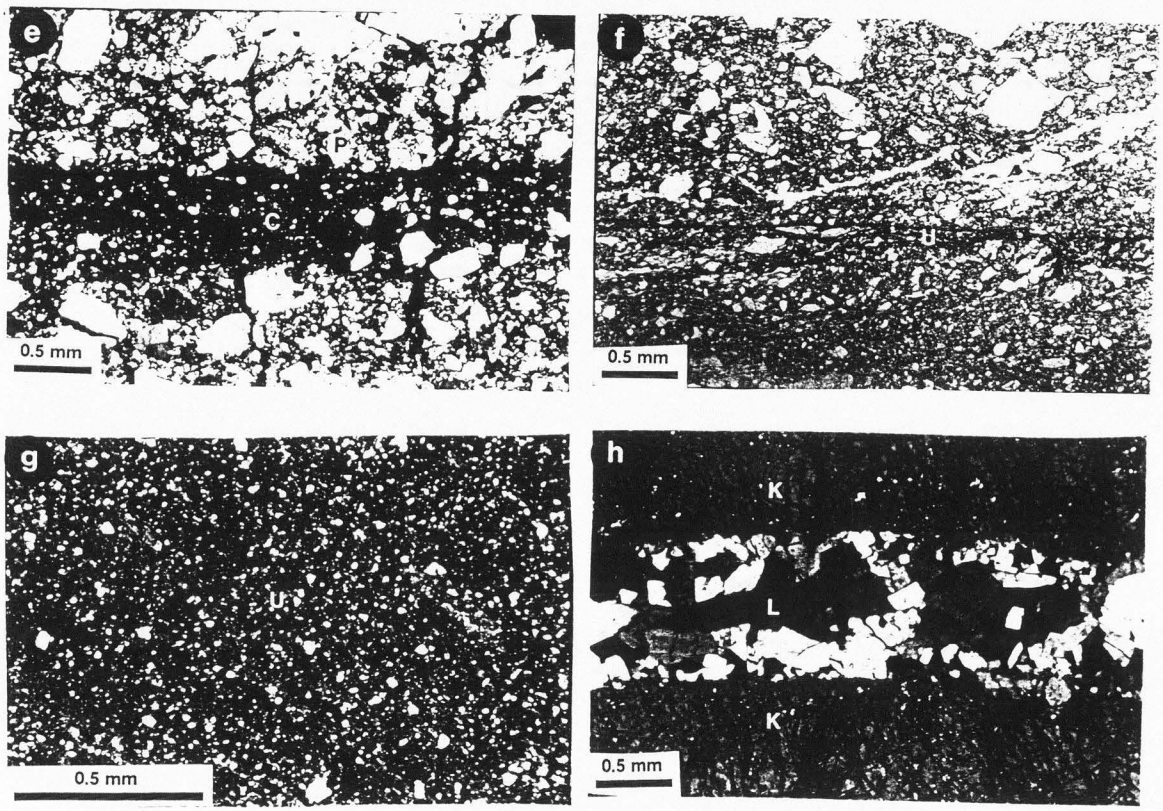

diffusional creep (pressure solution) and grain boundary sliding, which suggest the possibility of fluid influence during the late stages of deformation. Mitra (1984) suggests two stress/strain scenarios for the White Rock fault zone. The first assumes a constant strain rate with a drop in stress as dislocation graded to diffusional Coble creep as a result of grain-size reduction. The second scenario assumes stress remains constant with a strain rate increase as mechanisms changed from dislocation to diffusion. Either scenario is likely to have caused great strain localization, causing deformation to be concentrated in narrow zones. More time facilitated further grain-size reduction as the dominant deformation mechanisms changed to ductile, which was signified by diffusional Coble creep if no fluids were present, or pressure solution if fluids were present (Mitra 1984). Undeformed, thick calcite veins and relatively unaltered feldspars suggest that little or no fluids were present until the late stages of deformation (Mitra 1984). Lastly, diffusional creep likely led to strain softening, which facilitated rather large displacements localized in a relatively narrow zone (Mitra 1984).

Results of this research suggest that the dominant deformation mechanisms were brittle to semi-brittle, consisting of fracturing, faulting, and cataclasis with little evidence of Laramide-age crystal plasticity and high pressure and temperature diffusional mass transfer. Mitra (1984) suggests that the White Rock cataclasite zones deformed in a ductile manner, but cataclasis and gouge-forming processes are primarily formed by brittle to semi-brittle mechanisms assisted by fluid proccesses. Mitra (1984) also fails to account for intense syntectonic zeolite veining at most scales, the presence of clay minerals in the cataclasites, or zones of intensely deformed, veined ultracataclasites that likely accomodated most of the strain after their development. Deformation and displacement seemingly were focused along narrow zones of cataclasis. Strain hardening and grain-size reduction allowed the fault to propagate and become wider, at least until strain softening began to dominate in the fault core. Numerous, intricate networks of outcrop- to thin-section-scale, folded and faulted laumontite veins in both the damaged zone and fault core suggest large volumes of fluid played an important role in deformation.

Throughout most of the White Rock thrust's history, the core was bounded on both sides by Precambrian granitic protolith until the latest stages of faulting. That is, out of the ≈ 10 km of displacement, only ≈ 2 km of displacement occurred with sedimentary rocks in the footwall. For this reason, granitic protolith mineralogy is assumed to dominate the deformation and subsequent alteration of the fault, and that the underlying Paleozoic sedimentary rocks did not affect the fault, except for playing the role of a potential fluid reservoir.

Intra-fault fluid processes

The spatial distribution of alteration products and the apparent extreme comminution in the core of the White Rock fault suggest that fluid-rock interaction and solute transfer were enhanced within the core in response to grain size reduction and the resultant increase in grain boundary area. Within the core and the damaged zone, numerous cross-cutting sets of fractures, faults, veins, and cataclastic foliations imply repeated episodes of fluid assisted deformation. Macroscopic veining through large-aperture fractures is most dense in the damaged zone, suggesting high permeability and transport of material through this zone. Microscopic veining is less dense in the damaged zone, suggesting that fluid flow was pervasive in the damaged zone only at the macroscopic scale. Conversely, the cataclasite zones show an approximately equal density of macroscopic and microscopic veins. Macroscopic veining in the ultracataclasite layers is not obvious; however, micro-scale faulted, folded, sheared, and undeformed veins are numerous in the core. Textural and cross-cutting relations discussed below indicate that the majority of the alteration and mineralization in veins was syntectonic, albeit late stage. Older alteration and mineralization was likely obliterated by younger deformation, and this process likely was cyclic.

In the core of the fault, roughly two vein sets are present. The veins vary from irregular to planar and often are faulted, sheared, folded, refolded and truncated by other vein episodes. Veins tend to be oriented approximately parallel and perpendicular to the local foliation, with the parallel set being dominant. Laumontite veins tend to be subparallel or perpendicular to foliation.

Iron-rich veins align mostly parallel to subparallel to foliation. Most laumontite vein filling is subhedral and granular (Fig. 22h). All vein geometries are mutually cross-cutting and there are relatively few undeformed veins. Porphyroclasts in the cataclasites and ultracataclasites of the fault core are largely composed of opaques, severely altered feldspar and quartz, relict clasts of intact cataclasite and ultracataclasite from a previous cataclastic episode, and irregular pods of extremely altered and veined clasts. The abundance of existing veins near and within the fault core and of veined porphyroclasts within the fault core implies that there were numerous episodes of fracturing and vein formation followed by comminution over an extended period of time. Structures imply that the opening of vein fractures was rapid, as was their subsequent filling, and that these vein networks served as channels of focused fluid flow within the core. The distinctly greater degree of comminution in the ultracataclasites compared to the bounding wall rock is interpreted to reflect extreme localized strain and frictional sliding in the core of the fault. Extensive reworking of the ultracataclasite material is indicated by the presence of veins at all stages of mechanical fragmentation, as well as by the presence of porphyroclasts of older ultracataclasite suspended in a matrix of younger ultracataclasite. Because of continual reworking, the ultrafine-grained matrix material of the ultracataclasites may have partly been derived from recomminution of matrix material.

From microstructural observations, at least eleven episodes of deformation and fluid flow can be delineated. The sequence of events is as follows: 1) Precambrian chlorite veins acted as zones of weakness in some locations for onset of Laramide cataclasis (Fig. 23a); 2) laumontite veins formed in young fracture zones (Fig. 22h); 3) these veins were truncated with increased fracturing and faulting, leading to grain-size reduction to the point of a protocataclasite (fig. 23b & c); 4) continued comminution occurred, forming a cataclasite (Fig 19c); 5) iron oxide veins were formed in cataclasites (Fig. 23d); 6) the iron oxide veins were deformed and truncated during subsequent cataclasis (Fig. 23e & f); 7) foliated and non-foliated ultracataclasites were developed and reworked (fig. 23g); 8) laumontite veins formed mostly parallel and subparallel to

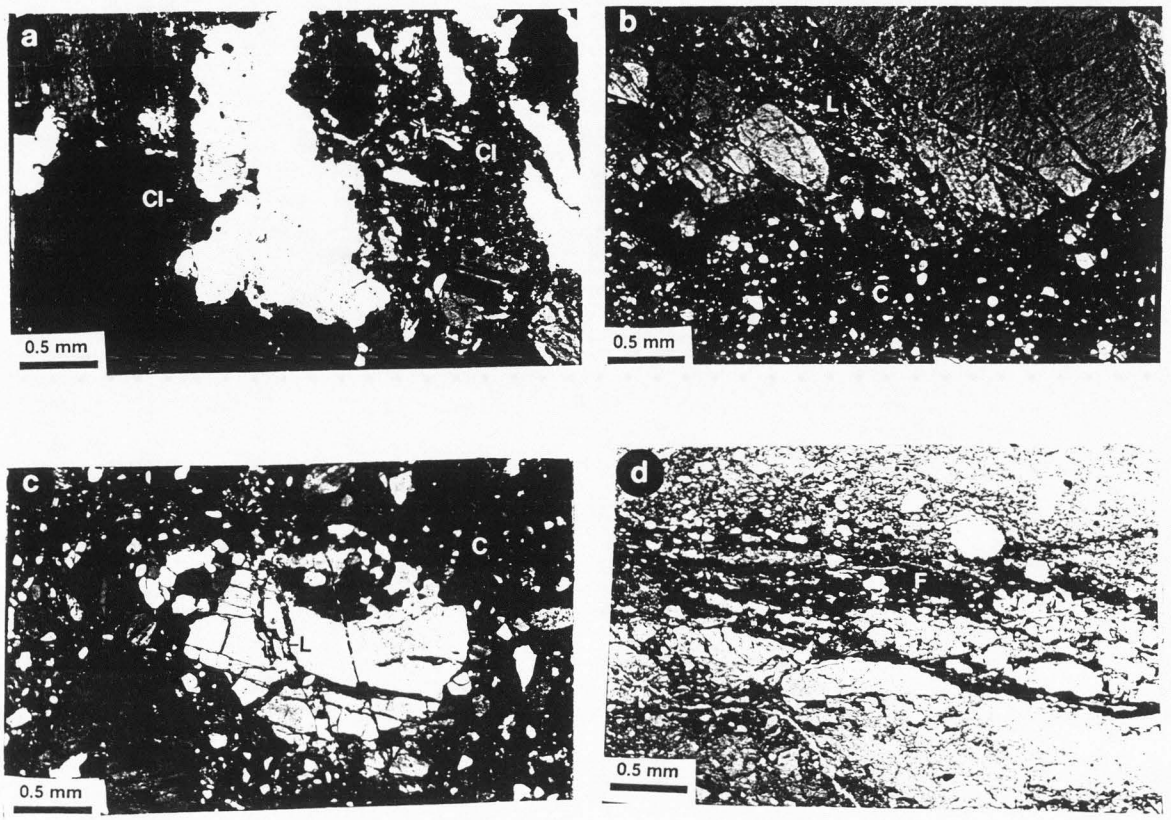

Fig. 23. Photomicrographs illustrating numerous episodes of deformation accompanied by fluid flow. (**a**) Precambrian (?) chlorite veins (Cl) showing evidence of Laramide cataclasis (cross polarizers). These zones may have acted as zones of weakness in which Laramide cataclasis was concentrated. (**b & c**) Relict damaged zone porphyroclasts with abundant laumontite veins (L) now truncated and floating in a protocataclasite and cataclasite matrix (C) (cross polarizers). (**d**) Early episode of fluid flow in which black iron oxides (F) were deposited in veins along zones of localized slip (plane polarizers). (**e & f**) Black veins (F) are eventually displaced and incorporated into the ultracataclasite (U) and cataclasite (C) matrix during ensuing cataclasis (plane polarizers). (**g**) An older ultracataclasite porphyroclast (U_C) floating in a younger ultracataclasite matrix (U) (cross polarizers). Note the crude foliation in the ultracataclasite trending approximately diagonal to the photo (from upper left to lower right). (**h**) Young laumontite vein (L) that truncates foliated ultracataclasite (U). Note the clasts of ultracataclasite floating in the laumontite vein (cross polarizers). (**i**) Photomosaic showing a laumontite vein (L_1) that parallels the foliated ultracataclasite (U_f). The laumontite vein and foliated ultracataclasite have been sheared, folded, and attenuated (cross polarizers). This vein and associated foliated ultracataclasite has then been truncated by a younger ultracataclasite (U) and laumontite vein (L_2). (**j & k**) Samples showing late stage episode of high-angle shearing that truncates all textures in the ultracataclasites (U_f), cataclasites, and protocataclasites (**j** = plane polarizers, **k** = cross polarizers).

Fig. 23. (continued).

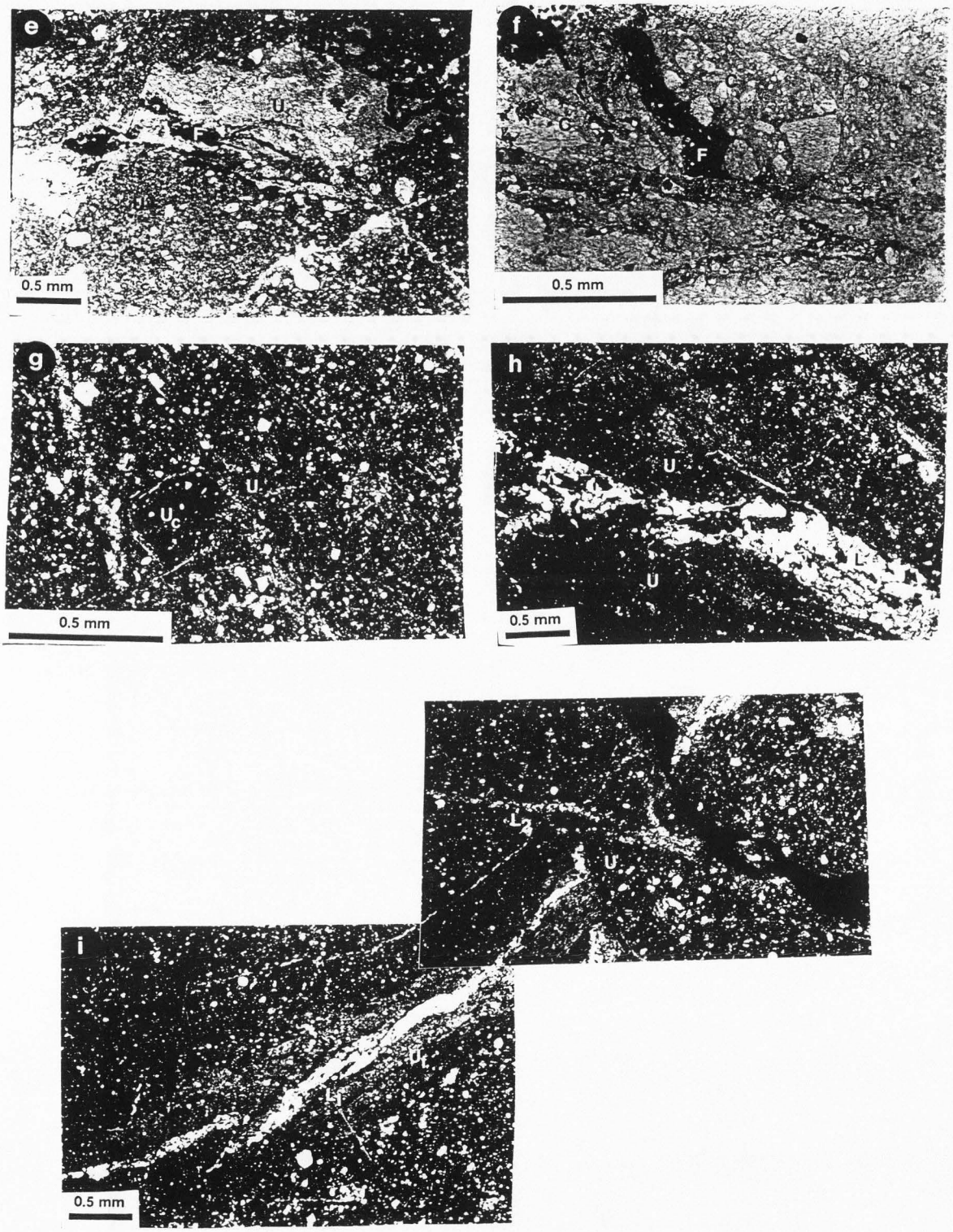

Fig. 23. (continued).

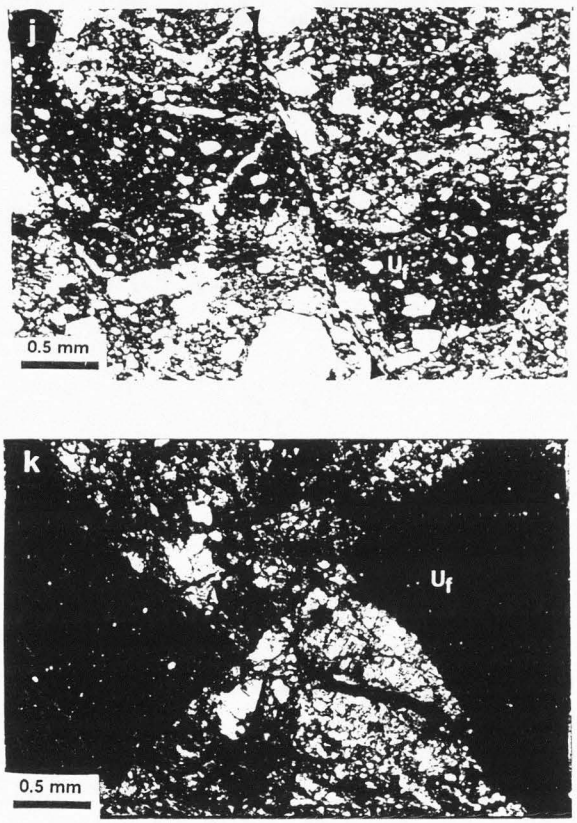

the ultracataclasite foliation (Fig. 23h); 9) laumontite veins and adjacent foliated ultracataclasites were sheared, folded, and truncated by continued ultracataclasis (Fig. 23i); 10) another laumontite vein episode occurred, cutting all foliation and older veins (Fig. 23i); 11) an episode of high-angle-to-foliation shearing occurred (Fig. 23j & k), which may have been caused by Reidel shear or the propagation of strain from the underlying massively folded carbonates in the footwall.

No macroscopic calcite veins were observed. Few microscopic calcite veins were observed, and those veins were post-tectonic and completely undeformed. Although excellent fault exposures north of Flat Top Mountain (up structural section) are few, observations suggest that fluid flow was not as extreme, reactive, or pervasive. In fact, the fault zone deformation resembles that of the East Fork fault zone. Zones of laumontite, iron oxide, and chlorite veins are still abundant, but intense, thick zones of fluid-influenced cataclasite and ultracataclasite deformation are not observed.

FRACTURE ANALYSES

Fracture Orientation and Length

In general, two to three times more fractures were observed at the thin-section scale than at the macroscopic scale (Fig. 24a-d). At the macroscopic scale, fractures were concentrated at angles between ± 30° to the faults (Fig. 24a-b). Fractures from slabs cut parallel to the fault slip direction tended to be concentrated at angles subparallel to the plane of the fault, giving rise to the diamond-shaped pattern that was observed. Fractures from slabs cut perpendicular to the fault slip direction tended to be mostly concentrated at angles subparallel to the plane of the fault, but with an increase in fractures at angles subperpendicular to the fault plane, giving rise to the blocky-shaped pattern that was observed. Thin-section scale fractures were concentrated at angles between ± 30° to the faults for networks from slabs cut parallel to the fault slip direction (Fig. 24c). However, fractures on fault-perpendicular slabs still show slight

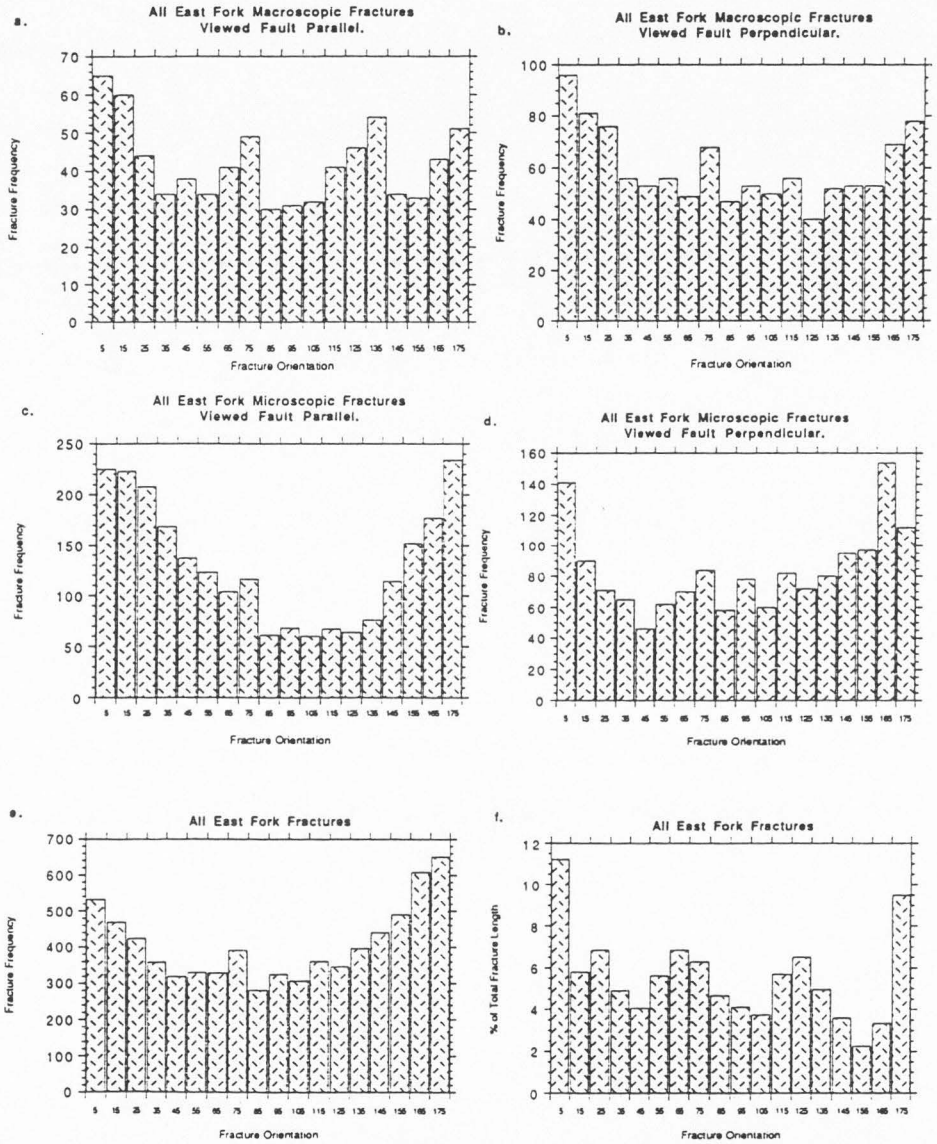

Fig. 24. Histograms showing the frequency distribution (**a-e**) and percentage length distribution (**f**) with respect to fracture orientation as measured from a two-dimensional surface. For all histograms 0° is equivalent to fault planar and 90° to fault perpendicular. The majority of all fractures and the majority of total fracture length at both the macro-and microscopic scales are at fault-subparallel orientations.

concentrations at low angles to the fault, but high concentrations at high angles to the fault also are common (Fig. 24b). Regardless of the scale, most fractures are concentrated at angles subparallel to the fault plane (Fig. 24e). Also, approximately 40% of the total fracture length of all fractures measured is concentrated in the same azimuthal interval of ± 30° (Fig. 24f).

These statistical results suggest that the effective fluid flow direction in the fault zone is roughly between ± 30° to 40°, or subparallel to the fault, regardless of scale. Based on field observations, most fluid-influenced mineralization occurs in the same azimuthal interval. That is, most silica and laumontite vein filling is found in fractures that are at an angle between ± 40° to the plane of the fault. Fractures at high angles to the fault transmit fluids, though not to the extent of subparallel fractures, which facilitate the thickening of the fault by speeding the brittle deformation process in the protolith wall rock.

Fractal Box Counting

The box counting method (both the Barton & LaPointe methods) helps quantify fracture "filledness," or the manner in which fractures fill space in a two-dimensional area. The LaPointe box counting method, because it incorporates fracture density into the calculation, better characterizes spatially varying density differences. Regardless, both box counting methods provide a fractal dimension, **D**, that not only suggests scale invariance of the spatial and density distribution of fractures over the scale studied, but the value also describes the filledness of the area with respect to fractures. That is, as an area becomes increasingly filled with fractures, **D** proportionally increases.

The fractal analysis of fault zone fractures in the East Fork area resulted in scale-invariant fractal dimensions of 1.23 to 1.81 using the Barton method, and 2.19 to 2.50 using the LaPointe method (Fig. 25). Both methods show that the higher the **D**, the more filled the area is with fractures. Thus, for fracture distributions in the East Fork study area, a value of 1.81 indicates an intensely fracture-filled area over the scale of observation, and a **D** value of 1.23 corresponds to an area sparsely filled with fractures (Fig. 26). Fractures are not self-similar and scale-invariant

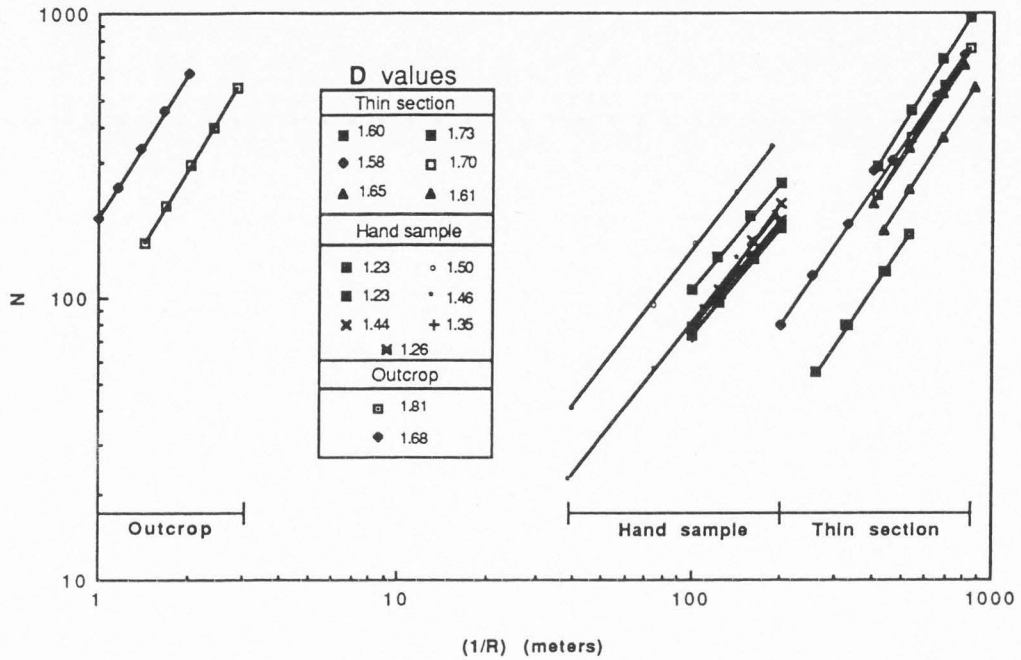

Fig. 25. Graph showing results of the Barton box counting method over the scale of thin section to outcrop for samples studied in the East Fork fault damaged zone. Fractal dimensions (**D**) for each analysis are listed in table in center of graph. Fractal dimensions are greater for thin-section and outcrop scale fractures than for hand sample scale fractures. The grid, using the box counting method, was consistently oriented such that a side of the grid was always parallel to the fault.

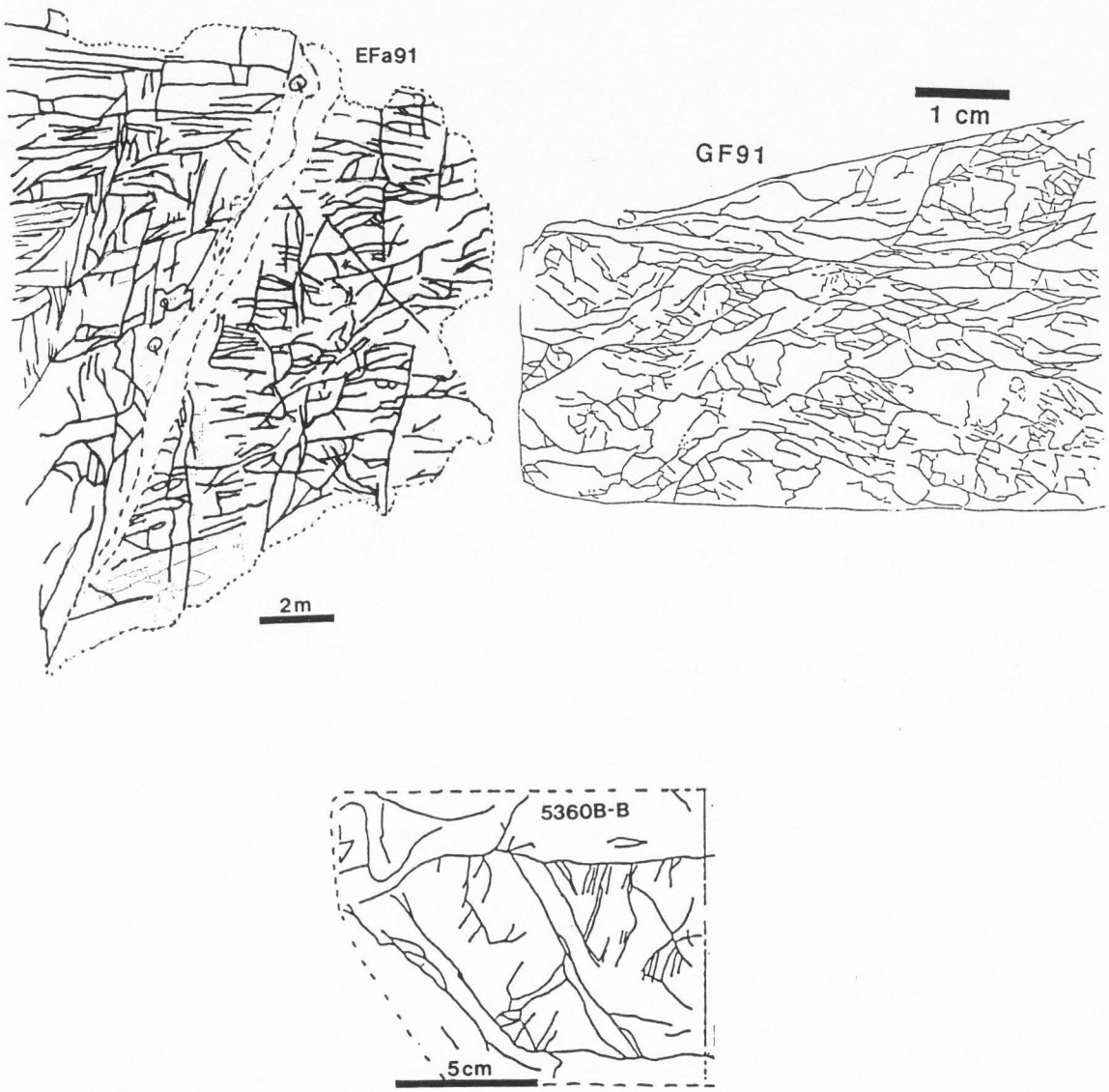

Fig. 26. Fracture trace maps that illustrate the physical difference between box counting fractal dimensions. EFa91 (outcrop) (see Fig. 7a) has a fractal dimension of 1.81. GF91 (thin section) has a fractal dimension of 1.73. 5360B-B (hand sample) has a fractal dimension of 1.23.

from the scales of outcrop to thin-section (Fig. 25). That is, **D** at thin-section and outcrop scale ranges from 1.58 to 1.81 (Barton method) and 2.30 to 2.50 (LaPointe method), whereas hand sample **D** values range from 1.23 to 1.50 (Barton method) and 2.19 to 2.40 (LaPointe method). This result suggests that the area observed at hand sample scale is less fracture-filled than adjoining outcrop and thin-section scales. This could be a result of sampling bias, or simply a consequence of fracture propagation mechanisms in this area that, for the most part, bypass the hand-sample scale. Fracture mechanisms imply that fractures densely propagate at the thin-section scale, then at some critical point, stress and strain become localized and fractures coalesce into large outcrop scale fractures, consequently circumventing the intermediate hand sample scale.

Notwithstanding, the box counting fractal methods do appear to depict the filledness or rough spatial distribution of a given fracture network in two-dimensional space. Unfortunately, the method does not divulge any information about variations in relative clustering or spatial distribution with respect to orientation and does not simultaneously characterize orientation, trace length, density, and interconnectivity. More research with larger data sets is needed to fully substantiate these findings.

Linear Fractal Analysis

The Cantor dust linear fractal method modified for this research depicts the spatial distribution of fractures with respect to orientation. The method also gives a reliable description of relative clustering along any given orientation. That is, the higher the fractal dimension, the more evenly the fractures are spaced along the oriented analysis line. The smaller the fractal dimension, the more spatially clustered the fractures are along the line. The Cantor fractal dimension depicts the spatial distribution (relative clustering) in linear space.

An example of the linear fractal analysis is shown in Figs. 27 & 28. Additional results are listed in the Appendix. Fractal dimensions for the East Fork fault range from 1.10 (clustered fractures) to 1.69 (fairly uniform distribution of fractures) over the scale of thin-section to outcrop.

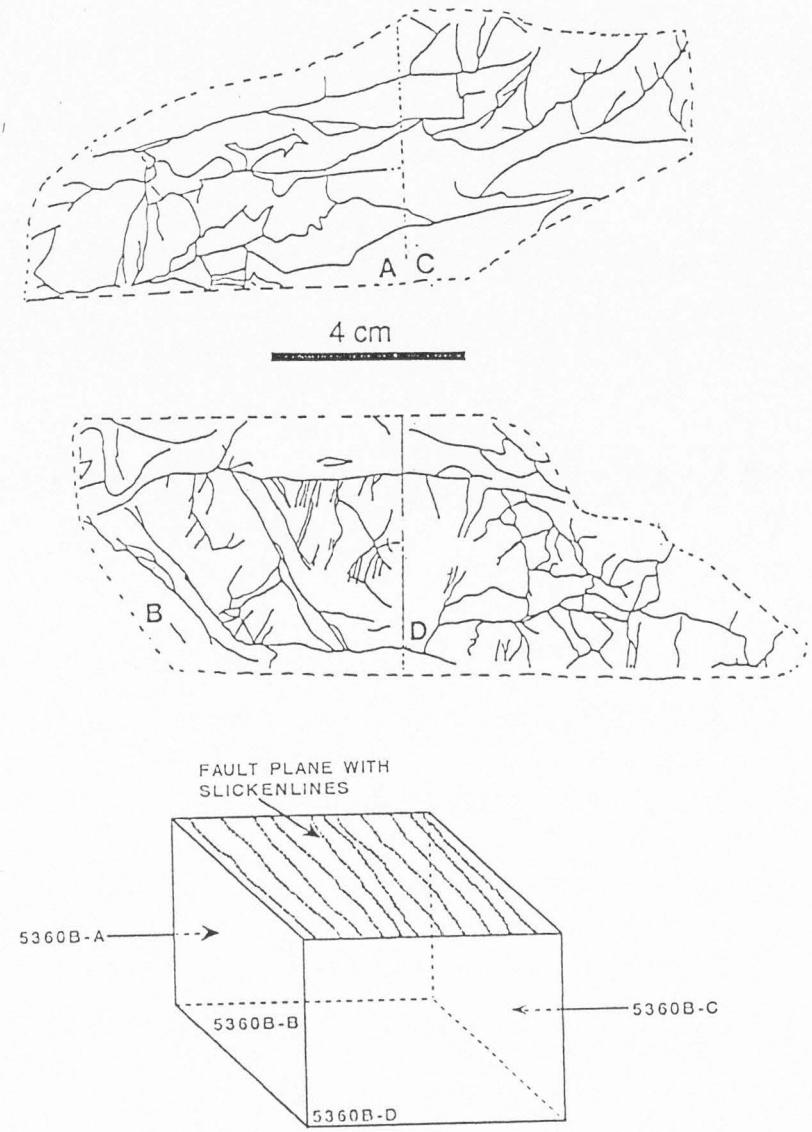

Fig. 27. Fracture trace maps, statistical, and fractal results for hand sample 5360B of the damaged zone adjacent to a gouge/cataclasite zone in the East Fork fault. (**a**) Line drawings of fractures from faces slabbed parallel to slip direction and perpendicular to the fault plane (5360B-B & 5360B-C) and faces slabbed perpendicular to slip direction and perpendicular to the fault plane (5360B-A & 5360B-D). Fractures are mainly transgranular with interspersed intragranular fractures. (**b**) Orientation frequency histograms for fracture trace maps for Sample 5360B. (**c**) Fractal ellipses for fracture trace maps of sample 5360B. Fractal dimensions are listed in parentheses below the orientation of the analysis line. (**d**) Normalized fractal ellipses for fracture trace maps of sample 5360B. Normalized fractal dimensions are listed in parentheses below the orientation of the analysis line. For the most part, dimensions are greater at high angles to the fault, suggesting uniform fracture clustering and higher fracture densities in angles subparallel to the fault. Remember that the analysis line measures fractures that mostly intersect the line at a high angle. These results correlate with orientation distributions and visual comparison with the trace maps, suggesting credibility of the method.

Fig. 27. (continued).

b

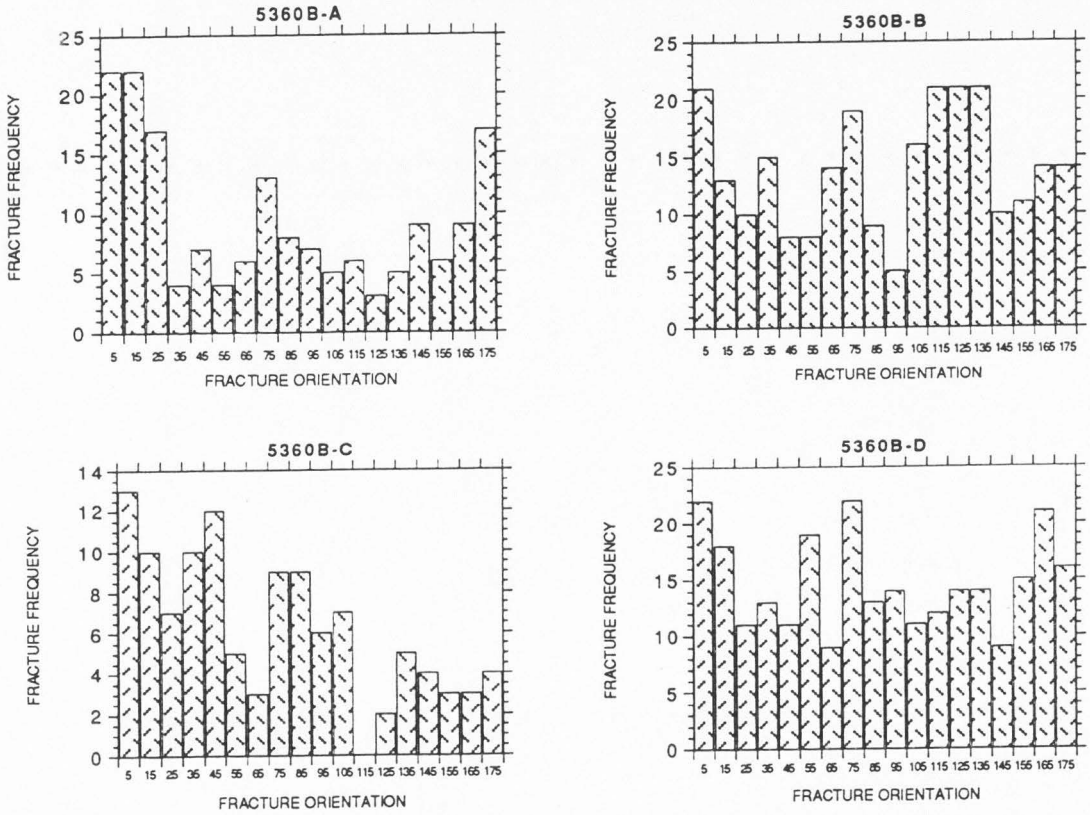

Fig. 27. (continued).

c

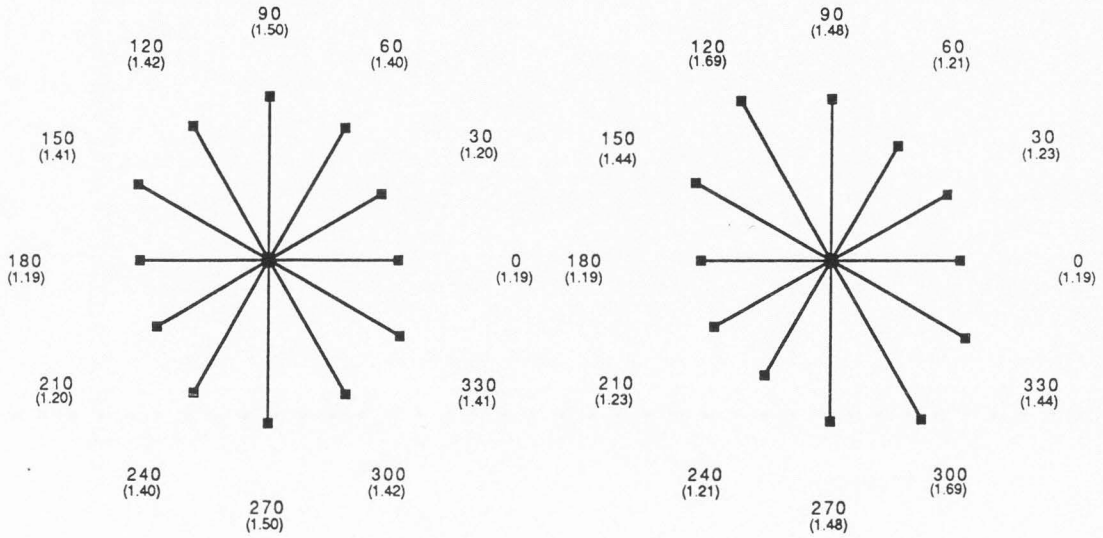

5360B-A Fractal Ellipse

5360B-B Fractal Ellipse

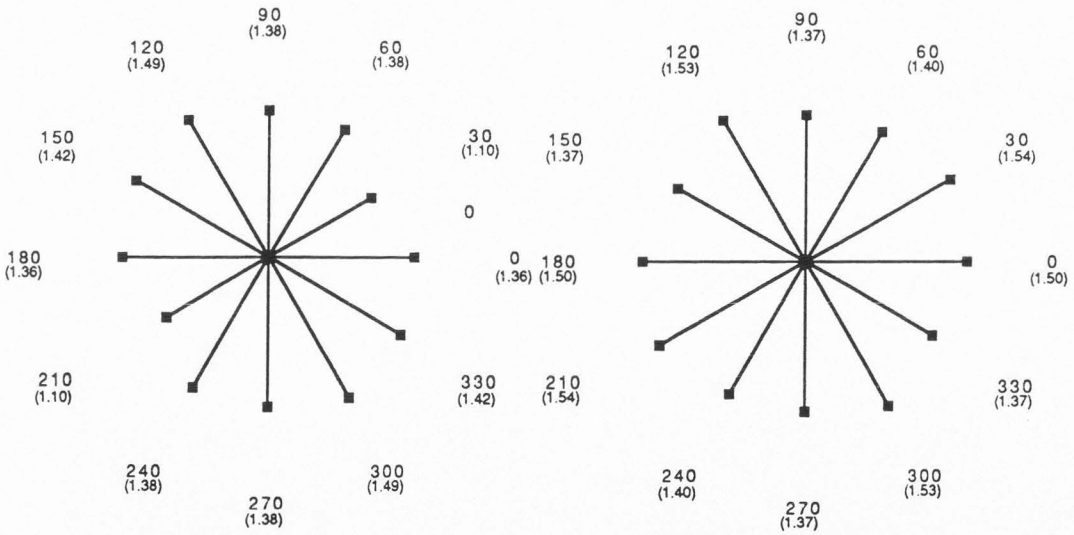

5360B-C Fractal Elliipse

5360B-D Fractal Ellipse

Fig. 27. (continued).

d

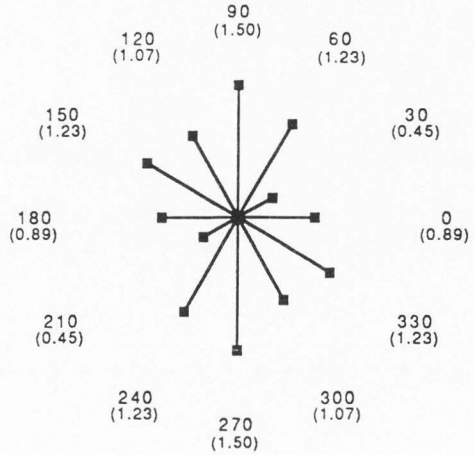

5360B-A Normalized Ellipse

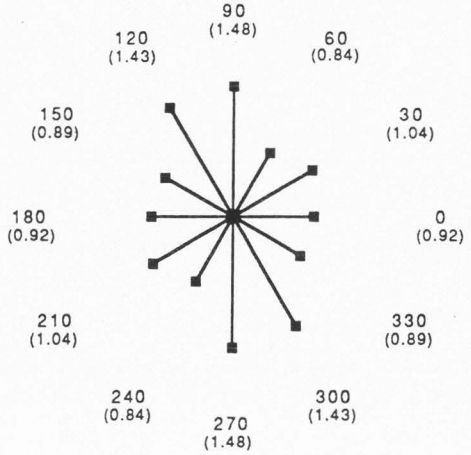

5360B-B Normalized Ellipse

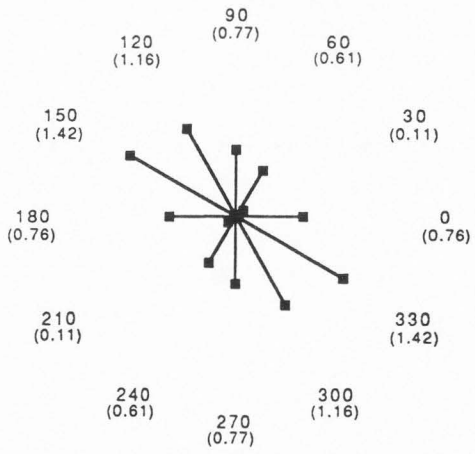

5360B-C Normalized Ellipse

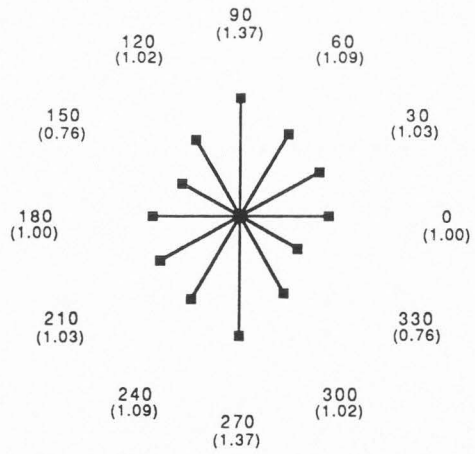

5360B-D Normalized Ellipse

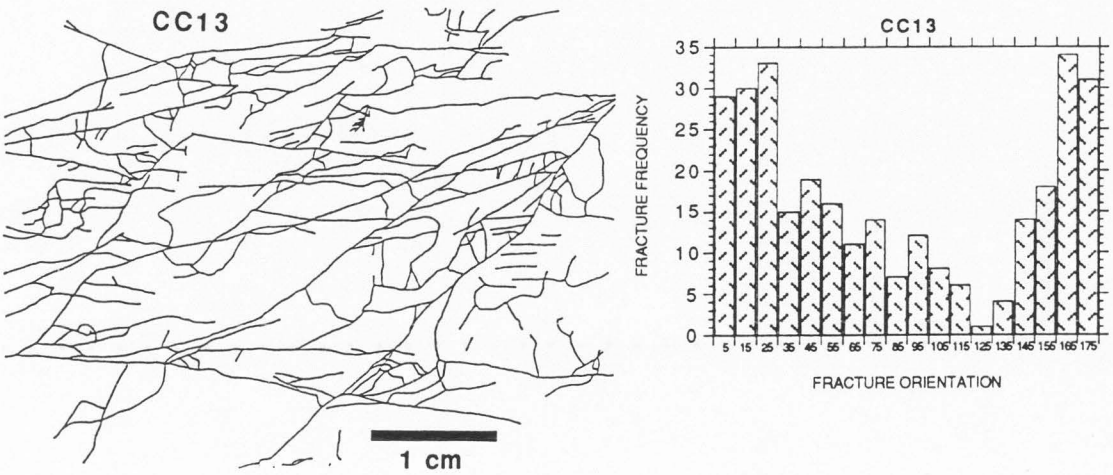

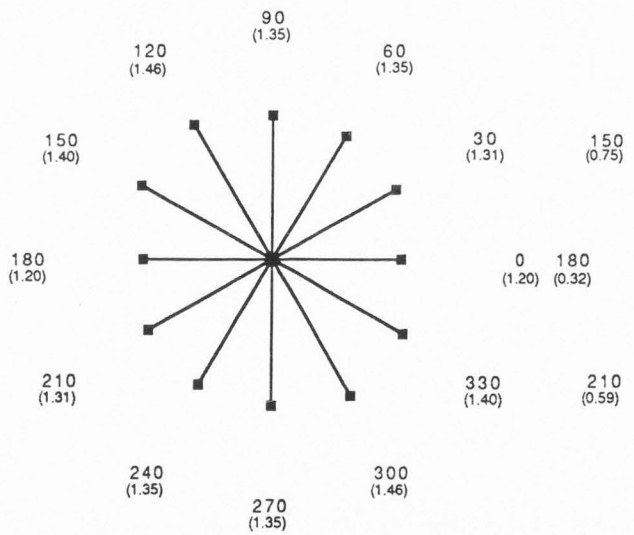

CC13 Fractal Ellipse

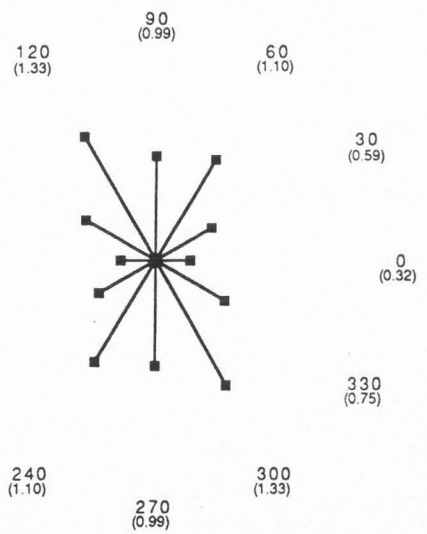

CC13 Normalized Ellipse

Fig. 28. Fracture trace map, orientation frequency histogram, fractal ellipse, and normalized fractal ellipse for thin section sample CC13. Map face slabbed parallel to slip direction and perpendicular to the fault plane in the East Fork damaged zone adjacent to a gouge/cataclasite zone. Fractures are transgranular that, in turn, connect zones of intragranular fractures.

High **D** values were typically acquired at orientations between 30° and 150°, which corresponds to fracture uniformity in the directions of ± 60° to the fault (**D** is a measurement of fractures that are primarily sub-perpendicular to the analysis line). Whereas, low **D** values are at orientations of ± 60°, suggesting non-uniform clustering in the directions of 60° to 120° to the fault.

This linear fractal analysis characterizes the degree of relative clustering along an analysis line, but does not take into account the number of fractures encountered along that same line. The normalized value, **D'**, depicts both clustering and fracture quantity, as it varies with orientation. The normalized dimension, **D'**, ranges from 0.11 to 1.58 in all samples. A value of 0.11 reflects a low number of fractures that are unevenly spaced. A value of 1.58 corresponds to dense fractures that are evenly spaced.

Thin sections have consistently larger values of **D'** in any given direction than do hand-sample fractures (Fig. 28) due to a higher density of fractures at the thin-section scale. In like manner to **D**, large **D'** values are typically oriented between 30° and 150°, which corresponds to fracture uniformity and high density in the directions of ± 60° to the fault, whereas, low **D'** values are at orientations of ± 60°, suggesting non-uniform clustering and low density in the directions of 60° to 120° to the fault. This contrast is less obvious at the hand-sample scale, implying both low fracture density and the lack of a dominant fracture orientation at this scale (Fig. 27).

In terms of differences with respect to the orientation of the two-dimensional fracture network relative to the fault (i.e., slabs cut parallel or perpendicular to slip direction of fault), both **D** and **D'** are distinctly higher at 60° to 120° than other orientations to the fault for parallel networks. Perpendicular networks have large **D** and **D'** values at orientations both subparallel and subperpendicular to the fault with no distinctive preferential orientations. Again, these contrasts are less distinct at the hand-sample scale.

Because fracture clustering, orientation, and density are taken into account, a possible rough correlation is suggested between the results offered by this linear fractal method and two-dimensional fracture permeability. For example, a numerical flow model was used to calculate the

relative maximum and minimum permeability directions in two directions for sample CC13, as shown by Fig. 29 (Forster & Evans 1991). Subsequently, the sample was analyzed using linear fractal analysis. For this sample, the maximum permeability direction is roughly perpendicular to the maximum **D'** value (Fig. 29). A similar relation exists for the minimum permeability direction and the minimum **D'** value. Thus, a possible relation between relative permeability and **D'** values can be inferred such as:

$$k \perp D'$$

or, at least for this case;

$$k_{max} \perp D'_{max} \quad \text{and} \quad k_{min} \perp D'_{min}$$

This relationship is not so much a function of absolute fractal values (**D** or **D'**), but rather a function of the entire fractal vector ellipse when portrayed as a whole. Obviously, more research is required to verify, or nullify, this relationship. Flow modeling must be computed at more than two angles to better describe the directional permeability structure of fracture networks. This is planned in future research, but is beyond the scope of this research.

Contrary to the findings of some authors of fractal work (e.g., Barton & Hsieh 1989, LaPointe 1988, Velde *et al.* 1991), fractal analysis does not appear to be a comprehensive statistical method that can explain everything about fracture mechanisms, distributions, and permeability. Rather, the methods can be used as a supplement to other characterizations (e.g., orientation, trace length, density, roughness, spacing, aperture, and mineralization). In the case of this research, a means to generate a more realistic synthetic network has been developed by integrating new types of fracture analyses into synthetic network generators and numerical fluid flow models. Thus, fractal analyses can be used as a check or constraint in a synthetic network generator. That is, as the generator creates a synthetic network based on other statistical parameters (e.g., paramaterized orientation, trace length, density, and aperture distributions), it

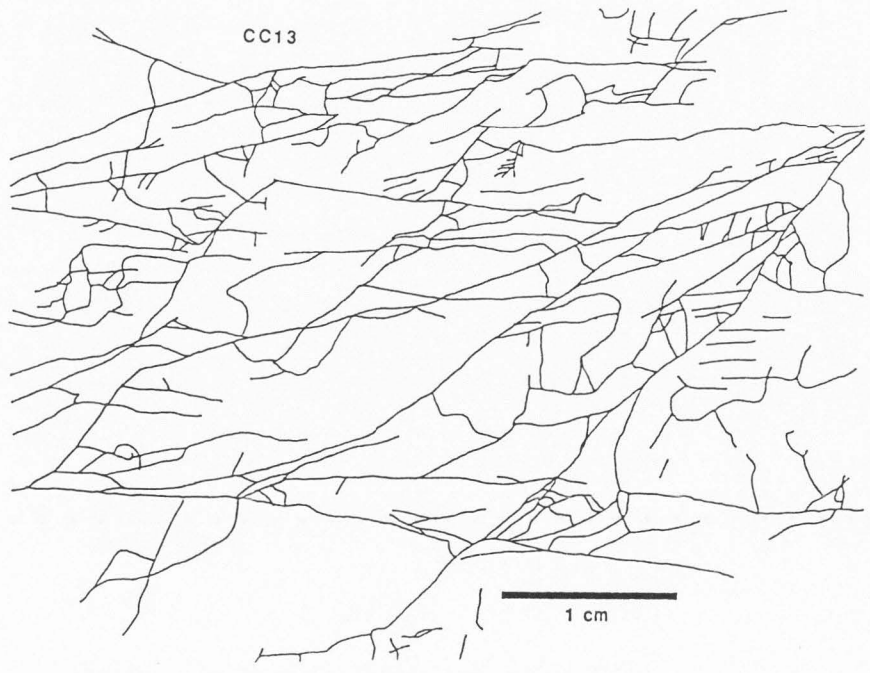

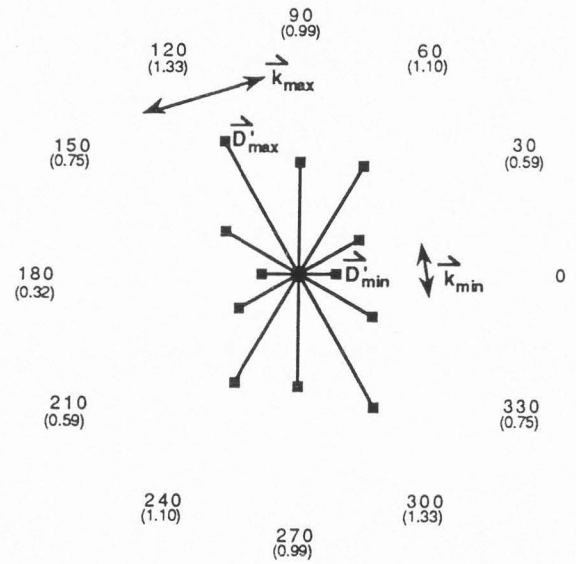

CC13 Normalized Ellipse

Fig. 29. Fracture trace map and normalized fractal ellipse for thin section sample CC13 showing permeability-fractal relation. Map face slabbed parallel to slip direction and perpendicular to the fault plane in the East Fork damaged zone adjacent to a gouge/cataclasite zone. Fractures are transgranular that, in turn, connect zones of intragranular fractures. Sample CC13 was subjected to a numerical fracture flow model in which relative maximum and minimum permeability directions were measured in two orientations. The normalized fractal ellipse (bottom) is labeled with the directions of those results (k_{max} & k_{min}) and the maximum and minimum fractal values (D'_{max} & D'_{min}). For this sample, maximum and minimum permeability directions are roughly perpendicular to the maximum and minimum fractal vectors.

also calculates the resultant network's fractal dimension using both the box counting and Cantor linear fractal methods. If the fractal dimension falls within prescribed values, e.g., 1.60 to 1.81 (Barton box counting) for thin-section scale networks, then the network is accepted. If not, the generator can spatially redistribute the network, while retaining the same statistical framework, until the proper fractal dimension is obtained.

GEOCHEMISTRY

Twenty-six samples were subjected to whole rock geochemical analysis. These results are summarized in Tables 1 and 2. In order to document the chemical changes across the East Fork and White Rock faults as a function of increasing deformation and water/rock interaction (from protolith to fault core), samples were collected along detailed traverses across the faults at several outcroppings. A comparison of White Rock thrust values from Table 2 indicates a substantial enrichment in TiO_2, MgO, MnO, and P_2O_5, and a depletion in SiO_2 from protolith to fault core, suggesting possible large volume losses. On the other hand, up structure, the East Fork compositions remain relatively constant from protolith to gouge/cataclasite zone, suggesting only minor volume losses, if any at all (Table 1).

As discussed previously, the likely open system behavior of the fault zones requires that a reference frame be established for normalizing the data. Although the low abundance of TiO_2 makes it more susceptible to analytical error, for this study, Ti (as TiO_2) is inferred to be the most immobile constituent within the fault zone, and geochemical analyses are normalized and calculated relative to assumed immobile TiO_2.

Fault Zone Component Gains and Losses

As illustrated by a Sinha-type diagram using immobile TiO_2 and equation 12, traverses across the East Fork fault zone from protolith to gouge/cataclasite indicate moderate losses in SiO_2, Al_2O_3, CaO, Na_2O, and K_2O and moderate gains of Fe_2O_3, MgO, and LOI (Lost On Ignition = primarily trapped H_2O & CO_2) in the damaged zone (Fig. 30a). In contrast, the

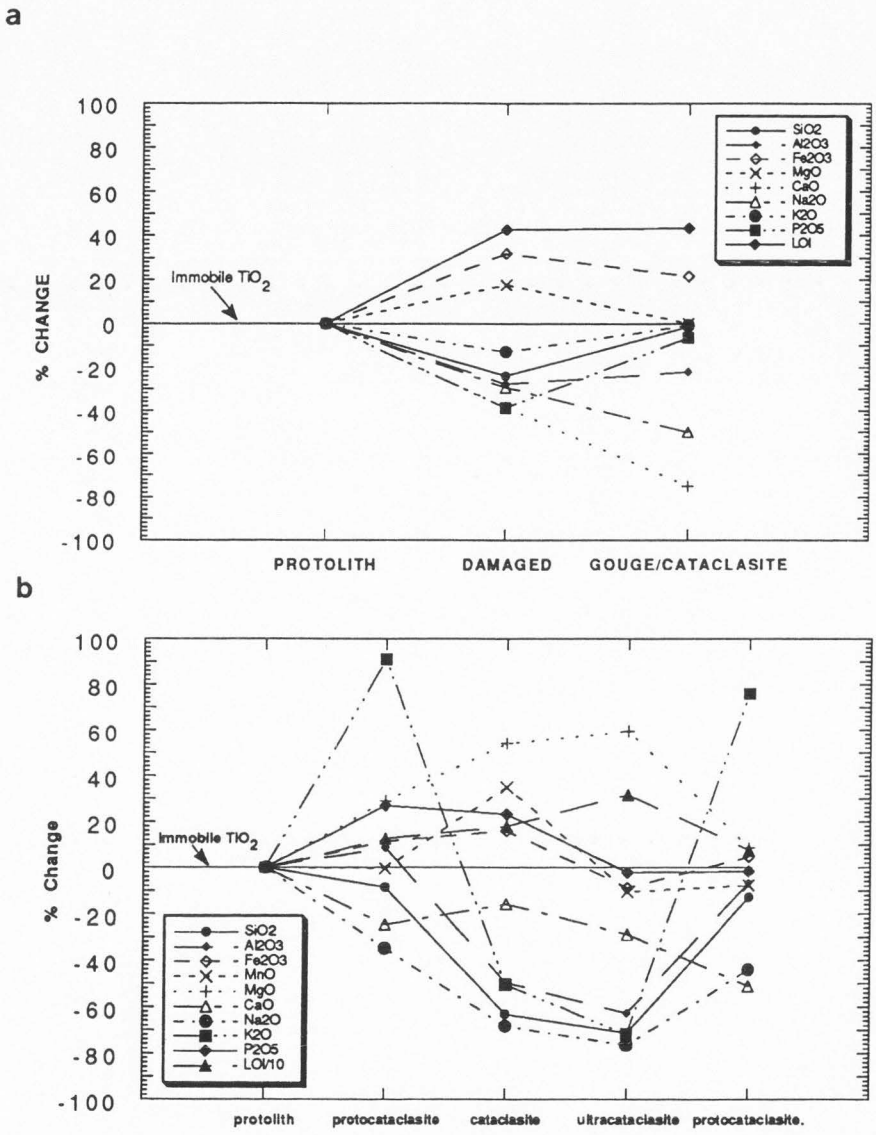

Fig. 30. Percentage change diagram for traverses across the East Fork (**a**) and White Rock (**b**) faults showing percentage change in oxides after normalization of data to constant (immobile) TiO_2. 0% corresponds to TiO_2 behavior assuming no change has occurred across the fault. Significantly more loss occurred in the White Rock fault than the East Fork faults.

gouge/cataclasite zone indicates near isovolumetric behavior for SiO_2, MgO, and K_2O accompanied by increased losses in Na_2O and CaO. Fe_2O_3 and LOI remain mostly unchanged from the damaged zone. With regards to spatial location, protolith samples were extracted from 50 m to 200 m from the fault core and damaged zone samples from 50 m to 1 m from the core.

Losses in the damaged zone can be explained by the breakdown of feldspars into sericite, clays, and other phyllosilicates. Then, fluids flowing through the open system may have flushed out the aqueous components, thus imposing a moderate volume loss in the damaged zone. Many of the damaged zone macro- and microscopic fractures are filled and lined with kaolinite and Fe-Mg oxides (from the breakdown of biotite and hornblende), explaining the gains in Fe_2O_3 and MgO in the damaged zone. An increase in LOI can be explained by the increase of syntectonic clays and other phyllosilicates created from the breakdown of feldspars.

With the exception of the behavior of SiO_2 and K_2O, other oxides follow the same trends in the gouge/cataclasite zone as the damaged zone. Abundant quartz veins and indurated gouge and cataclasite (indurated by silica cementation) suggest that large amounts of silica/Fe-saturated fluids flowed through the East Fork fault system. Because of the extremely fine-grained nature of the gouge and cataclasite zone, permeability and flux through this zone were likely not great. Thus, this zone was likely saturated with fluids, and the silica and Fe_2O_3 subsequently precipitated in the zone. This would explain the increase in SiO_2 in the gouge/cataclasite zone relative to the damaged zone. The apparently large volume of silica in the quartz veins and indurated gouge/cataclasite in the East Fork fault zone likely cannot be accounted for simply based on volume losses in this stretch of the fault zone. It is likely that a portion of the silica was transmitted by fluids from elsewhere, possibly from deeper structural levels along the same fault system where the solubility of silica is greater.

Figure 30(b) also shows a Sinha diagram illustrating chemical differences across a traverse along the White Rock thrust. This plot shows steady losses in SiO_2, Al_2O_3, CaO, and Na_2O of up to 75% from protolith to ultracataclasite. Generally immobile components, such as

MnO, Fe_2O_3, and P_2O_5, either remain mostly unchanged or gain slightly from the protolith to ultracataclasite. Conversely, K_2O gains by about 90% in the protocataclasite zone, thenit drops and follows the trend of the other alkalies in the cataclasite zone. LOI steadily increases towards the ultracataclasites.

The breakdown of quartz, feldspar, and biotite into kaolinite, montmorillonite, laumontite, and other phyllosilicates and the subsequent flushing of the mobile components by fluids can explain the large losses in silica and alkalies and the gain of LOI in the fault core. At the same time mostly immobile components, such as TiO_2, MnO, MgO, P_2O_5 remain relatively unchanged. As pointed out previously, microcline is likely one of the most stable minerals during deformation in the fault zone. Thus, the behavior of K_2O in the protocataclasite zone can be explained by the chemical stability of microcline relative to quartz and plagioclase. This shows a concomitant increase in K_2O when, in fact, other components are decreasing relative to K_2O. As deformation proceeds, microcline also begins to chemically breakdown, and K_2O then begins to follow the same losing trend as the other alkalies in the cataclasite zone.

Fault Zone Reactions

The decrease in silica and alkalies is consistent with the breakdown of feldspars and the release of these components to a fluid phase. Chemical reactions leading to the chemical breakdown and alteration to kaolinite, montmorillonite, and laumontite in the faults may include those described below:

1) Quartz → dissolved silica (Garrels & Christ 1965, Faure 1991).

$$\underset{\text{quartz}}{SiO_2} + H_2O \rightarrow \underset{\text{dissolved silica}}{H_4SiO_4}.$$

2) Albite → kaolinite (Faure 1991).

$$\underset{\text{albite}}{2NaAlSi_3O_8} + 9\,H_2O + 2H^+ \rightarrow \underset{\text{kaolinite}}{Al_4Si_4O_{10}(OH)_8} + 2Na^+ + \underset{\text{dissolved silica}}{8H_4SiO_4}.$$

3) Albite → laumontite (Faure 1991).

$$\underset{\text{albite}}{2NaAlSi_3O_8} + Ca^{2+} + 4H_2O \rightarrow \underset{\text{laumontite}}{CaAl_2Si_4O_{12}{\cdot}4H_2O} + 2Na^+ + \underset{\text{amorphous}}{2SiO_2}.$$

4) Anorthite → laumontite (Faure 1991).

$CaAl_2Si_2O_8 + 2H_4SiO_4 \rightarrow CaAl_2Si_4O_{12}{\cdot}4H_2O$
anorthite dissolved silica laumontite

5) Microcline → kaolinite (Garrels & Christ 1965).

$2KAlSi_3O_8 + 2H^+ + 9H_2O \rightarrow Al_2Si_2O_5(OH)_4 + 4H_4SiO_4$
microcline kaolinite dissolved silica

6) Laumontite ↔ Kaolinite (Faure 1991).

$CaAl_2Si_4O_{12}{\cdot}4H_2O + H_2O + 2H^+ \leftrightarrow Al_2Si_2O_5(OH)_4 + Ca^{2+} + 2H_4SiO_4$
laumontite kaolinite dissolved silica

7) Biotite → kaolinite (Faure 1991).

$2K(Mg^{2+},Fe^{2+})AlSi_3O_{10}(OH)_2 + 10CO_2 + \square O_2 + 8H_2O \rightarrow Al_2Si_2O_5(OH)_4 + 2Fe(OH)_3 +$
biotite kaolinite
$4Mg^{2+} + 10HCO_3^- + 4SiO_2.$

8) Kaolinite ↔ Mg-montmorillonite (Faure 1991).

$7Al_2Si_2O_5(OH)_4 + 8SiO_2 + Mg^{2+} \leftrightarrow 6[(Al_2)(Si_{3.67},Al_{0.33})O_{10}(OH)_2]Mg^{2+}_{0.167} +$
kaolinite Mg-montmorillonite
$7H_2O + 2H^+.$

9) Kaolinite ↔ K-montmorillonite (Faure 1991).

$7Al_2Si_2O_5(OH)_4 + 8SiO_2 + 2K^+ \leftrightarrow 6[(Al_2)(Si_{3.67},Al_{0.33})O_{10}(OH)_2]K_{0.33} +$
kaolinite K-montmorillonite
$7H_2O + 2H^+.$

Note that most of these reactions occur in the presence of water and the reactions typically liberate relatively large amounts of silica into solution.

Fault Zone Volume Loss

Figure 31(a) shows a Grant diagram for the East Fork damaged zone. The constant mass isocon and constant volume isocon both have a slope of 1 ($\rho^{fa}_{dam.}/\rho^{pr}$ = 2.62/2.62). The immobile isocon is best-fit through TiO_2, Zr, Fe_2O_3, and MgO and leads to a slope of 1.29. Using equations 9 and 10, mass and volume loss in the damaged zone is ≈ 22%. Because of the scatter of some of the more immobile elements (e.g., Sr), volume loss likely ranged from 0% to 22%. However, the Ti slope of 1.29 will be used in future calculations.

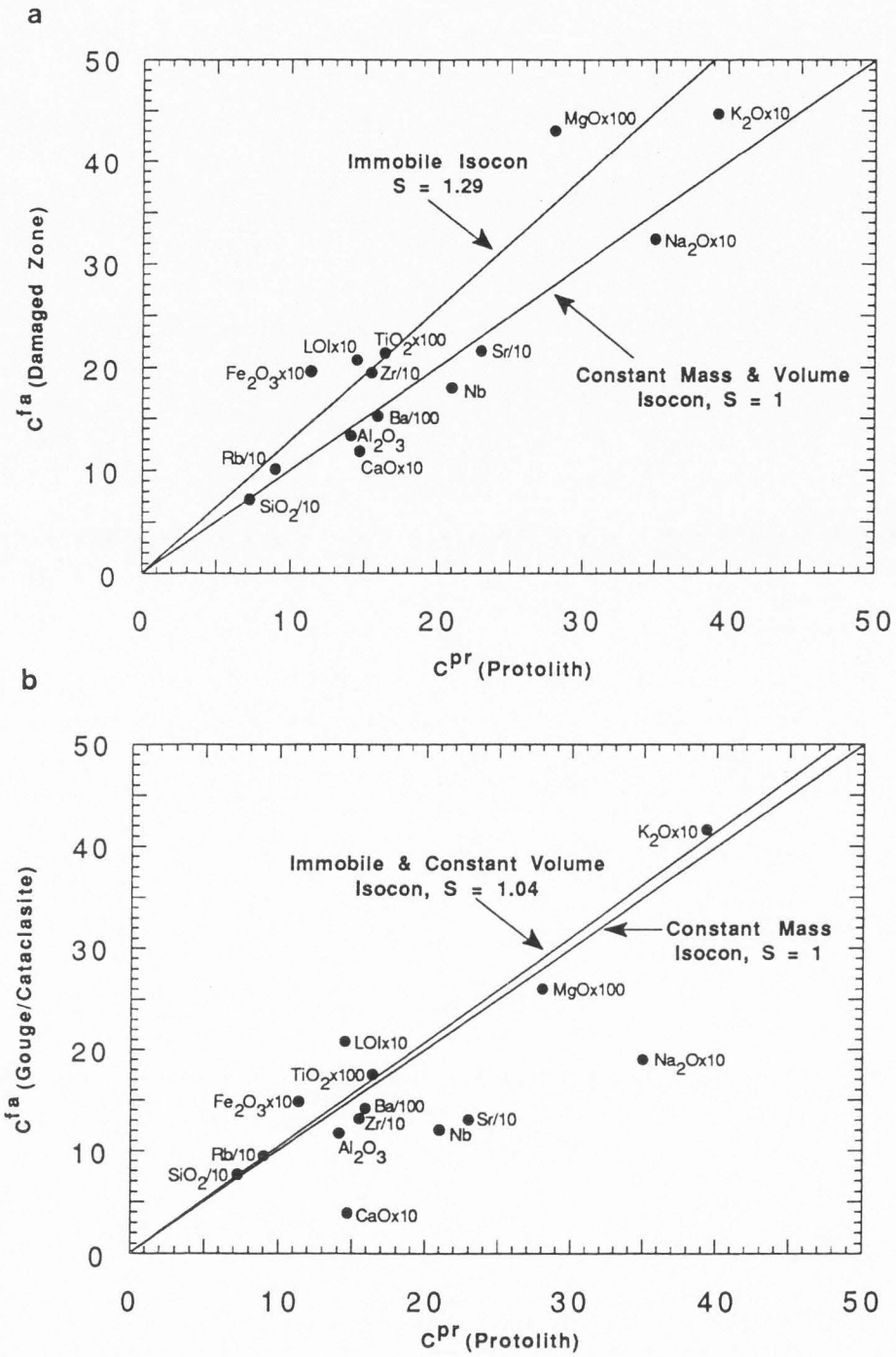

Fg. 31. Grant-type plot of average composition of protolith granite versus average composition o fault core rocks for the East Fork fault damaged zone (**a**) and gouge/cataclasite zone (**b**). Concentrations (C) are in wt% (oxides) and ppm (trace elements) scaled arbitrarily (so as to maintain slope) to fit on the plot. For the damaged zone, the best-fit immobile isocon has a slope of 1.29, which is equivalent to a mass and volume loss of 22%. Error analysis suggests loss may range from 0% to 22%. For the gouge/cataclasite zone, the constant volume slope equals the best-fit immobile isocon with a slope of 1.04. This is equivalent to a mass loss of 29% (range, 0% to 3%) and 0% volume loss.

Using the immobile isocon slope of 1.29 to calculate the volume factor (f_v)(equation 11), the associated densities, the associated chemical compositions, and equation 5, the following balanced component equation can be written for the East Fork damaged zone:

100 g protolith granite - 18.6 g SiO_2 - 4.1 g Al_2O_3 - 0.6 g CaO - 1.1 g Na_2O - 0.6 g K_2O → 74.6 g damaged rock + 0.3 g Fe_2O_3 + 0.1 g LOI.

The balanced equation indicates moderate losses in SiO_2 and Al_2O_3 with negligible losses in CaO, Na_2O, and K_2O, and small gains in Fe_2O_3. Components with negligible losses or gains of < 0.01 g were not listed in the balanced equation.

Figure 31(b) shows the Grant diagram for the East Fork gouge/cataclasite zone. In this case, the constant mass isocon has a slope of one, and the constant volume isocon has a slope of 1.04 ($\rho^{fa}_{gouge}/\rho^{pr}$ = 2.72/2.62). The immobile isocon is best-fit through TiO_2, Zr, Fe_2O_3 and MgO and leads to a slope of 1.04, nearly identical to the constant volume isocon. Using equations 9 and10, mass loss equals ≈ 2.9% with no volume loss in the gouge/cataclasite zone. The balanced component equation for the East Fork gouge/cataclasite is:

100 g protolith granite - 2.75 g Al_2O_3 - 1.1 g CaO - 1.7 g Na_2O → 92.0 g gouge/cataclasite + 1.5 g SiO_2 + 0.3 g Fe_2O_3 + 0.1 g K_2O + 0.6 g LOI.

Because the damaged zone is a precursor of the gouge/cataclasite zone, it is expected to find the same chemical trends in the gouge/cataclasite zone. This is mostly the case, excepting the behavior of silica. Rather than becoming more depleted in the gouge/cataclasite zone relative to the damaged zone, silica is actually enriched. Again, this can be explained by the infiltration, saturation, and precipitation of silica/Fe-saturated fluids into the gouge/cataclasite.

Figure 32 shows a Grant diagram for the White Rock thrust ultracataclasite zone. Because assumed immobile components typically, in this case, plot above the isovolume isocon, two possibilities are suggested. The first hypothesis suggests that these highly immobile components were added to the system presumably by a fluid phase. The second hypothesis suggests that, in fact, these components remained relatively immobile and other, more soluble, components such as silica and the alkalies have been depleted relative to the immobiles. The second hypothesis is more plausible, considering the immobility of such phases as TiO_2, and is applied hereafter. Thus, a more plausible isocon can be best-fit through the immobile components suggesting that components plotting below this immobile isocon have been removed from the system relative to the protolith. The loss of soluble components would produce a concomitant increase in the immobile components, thereby explaining their enrichments. Coincidentally, the TiO_2 point plots directly on the best-fit immobile isocon for all Grant diagrams. In this case, the constant mass isocon has a slope of one, and the constant volume isocon has a slope of 0.95 ($\rho^{fa}_{ultra.}/\rho^{pr}$ = 2.62/2.75). The immobile isocon is best-fit through TiO_2, MnO, MgO, and P_2O_5, and leads to a slope of 2.77. Using equations 9 and 10, mass loss is ≈ 64% and volume loss is ≈ 66% (ranging from 36% to 77%). The balanced component equation for the East Fork gouge/cataclasite is:

100 g protolith granite - 50.7 g SiO_2 - 8.9 g Al_2O_3 - 0.2 g Fe_2O_3 - 0.7 g CaO - 2.8 g Na_2O - 2.7 g K_2O → 31.7 g ultracataclasite + 0.3 g MgO + 2.0 g LOI.

Gains or losses of other components were negligible.

There have been large volume losses in the White Rock thrust, suggesting that tremendous fluid fluxes removed large amounts of the mobile components (SiO_2, Al_2O_3, K_2O, Na_2O, and CaO) from the system. The large losses of silica and alkalies are consistent with the

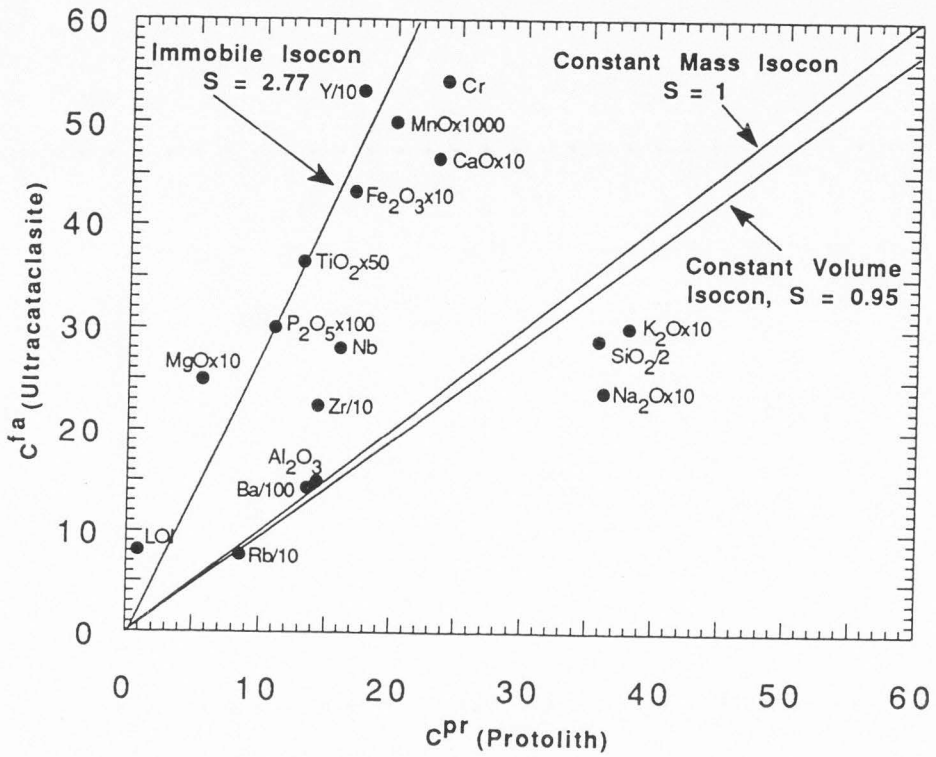

Fig. 32. Grant-type plot of average composition of protolith granite versus average composition of ultracataclasite for the White Rock fault. Concentrations (C) are in wt% (oxides) and ppm (trace elements) scaled arbitrarily (so as to maintain slope) to fit on the plot. The best-fit immobile isocon has a slope of 2.77, which is equivalent to a mass loss of 64% and a volume loss of 66%. Error within analysis suggests volume loss may range from 36% to 77%. Volume loss in the cataclasite zone is slightly lower (≈ 50% -60%).

breakdown of quartz, feldspar, and biotite to kaolinite, montmorillonite, and laumontite and the removal of the resulting released aqueous components.

Fluid/Rock Ratios

Because the chemical behavior documented above indicates much fluid/rock interaction, fluid/rock ratios can be calculated if the following criteria are known or can be assumed: 1) silica loss can be calculated from equation 5; 2) saturation of the fluid with respect to silica ranged from 0% (initial fault infiltration) to 90% (latter stages of fluid/fault evolution); and 3) an estimated fault temperature (leading to silica solubility), fluid/rock weight, and volume ratios required to produce the observed silica depletions can be calculated using equations 13 and 19. The fluid/rock ratio (**N**) is the amount (either weight or volume) of chemically active water that is required to remove the calculated loss in silica from a weight or volume of rock. Fluid/rock ratios are actually only a minimum value for the quantity of water passing through the rock, in that the ratios do not take into account the fluid that does not chemically interact with the wall rock, or fluid that is 100% saturated with respect to silica.

Fluid/rock ratios for the East Fork damaged zone and White Rock ultracataclasite zone were calculated using equations 13 and 19 with observed silica depletions (L_{Si}) of 18.6 g silica per 100 g rock (East Fork damaged zone) and 50.7 g per 100 g rock (White Rock ultracataclasite zone), silica solubilities corresponding to a range of fault zone temperatures from 350°C to 150°C (Table 3), and saturation with respect to silica ranging from 0% to 90%. These values are summarized in Table 4.

Fluid/rock weight ratios (N_W) for the East Fork damaged zone ranged from ≈ 76 (T = 350°C, s = 0%) to ≈ 12,400 (T = 150°C, s = 90%). That is, 76 masses of water are required to remove 18.6% of the silica from one mass of rock if the temperature is 350°C and the water is 0% saturated with respect to silica. Fluid/rock volume ratios (N_V) for the East Fork damaged zone ranged from ≈ 201 (T = 350°C, s = 0%) to ≈ 32,700.(T = 150°C, s = 90%). That is, 201 volumes of

Table 4. Fluid/rock weight and volume ratios as they relate to varying temperatures and silica saturation regimes for the East Fork and White Rock faults. Temp. (°C) is the temperature within the fault zone, Sat. is the saturation of fluid with respect to silica, N_W is the fluid/rock weight ratio, and N_V is the fluid/rock volume ratio.

White Rock thrust L_{Si} = 50.7g/100g				**East Fork fault** L_{Si} = 18.6g/100g			
Temp. (°C)	Sat.	N_W	N_V	Temp. (°C)	Sat.	N_W	N_V
350	0%	207	569	350	0%	76	201
"	40%	345	949	"	40%	127	335
"	70%	690	1900	"	70%	253	668
"	90%	2070	5690	"	90%	759	2000
300	0%	355	976	300	0%	130	343
"	40%	591	1630	"	40%	216	570
"	70%	1180	3250	"	70%	434	1150
"	90%	3550	9750	"	90%	1300	3440
250	0%	677	1830	250	0%	245	647
"	40%	1110	3060	"	40%	408	1080
"	70%	2220	6120	"	70%	816	2150
"	90%	6670	18300	"	90%	2450	6460
200	0%	1330	3670	200	0%	489	1290
"	40%	2220	6120	"	40%	816	2150
"	70%	4450	12200	"	70%	1630	4310
"	90%	13300	36700	"	90%	4900	12900
150	0%	3380	9300	150	0%	1240	3270
"	40%	5630	15500	"	40%	2070	5460
"	70%	11300	31000	"	70%	4130	10900
"	90%	33800	93000	"	90%	12400	32700

water are required to remove 18.6% of the silica from one volume of rock if the temperature is 350°C and the water is 0% saturated with respect to silica.

Based on cross-section restorations, mineral assemblages, and dominant deformation mechanisms in the East Fork fault system (Evans 1988, 1990a, in press), temperature in the fault zone likely ranged from 250°C (at the breach of the Precambrian rocks) to 150°C and saturation ranged from 0% to 70%. This further constrains the fluid/rock ratios such that $\mathbf{N_W}$ is ≈ 245 to 4130 and $\mathbf{N_V}$ is ≈ 647 to 10900 (Fig. 33a).

Fluid/rock weight ratios ($\mathbf{N_W}$) for the White Rock ultracataclasite zone ranged from ≈ 207 (T = 350°C, s = 0%) to ≈ 33,800 (T = 150°C, s = 90%). Fluid/rock volume ratios ($\mathbf{N_V}$) ranged from ≈ 569 (T = 350°C, s = 0%) to ≈ 93,000.(T = 150°C, s = 90%). Based on cross-section restorations (Mitra 1984), mineral assemblages (e.g., kaolinite and laumontite are not stable at temperatures above ≈ 300°C to 350°C (Montoya & Hemley 1975, Hemley *et al.* 1980), and dominant deformation mechanisms in the White Rock fault (e.g., cataclasis of feldspar and quartz), temperature in the fault zone likely ranged from 350°C (at the breach of the Precambrian rocks) to 250°C, and saturation likely ranged from 0% to 70%. This further constrains the fluid/rock ratios such that $\mathbf{N_W}$ is ≈ 207 to 2220 and $\mathbf{N_V}$ is ≈ 569 to 6120 (Fig. 33b)

LABORATORY PERMEABILITY TESTING

Steady-state permeability tests of 19 East Fork protolith, damaged zone, and gouge/cataclasite samples at ambient temperature and pressure yield permeability values from less than 10^{-20} m^2 to as high as $3x10^{-15}$ m^2 (Table 5). Laboratory permeability measurements are accurate to within ≈ 10%. Figure 8 illustrates the typical sampling technique, which maximized the delineation of permeability heterogeneity and anisotropy within the fault zone.

Results suggest that fault zone permeability is heterogeneous such that there is at least an order of magnitude difference in permeability from protolith (≈ 10^{-16} m^2) to the damaged zone (≈ 10^{-15} m^2), and two orders of magnitude difference between the damaged zone and the

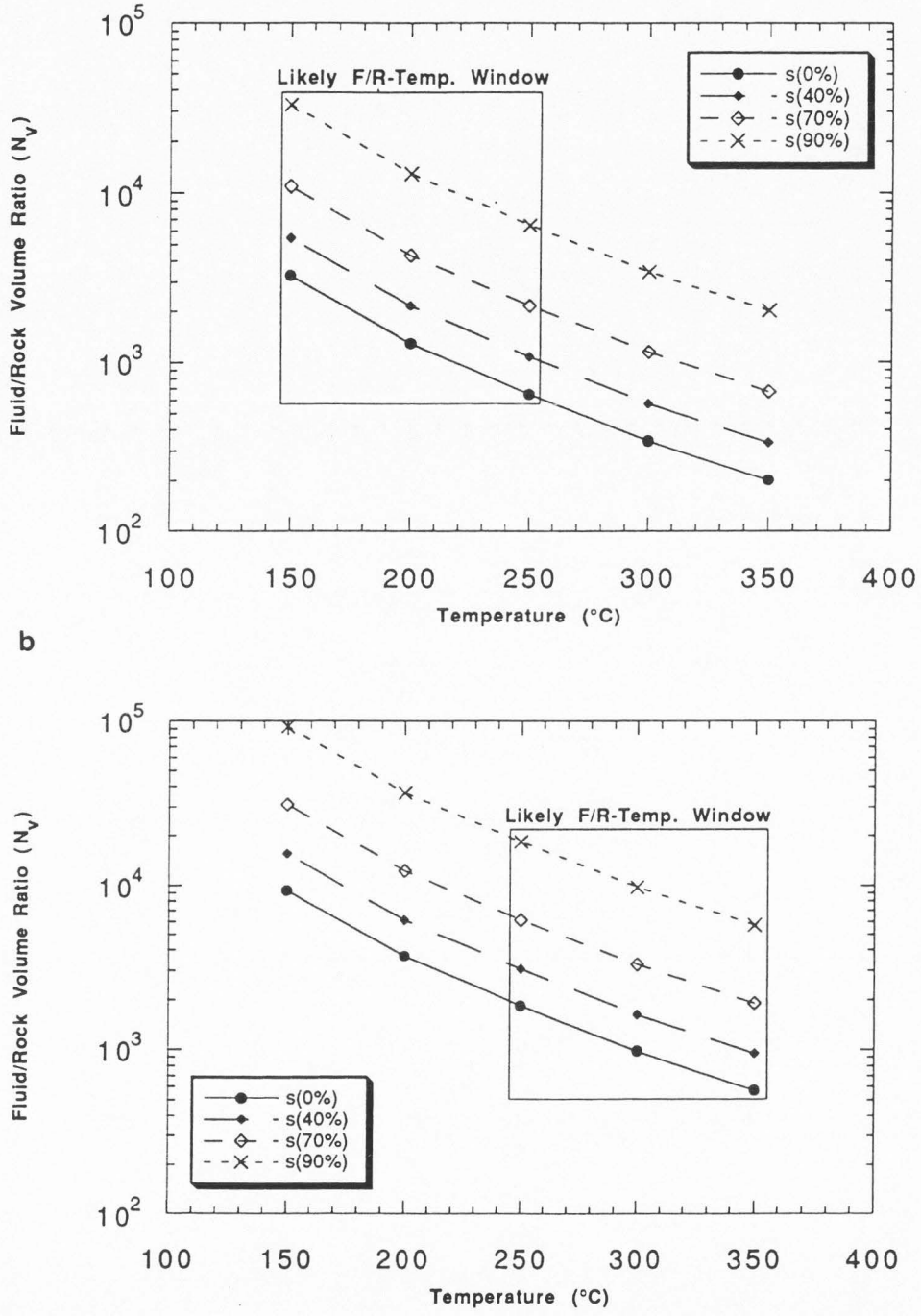

Fig. 33. Plot of inferred fault zone temperature versus fluid/rock volume ratios (from Table 4) for the East Fork fault (**a**) and the White Rock fault (**b**). Likely F/R-Temp Window represents the likely fluid/rock volume ratios that may have existed in the fault zone based on fault zone temperature constraints of 150°C to 250°C for the East Fork fault and 250°C to 350°C for the White Rock fault. Ratios for both faults range from $\approx 10^2$ to 10^4.

Table 5. Laboratory estimates of permeability. Samples with and asterisk (*) were reported by Forster & Evans (1991).

	Sample	∥ or ⊥	k_i (m^2)
Protolith	EF391-A	∥	9.8×10^{-17}
	EF391-B	∥	1.8×10^{-17}
	*EF-red	?	2.2×10^{-16}
	*EF-yellow	?	1.4×10^{-16}
Damaged Zone	EF291-B	∥	1.4×10^{-16}
	EF391-C	∥	1.9×10^{-16}
	EF591-A	∥	1.9×10^{-15}
	EF591-B	∥	1.6×10^{-15}
	*EFP1	∥	1.2×10^{-15}
	*EFP2	∥	3.0×10^{-15}
Gouge/Cataclasite Zone	EF291-V	⊥	1.3×10^{-17}
	EF591-V	⊥	$<10^{-20}$
	EF391-V	⊥	9.6×10^{-19}
	*EFV	⊥	2.0×10^{-17}
	EF291-A	∥	4.5×10^{-18}
	EF291-C	∥	8.0×10^{-18}
	EF591-C	∥	7.4×10^{-17}
	*EFH1	∥	6.0×10^{-17}
	*EFH2	∥	1.0×10^{-17}

gouge/cataclasite zone ($\approx <10^{-17}$ m^2) (Fig. 34). In addition, permeability was likely anisotropic with respect to the fault zone such that maximum permeability was parallel to the fault plane and minimum permeability was perpendicular. This is particularly evident in the gouge/cataclasite zone, where average permeability transverse to the fault plane is less than $8.5x10^{-18}$ m^2. This essentially focuses fluid flow in directions parallel to subparallel to the fault with little fault-perpendicular flow.

Thus, as suggested by field observations and fracture statistics, permeability is greatest in the damaged zone in directions parallel to subparallel to the fault plane. Because permeability of the damaged zone is approximately one order of magnitude higher than the protolith, the damaged zone likely acted as a conduit of least resistance for fluids. Permeability in the gouge/cataclasite zones is, for the most part, extremely low, especially in a fault perpendicular direction. Permeability of the gouge/cataclasite likely reflect fault conditions during the inter-seismic period, in that any dilatant fractures or pore permeability has been sealed or destroyed. However, transient permeability, during seismic rupture and ensuing fracture propagation and dilatancy, is likely greater.

These permeability tests are not *in situ*, nor were they conducted under pressures and temperatures typical during fault evolution. However, the relative permeability differences between intra-fault zones are likely representative of conditions during fault evolution. In addition, these values probably represent a lower limit to permeability, as they do not include the contribution of larger scale fractures.

Figure 35(a-c) shows three thin-section photonegatives and fracture trace maps of representative permeability-tested cores from the protolith, damaged zone, and gouge/cataclasite zone. It is easy to visualize the difference in permeability based on the degree of fracturing and interconnectivity. For example, the protolith consists primarily of intra-granular fractures with little completely throughgoing interconnectivity. Conversely, the damaged zone is made up of large, inter- and transgranular fractures that have a high degree of throughgoing

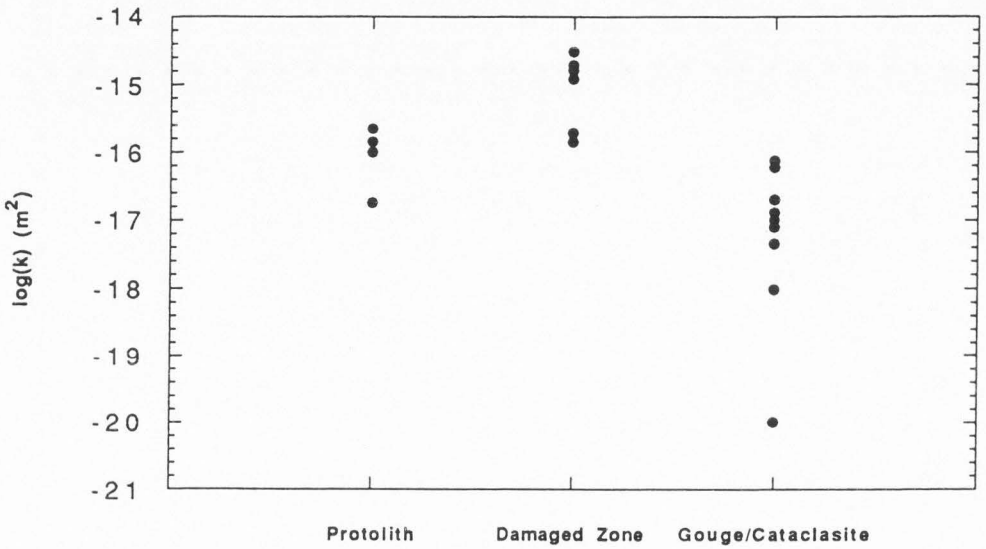

Fig. 34. Plot of laboratory-derived permeability versus location within the East Fork fault zone. Permeability values have an error of about ±10%.

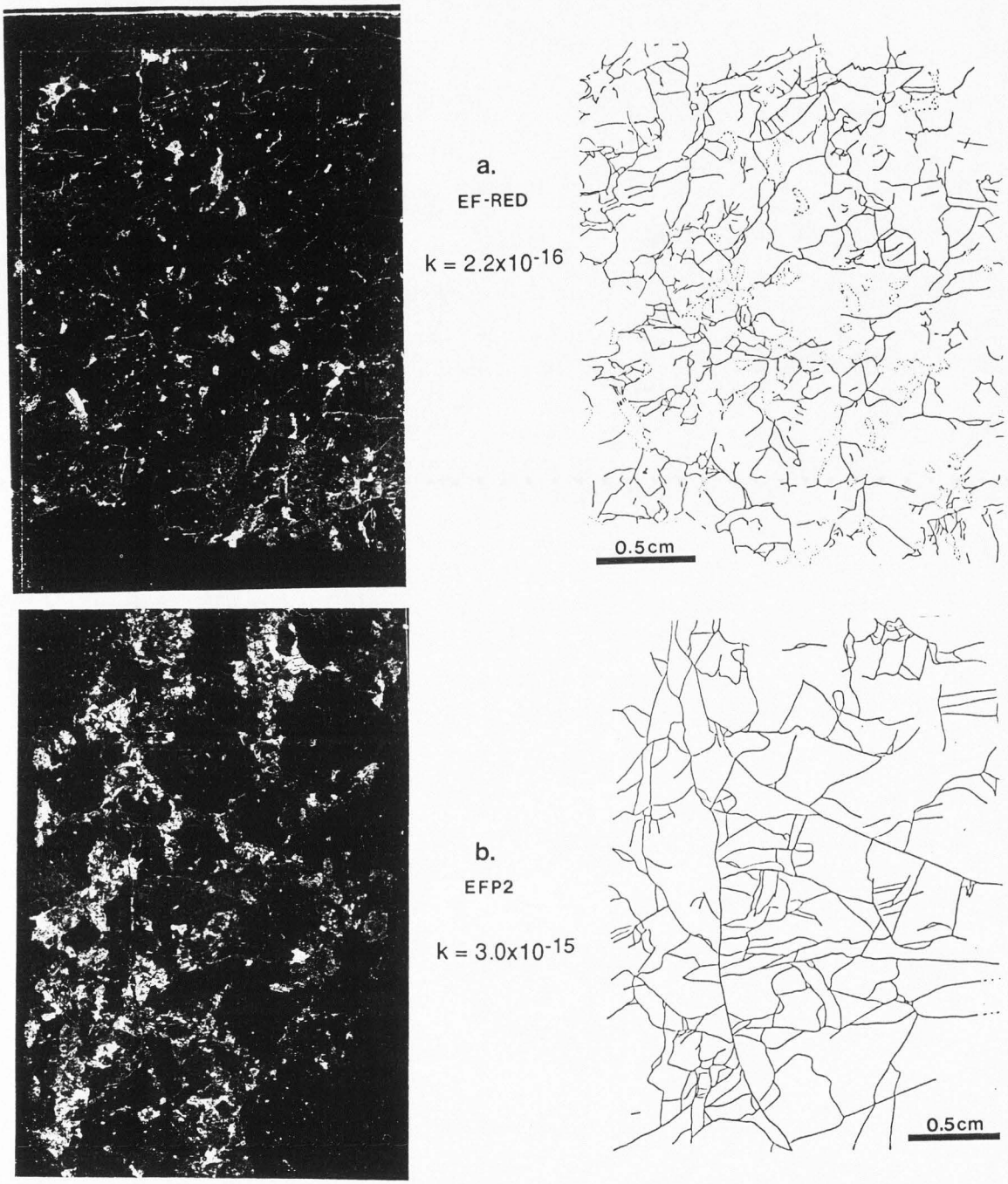

Fig. 35. Enlarged photonegatives of thin sections of permeability tested cores with resulting fracture trace maps. Flow direction for permeability test is along the long axis of photonegatives. Black grains are quartz, gray are feldspar, and white are mica, clay, and iron oxides. (**a**) Protolith sample EF-red. Fracture trace network is made up primarily of poorly connected intragranular fractures with no completely throughgoing intergranular fractures. (**b**) Damaged zone sample EFP2. Fracture trace network consist of many completely throughgoing fractures that, in turn, connect patches of intragranular fractures. (**c**) Gouge/cataclasite sample EFV. Approximately 50% of the map area is made up of very fine grained gouge/cataclasite that effectively acts as a fluid barrier for fluid flowing down the long axis of the photonegative.

Fig. 35. (continued).

c. EFV

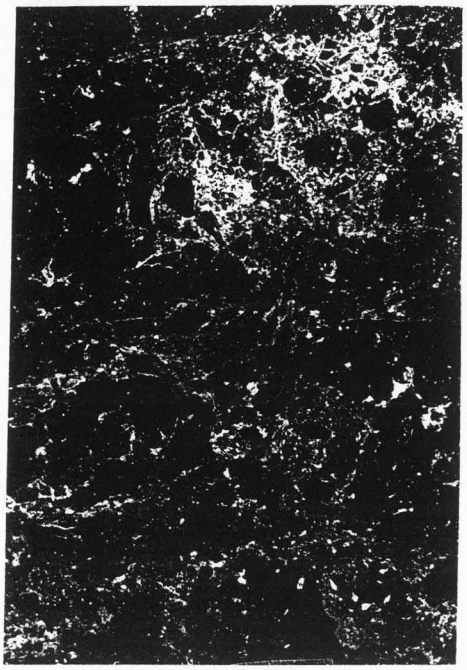

$k = 2.0 \times 10^{-17}$

interconnectivity. The gouge/cataclasite zone is made up of very fine-grained material that essentially acts as a flow barrier that chokes off any potential thoroughgoing permeability.

Future work will entail the analysis several East Fork core samples (5.2 cm diameter and 11.1 cm length) scheduled to be tested at the University of Utah, Department of Geology and Geophysics under successively greater confining pressures in order to evaluate how permeability tests at ambient pressure compares to permeability tests at *in situ* pressures.

DISCUSSION AND INTERPRETATION

Based on a synthesis of results discussed above, a spatial and temporal model that describes the deformation and permeability structure and the extent of fluid flow influences in the East Fork and White Rock fault zones is outlined below. Figure 36 is a cross-sectional view of a generalized fault illustrating the approximate structural levels and typical fault zone morphologies discussed in this section.

FAULT ZONE MORPHOLOGY AND EVOLUTION

A youthful fault is predominantly characterized by one or more primary slip surfaces bounded by randomly oriented, intragranular fractures. As the fault continues to evolve to an intermediate stage, a combination of fault-subparallel intragranular and intergranular fractures develops. The primary slip surfaces also widen as gouge and cataclasite form. A mature fault is internally zoned and consists of anastomozing arrays of interconnected, subparallel foliation, faults and fractures, with the cores of these fault zones containing variable stages (based on composition and grain size) of gouge and cataclasite. A typical traverse across a mature East Fork fault zone (structural level ≈ 6 to 8 km) (Fig. 36) would begin in unaltered protolith granite that grades into randomly fractured, slightly deformed protolith. The next stage nearer to the core is characterized by an increase in both micro- to outcrop, intra- and transgranular, interconnected, fault-subparallel fractures (damaged zone). The core is characterized by anastomozing zones of fine gouge and cataclasites, bounded by coarse, pinching and swelling pods of gouge, breccia, and protocataclasite. Because feldspars are volumetrically abundant, brittle deformation and comminution of feldspars were the dominant deformation mechanisms. Feldspars deformed by comminution from extension and shear fracture primarily along cleavage planes. Quartz deformed primarily by brittle fracture. During evolution, infiltrating fluids initiate the hydrolysis of feldspar and possibly the hydrolytic weakening of quartz. Insofar as silicate dissolution is controlled by surface area, the comminution of feldspar by cracking likely drove this

Fig. 36. Generalized cross section of a thrust fault illustrating the approximate structural levels and fault zone morphologies. The "shallow" zone structure is based on work by DuBois (1990) on the Ross Lakes reverse fault. This zone consists of brittle fractures and faults containing vein-fillings and shows little evidence of gouge and cataclasite. The shallow zone has no volume loss and is a locus of solute deposition (veins). The "intermediate" zone is based on characterization of the East Fork fault and the White Rock thrust near Roaring Fork Canyon. This zone has moderate volume loss and is also a locus of solute deposition (veins and cementation). The "deep" zone is based on characterization of the White Rock thrust near Flat Top Mountain. This zone has large volume loss in the core and is a locus of solute deposition in the damaged zone (veins).

Fig. 36. (continued)

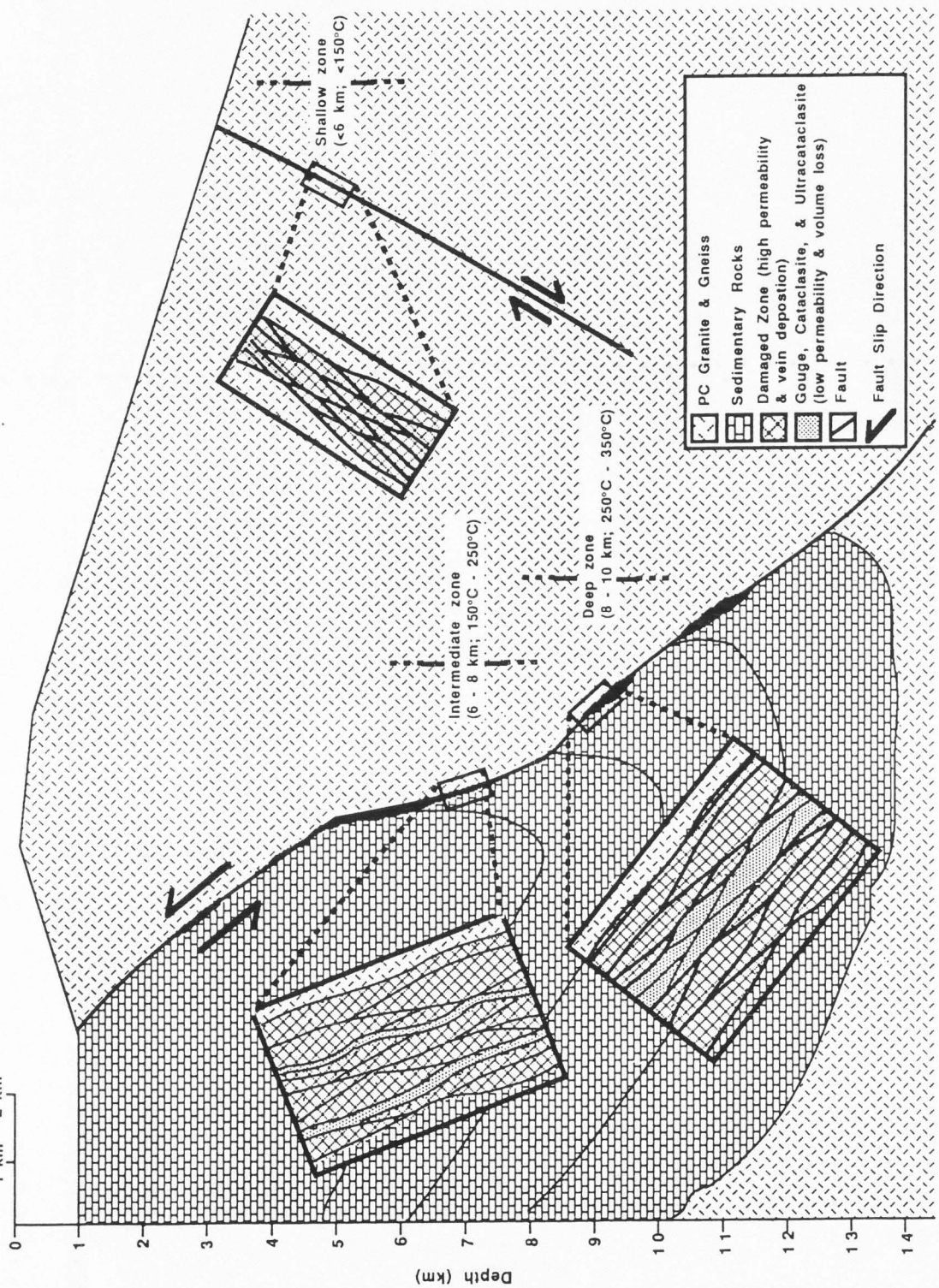

reaction forward. This resulted in moderate weakening of the rock and induced strain localization in the fault cores.

A typical traverse across a mature White Rock fault zone (structural level ≈ 10 km) (Fig. 36) would begin in unaltered protolith granite or gneiss that grades into randomly fractured slightly deformed protolith. The next stage nearer to the core consists of an increase in both intra- and transgranular, interconnected, fault-subparallel fracture densities primarily at outcrop scale (damaged zone). The core is characterized by an intensely deformed zone of foliated and nonfoliated ultracataclasites, bounded by anastomozing zones of intensely veined protocataclasites and cataclasites. This sequence of intrafault zones can also be extrapolated temporally such that the damaged zone is simply a precursor of the fault core.

Hence, the progression of structures from the edges to the middle of the fault zones provides a time sequence of development of the permeability and structures within the zone. Microfaults and fractures, and subsequent comminution of feldspar and quartz, increases towards the core of the White Rock fault. Increased grain surface areas due to comminution with higher temperatures and pressures (lithostatic and pore fluid) within the fault core probably drastically influenced active cataclastic deformation mechanisms by increasing the rate of the chemical breakdown of feldspar, quartz, and biotite. This altered the consequent mineral assemblages that resulted from deformation from a relatively "dry" assemblage of comminuted quartz and feldspar with minor clays such as the East Fork fault, to a "wet," strain-softened, assemblage of immobile components, phyllosilicates, clays, and zeolites with less quartz and feldspar. Within this relatively weak, strain-softened core, abundant microscopic veins and fractured porphyroclasts (fractured while in the fine, comminuted matrix) suggest that fluid pressures were, at least periodically, high (nearly lithostatic?). Comminution of feldspars also caused dilatantcy, allowing access of fluids. Fluid access along microcracks may have also promoted hydrolytic weakening in quartz, leading to further weakening. Thus, while cataclasis of feldspar by itself does not cause weakening, when followed by reaction-enhanced alteration

involving the production of phyllosilicates, together with hydrolytic weakening of quartz, an overall weakening of the rock apparently resulted. The actual deformation mechanism within the ultracataclasite is still a mystery, but structures and fabrics at the microscale suggest the dominant deformation mechanisms may be a combination of brittle and ductile, and are controlled and enhanced by the presence of fine-grained clays, zeolites, and other phyllosilicates that may act as a thermally pressurized, fluid-saturated lubricant somewhat analogous to grease between intact, cohesive slabs.

The fault zones typically grew in thickness with increasing time and deformation by gradualy fracturing into undeformed protolith wall rock. As deformation progressed, the fine-grained relatively weak core of the fault widened and accommodated progressively larger strain. Slip then became localized in these cores, particularly in the cataclasites for the East Fork and the ultracataclasites for the White Rock. At this stage, the thickening of the fault likely decreased in rate.

Faults at shallower structural levels, e.g., the White Rock fault near Roaring Fork Canyon and the East Fork fault, appear to be more diffuse, with displacement taken up over several sets of smaler faults, whereas deeper structural levels, e.g., the White Rock fault at Flat Top Mountan, appear to be concentrated into one zone, albeit wide, with the majority of displacement taken up within the cores.

FAULT ZONE PERMEABILITY STRUCTURE

Somewhat intuitively, the evolution of the permeability structure of the two fault zones follows the evolution of their physical morphology. Figure 37 illustrates the generalized physical and permeability structure of a typical fault zone. In early stages of fault evolution, permeability is enhanced by localized regions of increasing fracture density, aperture, and interconnectivity in the damaged zone (Fig. 37a-b). Permeability is likely similar both parallel and normal to the fault zone at this stage, with decreasing permeability with greater depth. At the intermediate stage,

Fig. 37. Schematic cross-sectional view of a generalized East Fork or White Rock fault zone illustrating the evolution of morphology and permeability structure, and the likely sources of infiltrating fluid. Evolution proceeds from young (**a**) to mature (**e**). Relative permeability is indicated in relative orders of magnitude (arrows) and is also indicated by generalized permeability ellipses. The permeability structure of the fault zone is based on field observation, fracture statistics, and laboratory-derived permeability measurements. Permeability arrows are directed up-structure and fault-perpendicular because : 1) permeability tests were conducted on samples parallel to fault slip direction and perpendicular to the fault plane; 2) it is assumed that fluids flow up the fault, based on this research and regional flow modeling (Forster & Evans 1991). Diagram not to scale.

Fig. 37. (continued)

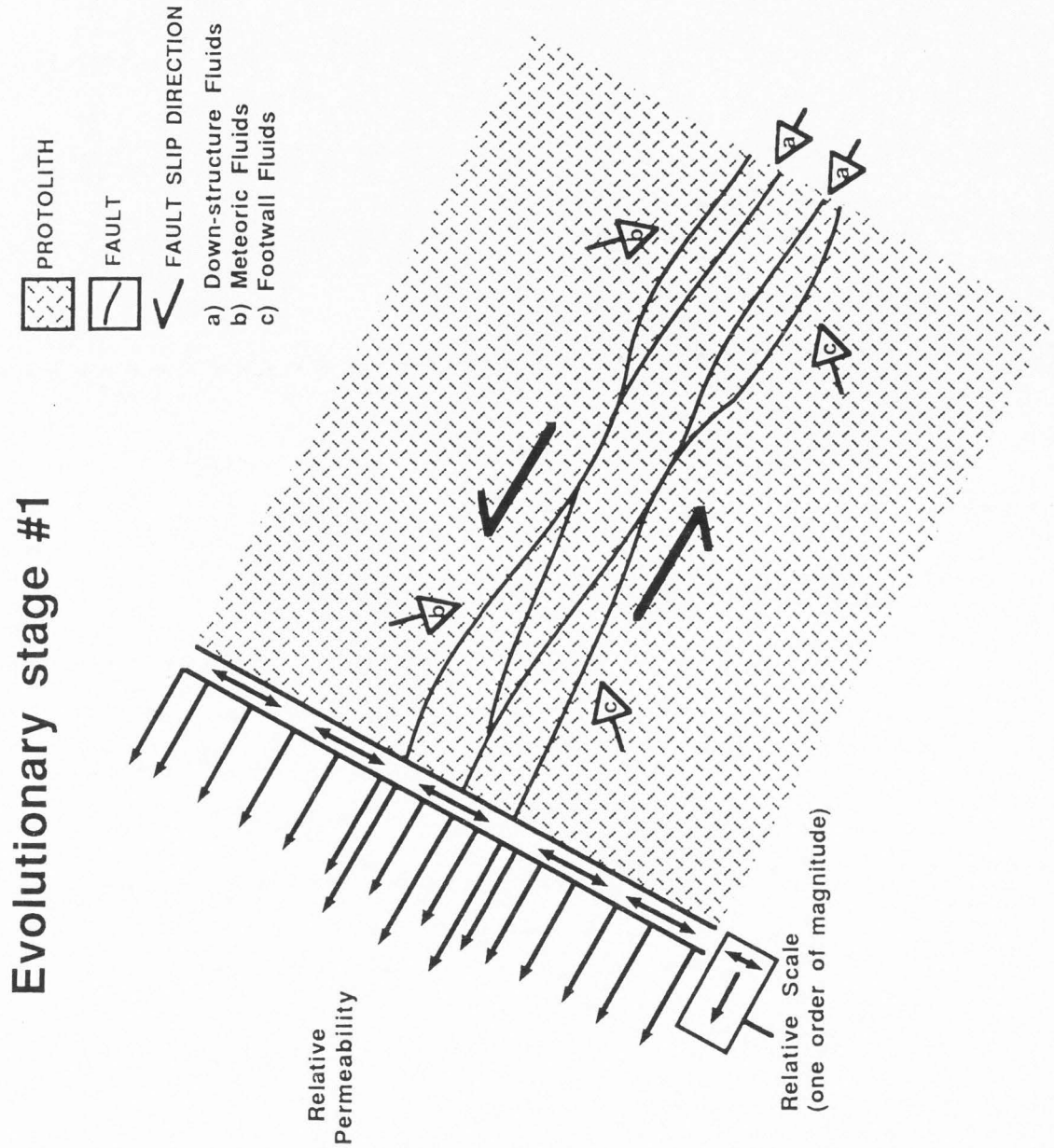

Fig. 37. (continued)

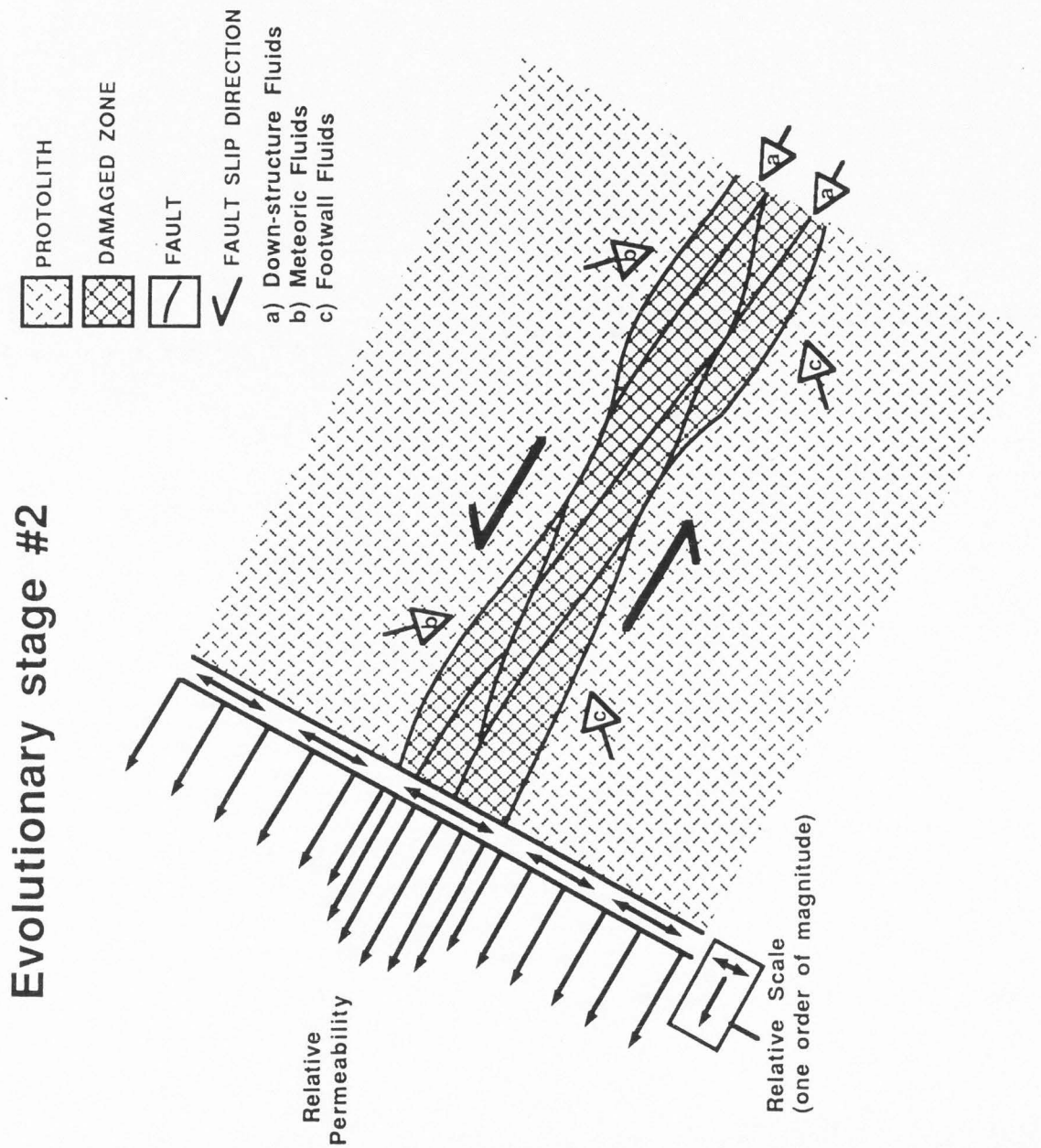

Fig. 37. (continued)

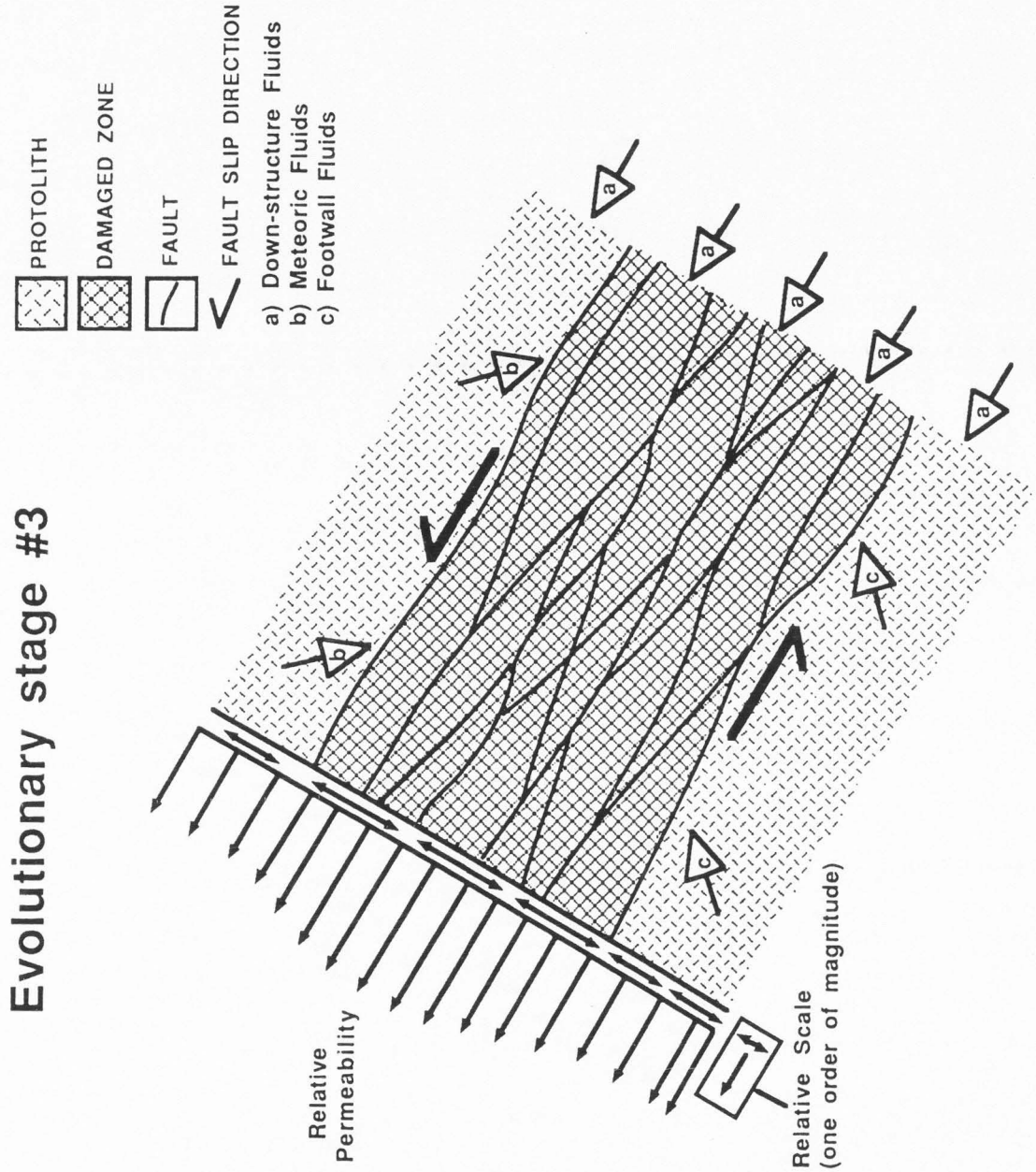

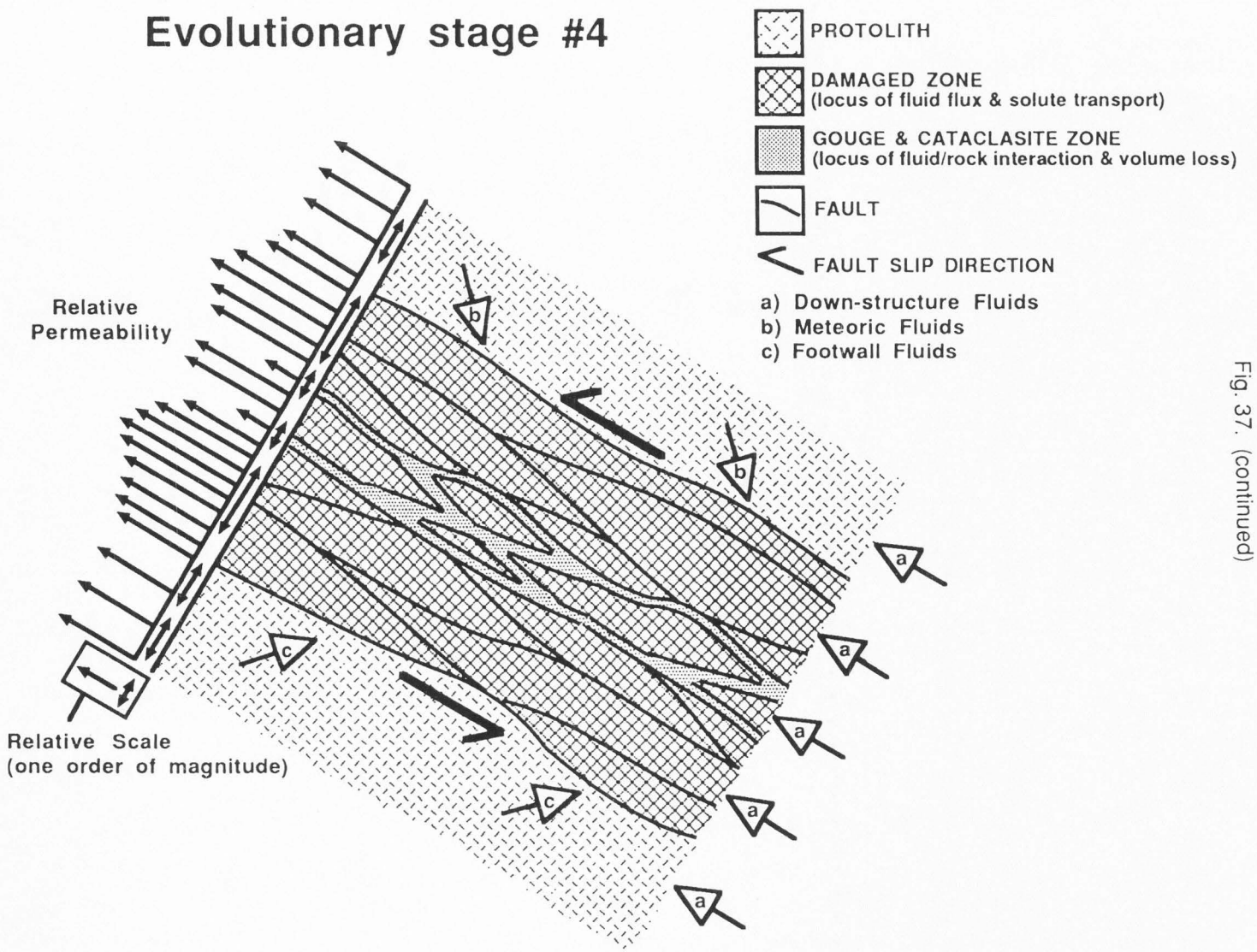

Fig. 37. (continued)

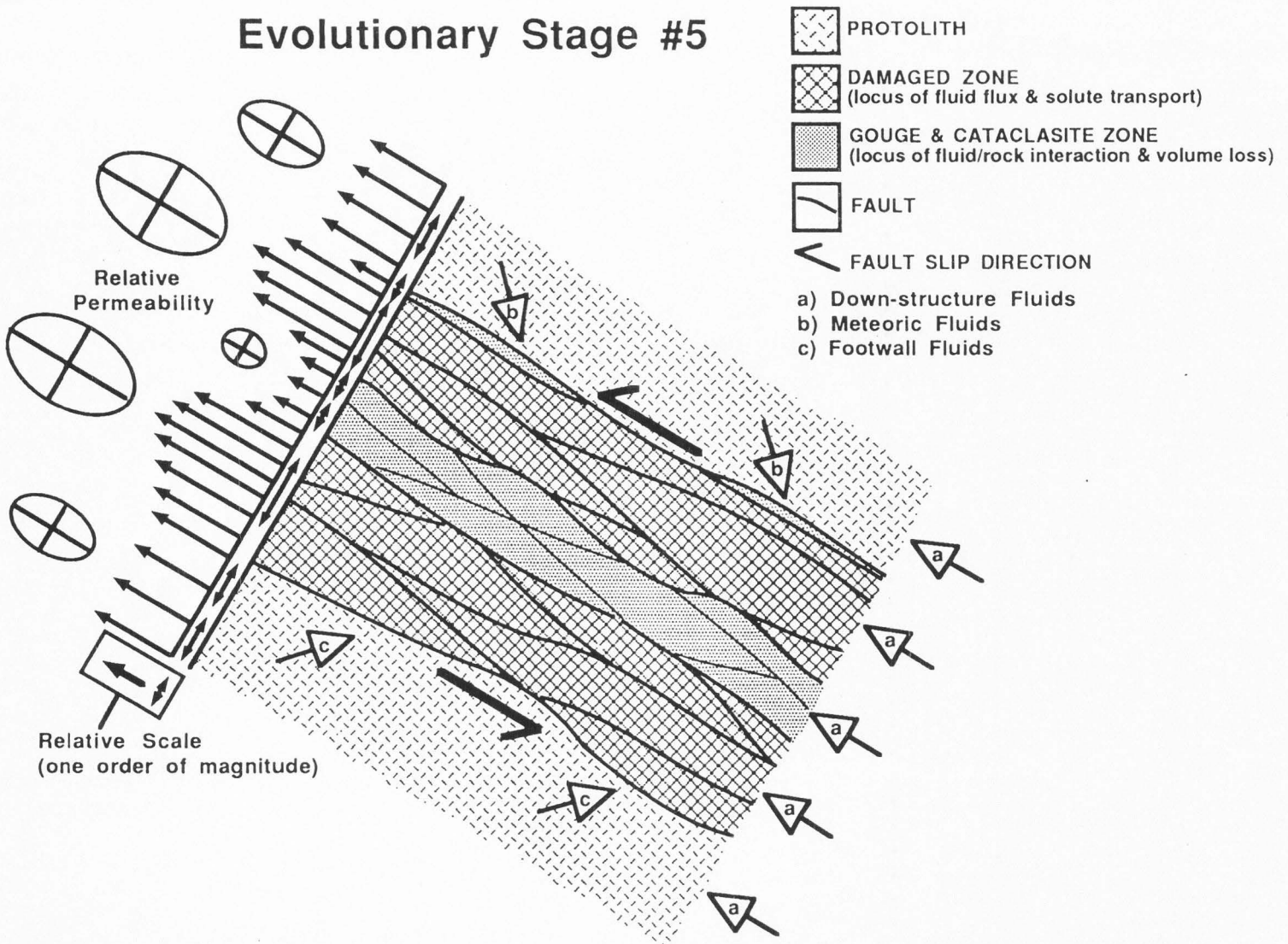

Fig. 37. (continued)

dense propagation of transgranular, fault-subparallel fractures in the damaged zone enhances permeability, particularly in directions subparallel to the fault zone (Fig. 37c). At the mature stage, intrafault-zone permeability likely decreases with the development of gouge and cataclasite zones and is heterogeneous such that there is at least an order of magnitude difference in permeability from protolith (intermediate) to the damaged zone (high), and two orders of magnitude difference from the damaged zone and gouge/cataclasite zone (low) (Fig. 37d-e). In addition, permeability was likely anisotropic with respect to the fault zone such that maximum permeability was parallel to the fault plane and minimum permeability was perpendicular (Fig. 37e). This essentially focuses fluid flow in the damaged zone in directions parallel or subparallel to the fault with little fault-perpendicular flow. Moreover, the fault core acted as a low permeability barrier and pressure seal, at least during compaction in the interseismic period.

Accordingly, permeability is greatest in the damaged zone in directions parallel or subparallel to the fault plane. Because permeability of the damaged zone is approximately one order of magnitude higher than the protolith, the fault likely acted as a conduit of reduced resistance for fluids. The gouge/cataclasite zones are, for the most part, nearly impermeable, especially in a fault perpendicular direction. Permeability of the gouge/cataclasite likely reflects fault conditions during the inter-seismic period, in that any dilatant fractures or pore permeability has been sealed or destroyed, consequently increasing the pore fluid pressure in the fault core. However, transient increases in permeability may occur during seismic rupture and ensuing fracture propagation and dilatantcy. Fluid/rock interaction is greatest in the core and permeability and solute transport is highest parallel to the fault and focused in the fracture-dense damaged zone. Open fractures and increased permeability are likely transient, being either closed, sealed with vein deposits, or healed with time until new fractures are formed during ensuing seismic slip.

In the East Fork fault, veining through fractures is pervasive at both the macroscopic and microscopic scale in the damaged zone, suggesting both high permeability and transportability, and moderate chemical reactivity through this zone. Conversely, the cataclasite zones are

characterized by a lack of veins at any scale, suggesting low permeability and transportability, though chemical interaction likely was high in this zone.

Within the White Rock core and damaged zone, numerous cross-cutting sets of fractures, faults, veins, and cataclastic foliations imply at least 11 syntectonic episodes of fluid assisted deformation and fluid flow. Macroscopic veining through large-aperture fractures is most dense in the damaged zone, suggesting high permeability and transport of material through this zone. Microscopic fracturing and veining is less dense in the damaged zone, suggesting that fluid flow was pervasive in the damaged zone only at the macroscopic scale. Conversely, the cataclasite zones show an approximately equal density of macroscopic and microscopic veins. Macroscopic veining in the ultracataclasite layers is not obvious; however, micro-scale faulted, folded, and sheared veins are numerous in the fine core, suggesting that the ultracataclasites were at least sporadically permeable.

FAULT ZONE WATER/ROCK INTERACTION

Fluids also likely influence fault zones differently with changing structural level. Deeper structural levels (White Rock thrust) have high enough pressures and temperatures to bolster cataclastic deformation by chemically softening and dissolving mobile elements such as silica and alkalies. If fluid circulation is great enough, this may create volume losses in deep (near the brittle-ductile transition) fault zones of up to 30-70%. Volumetric losses of this magnitude require enormous amounts of chemically active fluids, likely on the order of 10^2 to 10^4 volumes of reactive water per volume of rock. Essentially, the White Rock thrust core may have been analogous to a solution seam on a large scale along which large amounts of material have been removed. This lost rock volume may have been driven (by an upward pressure gradient during fault-valve action, (see Sibson 1992) in solution to higher structural levels where pressure and temperature conditions allow for the precipitation or crystallization of the silica. The abundant quartz veins and silica cementation in the East Fork area may have been derived, at least in part,

from saturated fluids migrating upward from deeper structural levels. Fluid flow at deep structural levels appears to have been focused in the core of the fault zone through microscopic fractures, and through large-aperture, macroscale fractures in the damaged zone. Comminution within the core of faults led to grain-size reduction and an increase in grain boundary area, which facilitated volume loss and fluid/rock reactivity.

Fluid flux and elevated fluid pressures in the core could be generated and maintained during the life of the White Rock thrust by a cycle of processes, including: 1) fracture formation in the core of the fault during a seismic event combined with instantaneous seismic pumping into these new fractures to recharge the fault core with fluid; 2) crystallization and precipitation of vein minerals in open fractures; 3) post-seismic self-sealing and compaction of fracture networks leading to considerable fluid expulsion (fault-valve action) and increased pore-fluid pressure in the core; and 4) inter-seismic sealing and compaction of fracture networks and core material leading to permeability reduction and an increase in pore-fluid pressure (Sibson 1990, Sleep & Blanpied 1992). The cycle then repeats during ensuing seismic events.

Intermediate structural levels (East Fork fault) are characterized by little or no volume loss (0-20%) due to the lack of fault-zone rock reactivity (and solubility) at lower pressures and temperatures, even though the zone has abundant quartz veins and cementation. Hence, the shallower the fault, the more fluid is required to dissolve and transport the rock. Because of this, fluid/rock volume ratios on the same magnitude as the White Rock thrust (10^2 to 10^4 for $\approx$ 64% volume loss) are required to remove only 20% of the fault rock volume. Fluid flow at higher structural levels appears to be more pervasive at both the micro- and macro-scale (fractures are open for a longer duration) and focused in the damaged zone. Though not great, the highest volume loss ($\approx$ 20%) was focused in the damaged zone because of the increase in circulation of fluids relative to the adjacent protolith and fine-grained core. Though fluids likely infiltrated and affected deformation in the core of the faults at shallow crustal levels, low volumetric losses relative to the protolith suggest that circulation and transfer of solutes were minimal and that

depleted elements such as silica may have been repurveyed in the core by penetrating fluids. That is, saturated fluids infiltrating the gouge/cataclasite zone likely became temporarily trapped. This facilitated both the dissolution of gouge/cataclasite material and the crystallization and precipitation of solutes from the permeating fluids.

Based on the large-scale leaching of silica from the fault zone (20% to 70%), fluids entering the fault zone were likely undersaturated with respect to silica throughout most of the life of the fault. This suggests that an influx of silica-poor water circulated into the fault zone. The sudden increase in temperature and pressure in the fault zone would tend to enhance silica solubility in the presence of silica-undersaturated fluids. Also, a fault zone, acting as a boundary for an inverse thermal gradient (from hotter basement rocks overriding cooler sedimentary rocks), could have increased the solubility of many of the mobile components within the fault (e.g., Sinha *et al.* 1986). Fluids could also have been derived from footwall sedimentary rocks, such that pressure from the overriding granite thrust sheet forced fluids into the fault zone. The contribution of metamorphic and upwelling hydrothermal fluids was likely minimal.

Based on calculated volume losses and fluid/rock volume ratios, the time, or in this case fluid flux, involved in creating the estimated volumetric losses by fluid transport can be roughly estimated. Assumptions made in this estimate for the East Fork and White Rock thrusts include: 1) the maximum and minimum life of the faults and ensuing fluid/rock interaction was ≈ 20 million years (Dickinson *et al.* 1988) and ≈ 1 million years (if fluid interaction was incremental), respectively; 2) temperatures and silica saturation in the fault zones ranged from 350°C to 250°C and 0% to 70% in the White Rock thrust and 250°C to 150°C and 0% to 70% in the East Fork thrust; 3) silica depletion was ≈ 50 g/100 g rock in the White Rock fault core and 18 g/100 g rock in the East Fork fault damaged zone, resulting in fluid/rock volume ratios of 10^2 to 10^4; and 4) comparable deformation and fluid/rock interaction occurred over a stretch of fault about one kilometer in length and 10 meters wide. In this case, water is channeled up a 1 km long, 10 m wide (cross-section view) by 1 m wide (map view) fault conduit (i.e., 10,000 m^3 of fault).

Essentially the calculation determines fluid flux (**q**), or the volume of fluid ($\mathbf{N_V}$ x 10,000 m^3 of rock) that must pass through a 10 m^2 fault conduit in a period of time (1 my to 20 my). For example, [10,000 m^3 (volume of affected fault) x 1000 ($\mathbf{N_V}$)]/[10 m^2 (conduit) x 20 my (maximum duration of deformation)] = $5x10^4$ m/my $\approx$ 10^{-9} ms^{-1}. Calculated fluid fluxes based on the above stated criteria range from 10^{-6} ms^{-1} to 10^{-9} ms^{-1} (Fig. 38). These calculated fluid flux values are similar to those calculated by Forster and Evans (1991), using a numerical flow model based on a thrust fault of similar character as the East Fork and White rock thrusts.

Both fault zones have similar distributions of fluid flux. Remember that fluid flux values are based on volumetric losses of silica from the faults. Thus, less fluid flux is required to remove large amounts of material from the "hotter" White Rock thrust, whereas more fluid flux is required to remove small amounts of material from the "cooler" East Fork fault. Large fluid fluxes likely did not occur continuously throughout the entire $\approx$ 20 my history of faulting, but rather were temporally incremental.

Fluid/rock volume ratios on the order of 10^2 to 10^4 may seem excessive. However, when extrapolated over the volume of affected fault (e.g., 10,000 m^3) over the life of the fault (e.g., 20 my), water/rock volumes become more conservative. For example, fluid/rock volume ratios between 100 and 10000 correspond to fluid/rock volume ratios over time of 0.005 L/m^3 of rock•yr and 0.50 L/m^3 of rock•yr, respectively.

a.

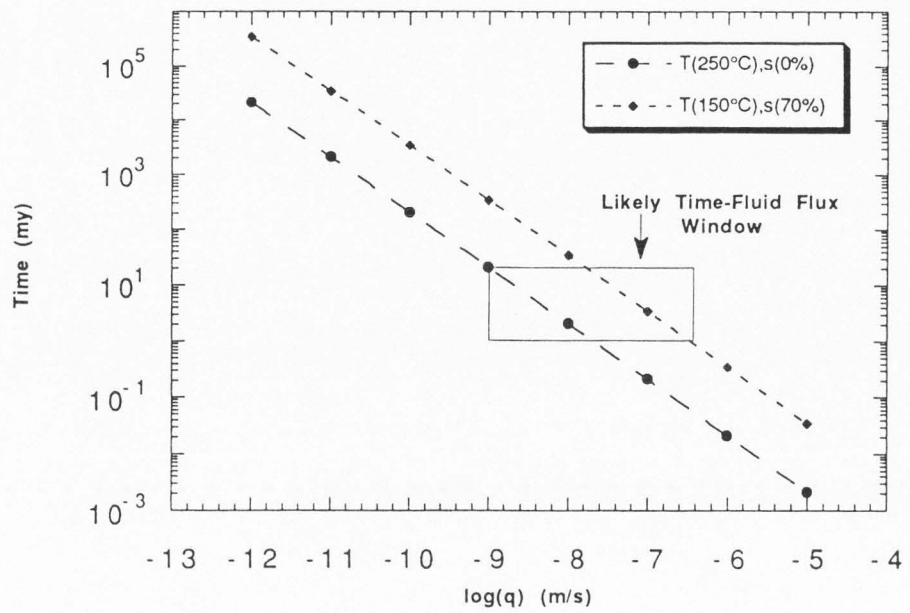

a.

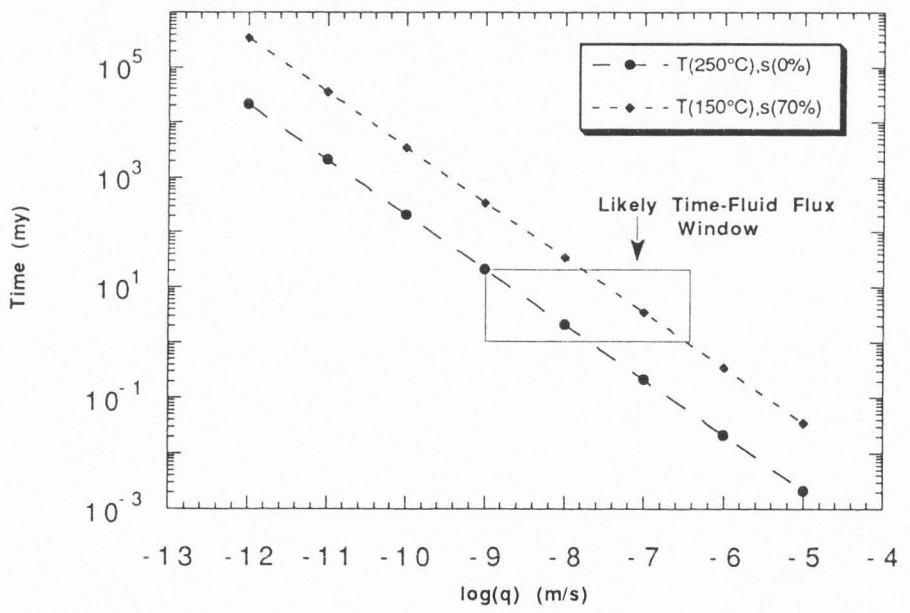

Fig. 38. Plot of fluid flux (**q**) versus time required to create the estimated volumetric losses within the East Fork fault (a) and the White Rock fault (b). Likely Time-Fluid Flux Window represents the likely fluid flux that may have existed in the fault zone based on the time constraint of between 20 my and 1 my, fluid saturation with respect to silica between 0% and 70%, and fault zone temperature constraints of 150°C to 250°C for the East Fork fault and 250°C to 350°C for the White Rock fault. Fluid fluxes in the fault zones may have ranged from 10^{-6} ms^{-1} to 10^{-9} ms^{-1} (probably closer to the lower end).

CONCLUDING REMARKS

This study integrates field, microstructure, fracture statistic, geochemistry, and laboratory permeability results of two exhumed thrust fault zones to develop a physical model that characterizes the temporal and spatial distribution of intra-fault structure, deformation, permeability, and fluid flow. Based on results derived from several different structural levels from the East Fork and White Rock faults (Fig 42), at least two zones of intra-fault structure, deformation, permeability, and fluid flow can be delineated. The first zone is at an "intermediate" level between ≈ 6 to 8 km structural depth (East Fork fault), and the second is at a "deep" level that forms at ≈ 8 to 10 km structural depth (White Rock fault).

Both zones are internally zoned, heterogeneous, and anisotropic with respect to physical and permeability structure, and can be separated into: 1) unaltered granitic protolith in which permeability is relatively intermediate, homogeneous, and isotropic; 2) fault-subparallel fractured, veined, and faulted damaged zone in which permeability is relatively high, heterogeneous with respect to local variations of fracture density and interconnectivity, and anisotropic with flow concentrated in open micro- and macroscopic fractures in directions subparallel to the fault; and 3) anastomosing zones of non-foliated to foliated gouge, cataclasite, and ultracataclasite in which strain is localized and permeability is relatively low, acting as a fluid flow barrier and pressure seal, especially for flow across the fault. This internal zoning also likely describes the temporal evolution of the fault zone from early to late stages. That is, the fault evolves from randomly fractured protolith to a fault-subparallel-fractured damaged zone to a damaged zone interspersed with pinching and swelling pods of gouge and cataclasite along the major slip surfaces. The internal structure, permeability, and evolution of these mature faults may represent the characteristics of active faults that possess similar tectonic regimes, protoliths, and structural levels.

The dominant deformation mechanisms at the intermediate zone were brittle fracture, comminution, and subsequent late stage hydrolysis of feldspar to clays. Veining through

fractures is pervasive at both the macroscopic and microscopic scale in the damaged zone, suggesting both high permeability, solute transport, and chemical reactivity of material through this zone. Conversely, the gouge and cataclasite zones are characterized by a lack of veins at any scale, suggesting low permeability and solute transport, albeit chemical reactivity of material likely was high in this zone. Although abundant syntectonic quartz veins within the intermediate zone suggest the circulation of large volumes of fluid, calculated volume loss was minimal in the damaged zone, with no calculated volume loss in the gouge/cataclasite zones. The excess vein-fill in the damaged zone and the unlikely possibility that large quantities of silica could have migrated from up-structure or from adjacent country rock suggest that silica-saturated fluids migrated from deeper parts of the fault. Estimated volume loss in the damaged zone requires fluid/rock volume ratios on the order of 10^2 to 10^4, confirming the conclusion that large quantities of fluids passed through this zone.

Deep zone deformation is characterized by brittle fracturing, faulting, and vein-filling in the damaged zone and extreme, fluid-assisted cataclasis in the fault core, which have led to large-scale comminution and dissolution of feldspar, quartz, and mica to produce: 1) clays, zeolite, and phyllosilicates; 2) concomitant enrichments in immobile components such as Ti, Mg, Mn, Fe, Zr, Y, and P; and 3) loss of silica and alkalies to an infiltrating fluid resulting in large volume losses of about 30% to 80% and fluid/rock volume ratios between 10^3 to 10^4. Progressive grain-size reduction and fluid-enhanced chemical breakdown of quartz, feldspar, and mica within the fault zone initiated strain softening and localization as cataclasite and ultracataclasite developed. Deformation mechanisms in the fault zone may have been a combination of brittle and ductile, supplemented with high pore pressure and low effective stress. Deformation mechanisms in the fault core may have been less frictional and strongly influenced by the presence of fine-grained clays, zeolites, and other phyllosilicates that may have acted as a thermally pressurized, fluid-saturated lubricant. Macroscopic veins in large-aperture fractures are densest in the damaged zone, suggesting high permeability and transport of material through this zone. Microscopic

veining is less dense in the damaged zone, suggesting that fluid flow was pervasive in the damaged zone only at the macroscopic scale. Conversely, the cataclasite zones show an approximately equal density of macroscopic and microscopic veins. Macroscopic veining in the ultracataclasite layers is not obvious; however, micro-scale faulted, folded, sheared, and undeformed veins are numerous in the fine-grained core, suggesting that fluid flow was episodically high.

The impact of fluid-rock interaction in ductily deformed faults and shear zones (>10 km depth) has been widely documented (Mitra & Frost 1981, Engelder 1984, Mitra 1984, Grant 1986, Kerrich 1986, O'Hara 1988, Sinha *et al.* 1988, Losh 1989, O'Hara & Blackburn 1989, Glazner & Bartley 1991). However, documentation on the importance of fluids in semi-brittle to brittle fault zones (<10 km depth) is uncommon and often even minimizes the role of fluid-rock interaction. This study and other work (e.g., Forster & Evans 1991), on the other hand, implies that semi-brittle to brittle fault zones are greatly affected by fluids. These fault zones serve as fluid conduits that facilitate fluid interaction on fault zone deformation mechanisms and evolution, volume loss due to fluid transport, and variations in permeability due to cyclical fracture opening and vein filling. Because these faults are shallower and cooler than deeper, ductile faults, a tremendous quantity of chemically active fluids must have penetrated through high permeability fault zones and transported large volumes of mobile fault material out of the local system. This explains the unusually large fluid/rock ratios of $\approx 10^2$ to 10^4 computed for the deep and intermediate levels.

Fluids in the two fault zones likely originated from: 1) meteoric water entering from the fractured crystalline hanging wall; 2) connate fluids derived from footwall sedimentary rocks; and 3) fluids migrating upwards from deeper structural levels along the same fault zone. Because the damaged zones of the deep zone are pervasively vein-filled with Ca-rich laumontite, sedimentary rock connate fluids of the footwall, at least in part, may be responsible for the zeolite veins. If this is the case, fluids must have traversed the low permeability fault core in order to deposit zeolites

in the hanging wall-damaged zone, which implies that the fault core permeability was, at least periodically, high. Again, this suggests that the fault zones acted as a fluid flow conduit-barrier system. This conduit-barrier system was likely generated as a result of seismic cycling, which spatially and temporally created and destroyed fracture permeability both in the core and in the damaged zone (Sibson 1990, Sleep & Blanpied 1992). A generalized cycle may have included: 1) dilatantcy and subparallel fracture formation in the damaged zone and core of the fault during a seismic event combined with instantaneous seismic pumping into these new fractures to recharge the fault core with fluid. At this stage the fault zone acts as a fluid flow conduit in that permeability is high in both the damaged zone and the fault core; 2) crystallization and precipitation of vein minerals in open fractures with time gradually decrease the effective permeability; 3) post-seismic self-sealing and compaction of fracture networks initially in the core lead to considerable fluid expulsion (fault-valve action) into and along the damaged zone and increase pore pressure in the core. At this stage the fault acts as a fluid flow conduit-barrier in that fluid flow is concentrated along the fault in the damaged zone but is inhibited across the fault by the low-permeability fault core; and 4) inter-seismic sealing and compaction of fracture networks and core material lead to an overall permeability reduction in the fault zone and an increase in pore pressure in the fault core. The cycle then repeats during ensuing seismic events.

Fluid flux and fluid/rock volume ratios over time involved in creating the computed volume loss by fluid transport were estimated to range from $\approx 10^{-6}$ ms^{-1} to 10^{-9} ms^{-1} and 0.005 L/m^3 rock•yr to 0.50 L/m^3 rock•yr, respectively, for both the intermediate and deep zones. These values indicate that faults act as conduits for fluid flow, essentially focusing fluid flow on a regional scale. Because these values are based on volume loss in the ultracataclasites in the deep zone, permeability and fluid flow were likely episodically high, which is contrary to the low-permeability, fine-grained nature of the ultracataclasite. This suggests that periodic, tectonically driven fluid flux, in conjunction with continuous, topographically driven fluid flux, operated in at

least the deep zone fault cores. Thus, large fluid fluxes did not occur continuously throughout the entire ≈ 20 million year history of faulting, but rather fluxes were temporally incremental within the seismic cycle. Upward pressure gradients, combined with transient tectonic driving forces, pushed saturated fluids to shallower structural levels in the intermediate zone, where the fluids eventually deposited solutes as vein-fill in the high permeability damaged zone or as cementation in the low permeability gouge and cataclasite zones.

Faults possessing the characteristics discussed here act as zones of large volume loss and major conduits for fluid flow and solute transport. On a regional scale, like the local scale, mature faults serve as barriers to fluid flow across faults, but facilitate fluid flow parallel to the fault in the damaged zone. Even during seismic rupture in the fault cores, vein geometry suggests that fluids were pumped into the fault core and expelled up-structure in a fault parallel direction instead of across the fault. These results have an impact not only for understanding the role of fault evolution and fluid flow, but also for understanding how these fluid flow and deformation characteristics affect the development of ore deposits and hydrocarbon migration and entrapment. For example, ore deposits would tend to be found in vein-fill in the damaged zone of the intermediate zone and disseminated in the gouge and cataclasite of the intermediate zone. On the other hand, cataclasite and ultracataclasite of a deep zone may contain an abundance of immobile ore deposits, while the damaged zone of the deep zone may contain ore deposits. Also, a mature fault, with accompanying low permeability units, can act as a hydrocarbon reservoir seal above footwall reservoir rocks. However, if the fault is still seismically active, the fault/seal can potentially rupture and leak hydrocarbons during seismic events, creating secondary hydrocarbon migration up-structure along the fault. This could seriously reduce the reservior hydrocarbon potential.

In an attempt to more fully characterize the role of fluid flow in fractures, fractal analyses provided several interesting results and led to the development of new fracture characterization techniques. Box counting fractal analysis of fault zone fractures showed that fracture spatial and

density distribution is scale-invariant at the separate scales of outcrop, hand-sample, and thin-section, but self-affine from outcrop to thin-section scale. That is, fractures at the hand-sample scale have a smaller fractal dimension than fractures at the thin-section and outcrop scale. This poses serious implications, especially if only the hand-sample scale is relied upon to extrapolate the distribution of fractures at the thin-section and outcrop scales. For example, the spatial distribution of fractures from a well core may not be representative of the fracture distribution at all scales. The box counting fractal methods depict the "filledness" or spatial distribution of fractures. The Cantor dust fractal method developed for this research depicts the spatial, clustering, and density distribution of fractures with respect to orientation. Preliminary results suggest a possible correlation between the results of the Cantor dust fractal method and two-dimensional fracture permeability, assuming a constant aperture. If this is true, the Cantor dust method may provide an initial quick and robust way to characterize two-dimensional fracture permeability. A practical use for this fractal data may be as another statistical parameter to input into a flow model or synthetic fracture network generator. This may provide another test between synthetic fracture models and real fracture data.

Since the results and interpretations discussed here are based on only a few faults, further research on these and other fault zones, as well as the implementation of other techniques, is required to better characterize fluid flow in the shallow crust. Additional geochemical studies, including scanning electron microscopy, isotope studies, and fluid inclusion studies, will shed further light and provide additional constraints on the internal structure of the fault cores, volume loss, fluid/rock ratios, syntectonic pressure and temperature, and fluid sources. Laboratory permeability tests at elevated pressures will provide fault rock permeability values that may more resemble the conditions present during fault evolution. Ideally, microstructural, geochemical, and permeability tests should be done *in situ*, on tectonically active faults. This would require very expensive deep-drilling projects. Such a program may be in the offing for the San Andreas Fault. Both local and regional scale fluid flow

modeling incorporating the results of this research are needed to further synthesize fluid flow in fractures and faults with respect to fault zone character, thermal conditions, pressure conditions, and stress regime. Of course, presently collected field characterization and fracture data never seem to be sufficient, and additional data will always help to substantiate, or negate, the findings to date. In addition, more fault zones, at a varying of structural level, protolith, and tectonic setting, should be similarly characterized to expand the knowledge of fault zone fluid flow.

The primary conclusions of this research are: 1) Fault zones can be separated into sub-zones of protolith, damaged zone, and gouge/cataclasite, based on physical morphology and permeability structure. At deep structural levels, gouge/cataclasite zones are more evolved (thicker with advanced grain size reduction) due to strain localization, higher pressure and temperature, and fluid/rock interaction; 2) Deformation mechanisms evolved from primarily brittle fracturing and faulting in the damaged zone to extreme, fluid-enhanced chemical breakdown and cataclasis, which localized strain in the fault core. Deformation in the deep-level-fault core may be a combination of frictional and quasi-plastic mechanisms, and is largely controlled by extremely fine-grained clays, zeolites, and other phyllosilicates that may have acted as a thermally pressurized, fluid-saturated lubricant; 3) Permeability in fault zones was temporally heterogeneous and anisotropic (k of damaged zone>protolith>gouge/cataclasite, k along fault>k across fault); 4) Volume loss was concentrated in the fault cores and was negligible at intermediate structural levels and high at deep structural levels in the semi-brittle to brittle regime; 5) Fluid flow and solute transport were concentrated upwards and subparallel to the fault in the damaged zone; 6) Faults at both the local and regional scale acted as fluid flow conduit/barrier systems depending upon the evolutionary stage and interval in the seismic cycle; 7) Fluid/rock volume ratios, fluid flux, and fluid/rock volume ratios over time ranged from $\approx 10^2$ to 10^4, 10^{-6} m/s to 10^{-9} m/s, and 0.005 L/m^3 rock•yr to 0.50 L/m^3 rock•yr, respectively, suggesting that enormous quantities of fluids passed through the fault zones; 8) Box counting fractal analyses of fault zone fractures showed that fracture spatial and density distribution are scale-invariant at

the separate scales of outcrop, hand-sample, and thin-section, but self-affine from outcrop to thin-section scale; 9) Linear fractal analysis depicts clustering and density distribution as a function of orientation, and may be a quick, robust method of estimating two-dimensional fracture permeability; 10) Fractal analysis of fractures is not a comprehensive statistical method, but can be used as another supplemental statistical parameter.

REFERENCES

Barnes, H. L. 1979. *Geochemistry of Hydrothermal Ore Deposits*. John Wiley & Sons, 465-470.

Barton, C. C. & Hsieh, P. A. 1989. Physical and hydrologic-flow properties of fractures. Field trip guidebook T385: 28th Int. Geol. Cong. Guidebooks, Amer. Geop. Un., 36.

Barton,C.C., LaPointe P. R. & Malinverno, A. 1991. Fractals and their use in earth science. Unpublished notes, Geol. Soc. Am. short course.

Barton, C. C. & Larsen, E. 1985. Fractal geometry of two-dimensional fracture networks at Yucca Mountain, southwest Nevada. In: Fundamentals of rock joints (edited by Stephannson, O.). *Proceedings of the International Symposium of Fundamentals of Rock Joints, Bjorkliden, Lapland, Sweden, Centek Publishers, Lulea Sweden*, 74-84.

Barton, C. C., Larsen, E., Page, W. R. & Howard, T. M. 1987. Characterizing fractured rock for fluid flow, geomechanical, and paleostress modeling: Methods and preliminary results from Yucca Mountain, Nevada. *U.S.G.S. Unpublished Report.*

Barton, C. A. & Zoback, M. D. 1992. Self-similar distribution and properties of macroscopic fractures at depth in crystalline rock in the Cajon Pass scientific drill hole. *J. of Geophys. Res.* **97**, 5181-5200.

Brace, W. F. 1984. Permeability of crystalline rocks: New in situ measurements. *J. Geophys. Res.* **89**, 4327-4330.

Brantley, S. L., Evans, B., Hickman, S. H., & Crerar, D. A. 1990. Healing of microcracks in quartz: Implications for fluid flow. *Geology* **18**, 136-139.

Brown, W. G. 1988. Deformational style of Laramide uplifts in the Wyoming foreland. In: Interaction of the Rocky Mountain foreland and the Cordilleran thrust belt (edited by Perry, W. J. & Schmidt, C. J.). *Geol. Soc. Amer. special paper 171*, 1-25.

Bruhn, R. L. & Yonkee, W. A. 1988. Fracture networks in fault zones. *EOS, Trans. of Amer. Geophys. Un.* **69**, 1172.

Bruhn, R. L., Yonkee, W. A. & Parry, W. T. 1990. Structural and fluid-chemical properties of seismogenic normal faults. *Tectonophysics* **175**, 139-157.

Cann, J. R. 1970. Rb, Sr, Y, Zr and Nb in some ocean floor basaltic rocks. *Earth Planet. Sci. lett.* **10**, 7-11.

Chester, F. M. & Logan, J. M. 1986. Implications for mechanical properties of brittle faults from observations of the Punchbowl fault zone, California. *Pageoph.* **124**, 80-106.

Chester, F. M., Evans, J. P. & Biegel, R. L. 1991. Internal structure and weakening mechanisms of large-displacement faults of the San Andreas system. *Geol. Soc. Amer. Abst. w/ Prog.* **23**, 103.

Chester, F. M., Evans, J. P. & Biegel, R. L. 1993. Internal structure and weakening mechanisms of the San Andreas Fault. *J. of Geophys. Res.* **98**, 771-786.

Chiles, J. P. 1988. Fractal and geostatistical methods for modeling of a fracture network. *Mathematical Geology* **20**, 631-654.

Clauser, C. 1992. Permeability of crystalline rocks. *GSA Today*, **1**, 233-237.

Compton, R. R. 1985. *Geology in the Field.* John Wiley & Sons, New York.

Correns, C. W. 1978. Titanium: behavior in metamorphic reactions. In: *Handbook of Geochemistry* (edited by Wedepohl, K. H.). Springer, Berlin, 22H.

Davy, P., Sornette, A. & Sornette, D. 1992. Experimental discovery of scaling laws relating fractal dimensions and the length distribution exponent of fault systems. *Goephys. Res. Lett.* **19**, 361-363.

Dickinson, W. R., Klute, M. A., Hayes, M. J., Janecke, S. U., Lundin, E. R., McKittrick, M. A. & Olivares, M. D. 1988. Paleogeographic and paleotectonic setting of Laramide sedimentary basins in the central Rocky Mountain region. *Geol. Soc. Amer. Bull.* **100**, 1023-1039.

Dostal, J., Strong, D. F. & Jamieson, R. A. 1980. Trace element mobility in the mylonite zone within the ophiolite aureole, St. Anthony complex, Newfoundland. *Earth & Plan. Sci. Lett* **49**, 188-192.

DuBois, M. A. 1990. Laramide deformation in Precambrian granitic rocks, northeastern Wind River Range, Wyoming. *Unpublished master's thesis, Utah State University, Logan, Utah* 204.

Engelder, T. 1984. The role of pore water circulation during the deformation of Foreland fold and thrust belts. *J. Geophys. Res.*, **89**, 4319-4325.

Evans, J. P. 1987. Geometry, mechanisms, and mechanics of deformation in a Laramide thrust sheet. *Ph.D. dissertation, Texas A&M Univ., College Station.* 217.

Evans, J. P. 1988. Deformation mechanisms in granitic rocks at shallow crustal levels. *J. Struct. Geol.* **10**, 437-443.

Evans, J. P. 1990a. Textures, deformation mechanisms, and the role of fluids in the cataclastic deformation of granitic rocks. In: Deformation mechanisms, rheology and tectonics (edited by Knipe, R. J. & Rutter, E. H.). *Geol. Soc. Amer. Special Publ.* **54**, 29-39.

Evans, J. P. 1990b. Thickness--displacement relationships for fault zones. *J. Struct. Geol.* **12**, 1061-1065.

Evans, J. P. in press. Deformation mechanisms and kinematics of a crystalline thrust sheet: the Washakie thrust system, Wyoming. In: Basement deformation in Rocky Mountain foreland structures (edited by Schmidt, C. J., Chase, R., & Erslev, E. A.). *Geol. Soc. Amer. special paper*, 280.

Faure, G. 1991. *Principles and Applications of Inorganic Geochemistry.* Macmillan Publishing Company, New York.

Feder, J. 1988. *Fractals.* Plenum Press, New York.

Floyd, P. A. & Winchester, J. A. 1983. Element mobility associated with meta-shear zones within the Ben Hope amphibolite suite, Scotland. *Chemical Geology* **39**, 1-15.

Forster, C. B. & Evans, J. P. 1991. Hydrogeology of thrust faults and crystalline thrust sheets: Results of combined field and modeling studies. *Geophys. Res. Lett.* **18**, 979-982.

Fournier, R. O. & Potter, R. W. 1982. An equation correlating the solubility of quartz in water from 25°C to 900°C at pressures up to 10,000 bars. *Geochim. Cosmochim. Acta* **46**, 1969-1973.

Garrels, R. M. & Christ, C. L. 1965. *Solutions, Mineral, and Equilibria.* Freeman, Cooper & Company, San Francisco.

Glazner, A. F. & Bartley, J. M. 1991. Volume loss, fluid flow and state of strain in extensional mylonites from the central Mojave Desert, California. *J. Struct. Geol.* **13**, 587-594.

Goddard, J. V. & Evans, J. P. 1991. Fractal and statistical characterization of fractured rocks and thin-section and hand-sample scales. *Geol. Soc. Amer. Abst. with Prog.* **23**, 496.

Grant, J. A. 1986. The isocon diagram-A simple solution to Gresens' equation for metasomatic alteration. *Economic Geology* **81**, 1976-1982.

Gresens, R. L. 1967. Composition-volume relationships of metasomatism. *Chemical Geology* **2**, 47-65.

Hanson, G. N. 1980. Rare earth elements in petrogenetic studies of igneous systems. *Ann. Rev. Earth Planet. Sci.* **8**, 371-406.

Hanson, R. B. 1992. Effects of fluid production on fluid flow during regional and contact metamorphism. *J. Metamorphic Geology*, **10**, 87-97.

Harris, C., Franssen, R. & Loosveld, R. 1991. Fractal analysis of fractures in rocks: the Cantor's Dust method -- comment. *Tectonophysics* **198**, 107-111.

Hemley, J. J., Montoya, J. W., Marinenko, J. W. & Luce, R. W. 1980. Equilibria in the system Al_2O_3--SiO_2--H_2O and some general implications for alteration/mineralization processes. *Econ. Geol.* **75**, 210-228.

Herrmann, A. G. 1978. Yttrium: abundance in natural waters. In: *Handbook of Geochemistry* (edited by Wedepohl, K. H.). Springer, Berlin, 14C.

Hickman, S. H. 1991. Stress in the lithosphere and the strength of active faults. *U.S. Nat. Rep. to Internat. Un. of Geodesy and Geophys. 1987-1990, Reviews of Geophys., Suppl.*, 759-775.

Howard, J. H. & Nolen-Hoeksema, R. C. 1990. Description of natural fracture systems for quantitative use in petroleum geology. *Amer. Assoc. Petro. Geol. Bull.* **74**, 151-162.

Hull, J. 1988. Thickness--displacement relationships for deformation zones. *J. Struct. Geol.* **10**, 431-435.

Janecke, S. U. & Evans, J. P. 1988. Feldspar-influenced rock rheologies. *Geology* **16**, 1064-1067.

Kerrich, R. 1986. Fluid infiltration into fault zones: Chemical, isotopic, and mechanical effects. *Pageoph.* **124**, 225-268.

LaPointe, P. R. 1988. A method to characterize fracture density and connectivity through fractal geometry. *Int. Jour. Rock Mech. Min. Sci., & Geomech. Abst.* **25**, 421-429.

Lockner, D., Hickman, S., Kuksenko, V., Ponomarev, A., Sidorin, A., Byerlee, J., & Khakaev, B. 1991. Laboratory-determined permeability of cores from the Kola superdeep well, USSR. *Geophys. Res. Lett.* **18**, 881-884.

Losh, S. 1989. Fluid-rock interaction in an evolving ductile shear zone and across the brittle-ductile transition, central Pyrenees, France. *Am. J. Sci.* **289**, 600-648.

Mandelbrot, B.B. 1982. *The Fractal Geometry of Nature.* W. H. Freeman and Co., New York.

Matsumoto, N., Yomogida, K. & Honda, S. 1992. Fractal analysis of fault systems in Japan and the Philippines. *Geophys. Res. Lett.* **19**, 357-360.

McCaig, A. M. 1988. Deep fluid circulation in fault zones. *Geology* **16**, 867-870.

Mitra, G. 1984. Brittle to ductile transition due to large strains along the White Rock thrust, Wind River Mountains, Wyoming. *J. Struct. Geol.* **6**, 51-61.

Mitra, G. & Frost, R. B. 1981. Mechanisms of deformation within Laramide and Precambrian deformation zones in basement rocks of the Wind River Mountains. *Cont. to Geol.* **19**, 161-173.

Mitra, G., Hull, J. M., Yonkee, W. A. & Protzman, G. M. 1988. Comparison of macroscopic and microscopic deformational styles in the Idaho-Wyoming thrust belt and the Rocky Mountain foreland. *Geol. Soc. Amer. Memoir 171* 119-130.

Montoya, J. W. & Hemley, J. J. 1975. Activity relations and stabilities in alkali feldspar and mica alteration reactions. *Econ. Geol.* **70**, 577-583.

Moore, J. C. 1989. Tectonics and hydrogeology of accretionary prisms. *J.Struct. Geol.* **11**, 95-106.

Moore J. C., Taira, A. & Moore, G. 1991. Ocean drilling and accretionary processes. *GSA Today* **1**, 265-269.

Morrow, C. A. & Byerlee, J. 1988. Permeability of rock samples from Cajon Pass, California. *Geophys. Res. Lett.* **15**, 1033-1036.

Morrow, C. A., Shi, L. Q. & Byerlee, J. 1984. Permeability of fault gouge under confining pressure and shear stress. *J. Geophys. Res.* **89**, 3193-3200.

O'Hara, K. 1988. Fluid flow and volume loss during mylonitization: An origin for phyllonite in an overthrust setting, North Carolina, U.S.A. *Tectonophysics* **156**, 21-36.

O'Hara, K. & Blackburn, W. H. 1989. Volume loss model for trace-element enrichment in mylonites. *Geology* **17**, 524-527.

Parry, W. T. & Bruhn, R. L. 1990. Fluid pressure transients on seismogenic normal faults. *Tectonophysics* **179**, 335-344.

Reynolds, S. J. & Lister, G. S. 1987. Structural aspects of fluid-rock interactions in detachment zones. *Geology* **15**, 362-366.

Richmond, G. M. 1945. Geology of northwestern end of the Wind River Mountains, Sublette County, Wyoming. U.S.G.S. Oil & Gas Investigation Prelim. Map 31.

Rimstidt, J. D. & Barnes, H. L. 1980. The kinetics of silica-water reactions. *Geochemica et Cosmochimica Acta* **44**, 1683-1699.

Sibson, R. H. 1981. Fluid-flow accompanying faulting: Field evidence and models. In: Earthquake prediction (edited by Simpson, D. W. & Richards, P. G.). *Am. Geophys. Un., Ewing Series monograph* 593-603.

Sibson, R. H. 1986. Brecciation processes in fault zones: Inferences from earthquake rupturing. *Pageoph* **124**, 159-175.

Sibson R. H. 1987. Earthquake rupturing as a mineralizing agent in hydrothermal systems. *Geology* **15**, 701-704.

Sibson, R. H. 1990. Faulting and Fluid Flow. Min. Assoc. Canada Short Course on Crustal Fluids, Handbook **18**, 95-132.

Sibson, R. H. 1991. Loading of faults to failure. *Bull. Seismological Soc. Amer.* **81**, 2493-2497.

Sibson, R. H. 1992. Fault-valve behavior and the hydrostatic-lithostatic fluid pressure interface. *Earth-Science Reviews* **32**, 141-144.

Sibson, R. H., Robert, F. & Poulsen, K. H. 1988. High-angle reverse faults, fluid pressure cycling and mesothermal gold-quartz deposits *Geology* **16**, 551-555.

Sinha, A. K., Hewitt, D. A. & Rimstidt, J. D. 1986. Fluid interaction and element mobility in the development of ultramylonites. *Geology* **14**, 833-886.

Sinha, A. K., Hewitt, D. A. & Rimstidt, J. D. 1988. Metamorphic petrology and strontium isotope geochemistry associated with development of mylonites: An example from the Brevard fault zone, North Carolina. *Amer. Jour. of Science* **288**, 115-147.

Sleep, N. H. & Blanpied, M. L. 1992. Creep, compaction, and the weak rheology of major faults. *Nature*, **359**, 687-692.

Starkey, H. C., Blackmon, P. D. & Hauff, P. L. 1984. The routine mineralogical analysis of clay-bearing samples. U.S. Geological Survey Bulletin 1563, 32.

Turcotte, D. L. 1986. Fractals and fragmentation. *J. Geophys. Res.* **91**, 1921-1926.

Velde, B. & Dubois, J. 1991. Fractal analysis of fractures in rocks: the Cantor's Dust method--Reply. *Tectonophysics* **198**, 113-115.

Velde, B., Dubois, J., Moore, D. & Touchard, G. 1991. Fractal Patterns of fractures in granites. *Earth and Planetary Sci. Lett.* **104**, 25-35.

Velde, B., Dubois, J., Touchard, G. & Badri, A. 1990. Fractal analysis of fractures in rocks: the Cantor's Dust method. *Tectonophysics* **179**, 345-352.

Vignes-Alder, M., Le Page, A. & Alder, P. 1991. Fractal analysis of fracturing in two African regions, from satellite imagery to ground scale. *Tectonophysics* **196**, 69-86.

Vocke, R. D., Hanson, G. N. & Grunenfelder, M. 1987. Rare Earth element mobility in the Roffna Gneiss. *Contrib. Min. Petr.* **95**, 145-154.

Walther, J. V. & Helgeson, H. C. 1977. Calculation of the thermodynamic properties of aqueous silica and the solubility of quartz and its polymorphs at high pressures and temperatures. *Am. J. Sci.* **277**, 1315-1351.

Winchester, J. A. & Max, M. D. 1984. Element mobility associated with syn-metamorphic shear zones near Scotchport, NW Mayo, Ireland. *J. Metamorphic Geol.* **2**, 1-11.

Wood, B. J. & Walther, J. V. 1986. Fluid flow during metamorphism and its implications for fluid-rock ratios. In: Fluid-rock interactions during metamorphism, Advances in physical geochemistry (edited by Wood, B. J. & Walther, J. V.). *Springer-Verlag New York Inc.* **5**, 89-108.

APPENDIX

APPENDIX. RESULTS OF LINEAR FRACTAL ANALYSIS

Results of linear fractal analysis illustrating fracture trace maps, fracture orientation histograms, and fractal vector plots for hand samples and thin sections.

a

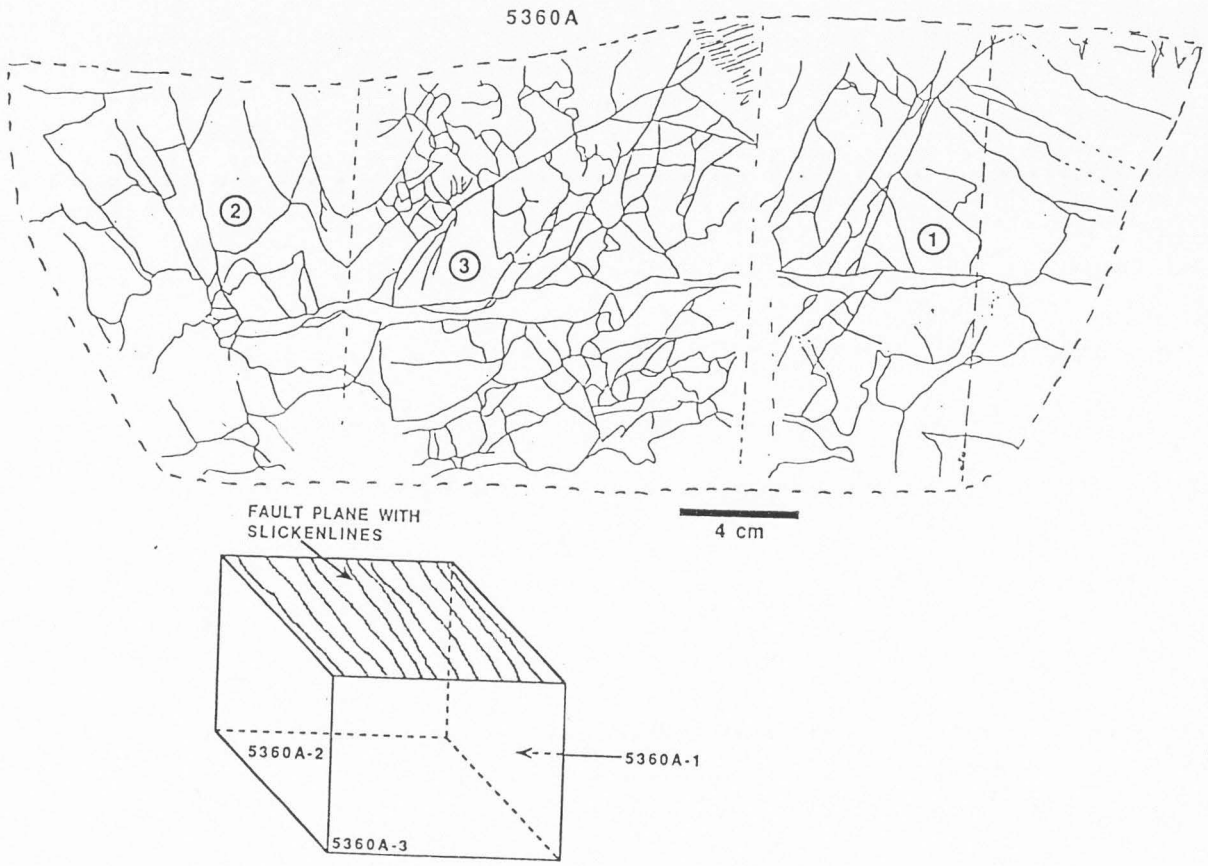

Fig. 39. Fracture trace maps, statistical, and fractal results for hand sample 5360A of the damaged zone adjacent to a gouge/cataclasite zone in the East Fork fault. (**a**) Line drawings of fractures from faces slabbed parallel to slip direction and perpendicular to the fault plane (5360A-1 & 5360A-2) and faces slabbed perpendicular to slip direction and perpendicular to the fault plane (5360A-3). Fractures are mainly transgranular with interspersed intragranular fractures. (**b**) Orientation frequency histograms for fracture trace maps for Sample 5360A. (**c**) Fractal ellipses for fracture trace maps of sample 5360A. Fractal dimensions are listed in parentheses below the orientation of the analysis line. (**d**) Normalized fractal ellipses for fracture trace maps of sample 5360A. Normalized fractal dimensions are listed in parentheses below the orientation of the analysis line. For the most part, dimensions are greater at high angles to the fault, suggesting uniform fracture clustering and higher fracture densities in angles subparallel to the fault. Remember that the analysis line measures fractures that mostly intersect the line at a high angle. These results correlate with orientation distributions and visual comparison with the trace maps suggesting credibility of the method.

Fig. 39. (continued).

b

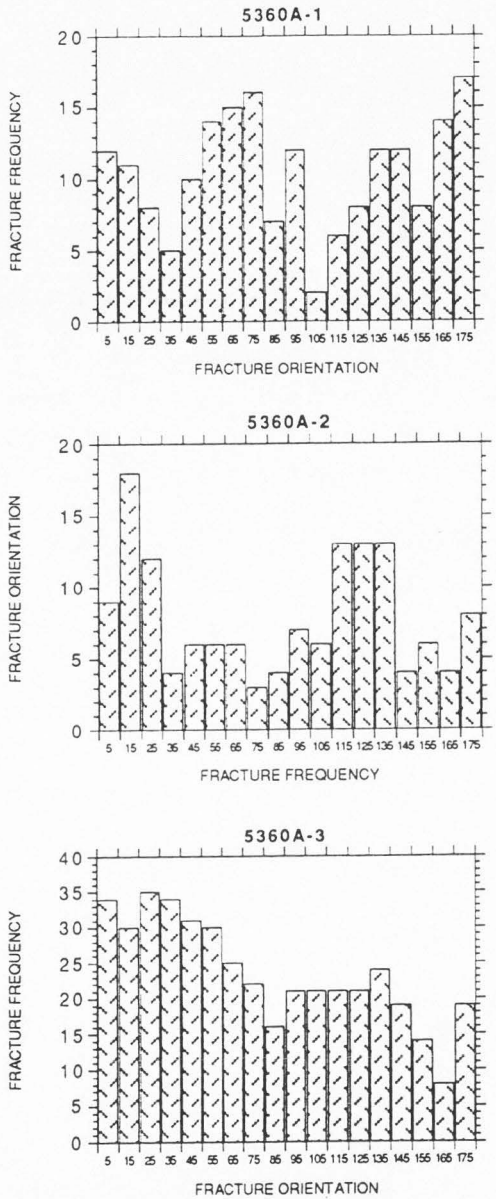

Fig. 39. (continued).

c

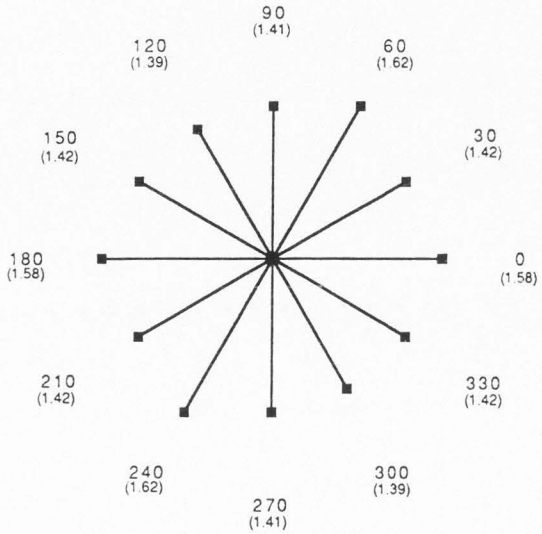

5360A1 Fractal Ellipse

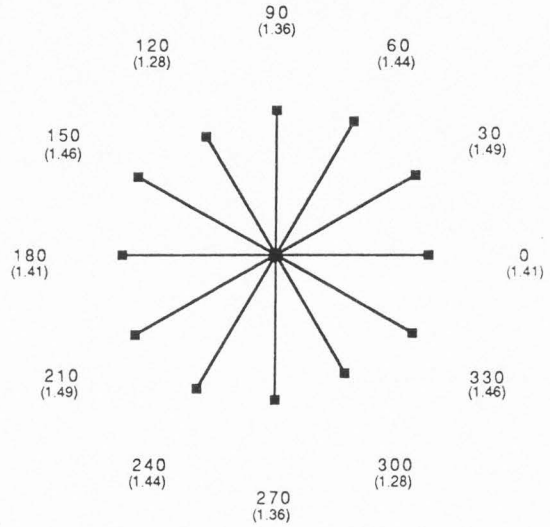

5360A2 Fractal Ellipse

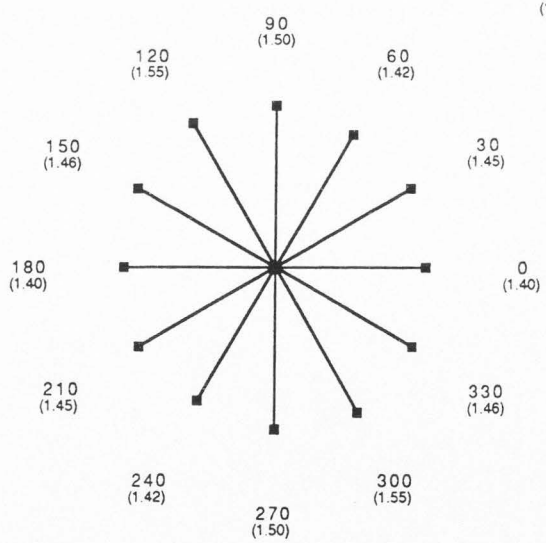

5360A3 Fractal Ellipse

Fig. 39. (continued).

d

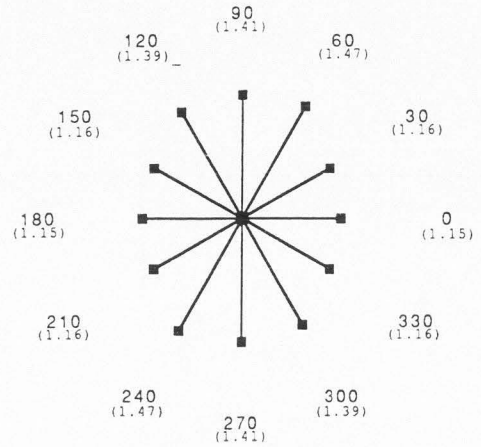

5360A1 Normalized Ellipse

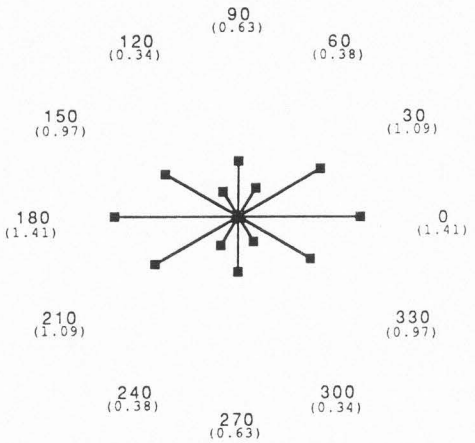

5360A2 Normalized Ellipse

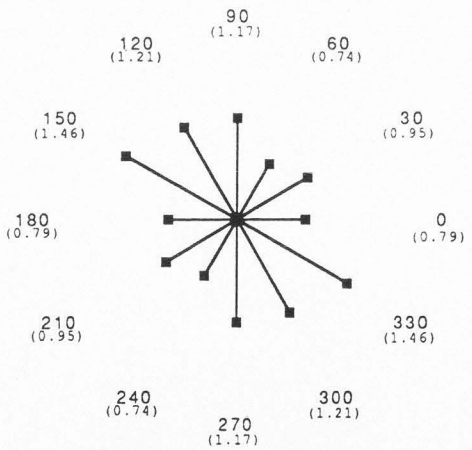

5360A3 Normalized Ellipse

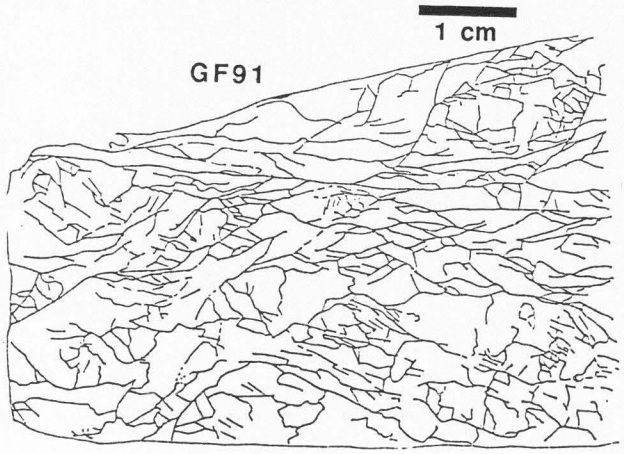

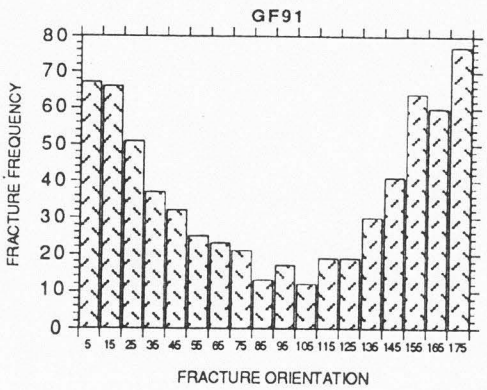

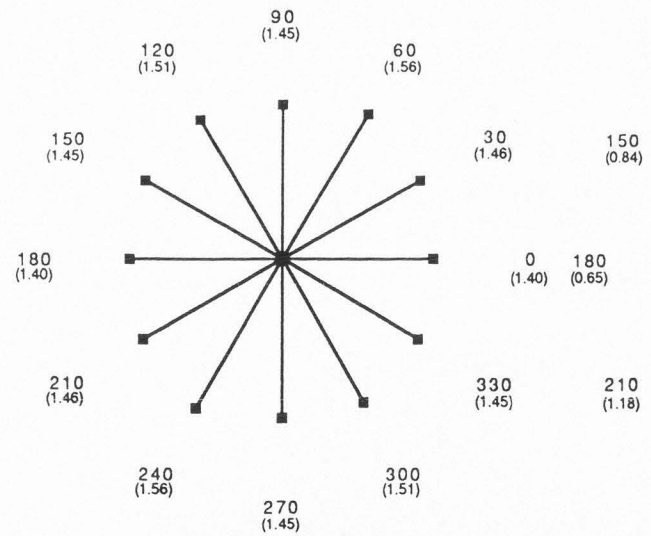

GF91 Fractal Ellipse

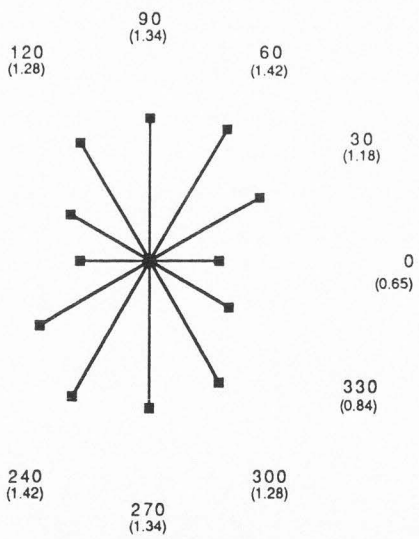

GF91 Normalized Ellipse

Fig. 40. Fracture trace map, orientation frequency histogram, fractal ellipse, and normalized fractal ellipse for thin section sample GF91. Map face slabbed parallel to slip direction and perpendicular to the fault plane in the East Fork damaged zone adjacent to a gouge/cataclasite zone. Fractures are transgranular that, in turn, connect zones of intragranular fractures.

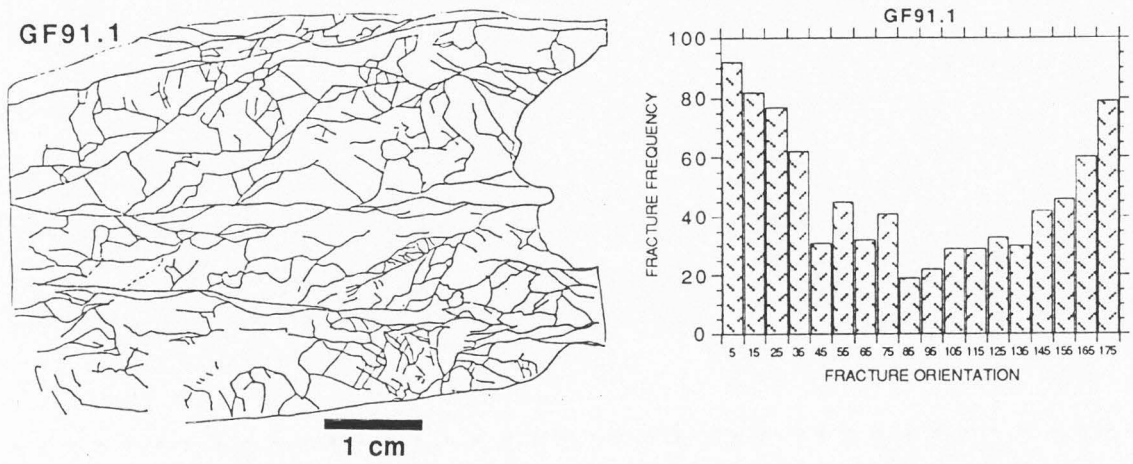

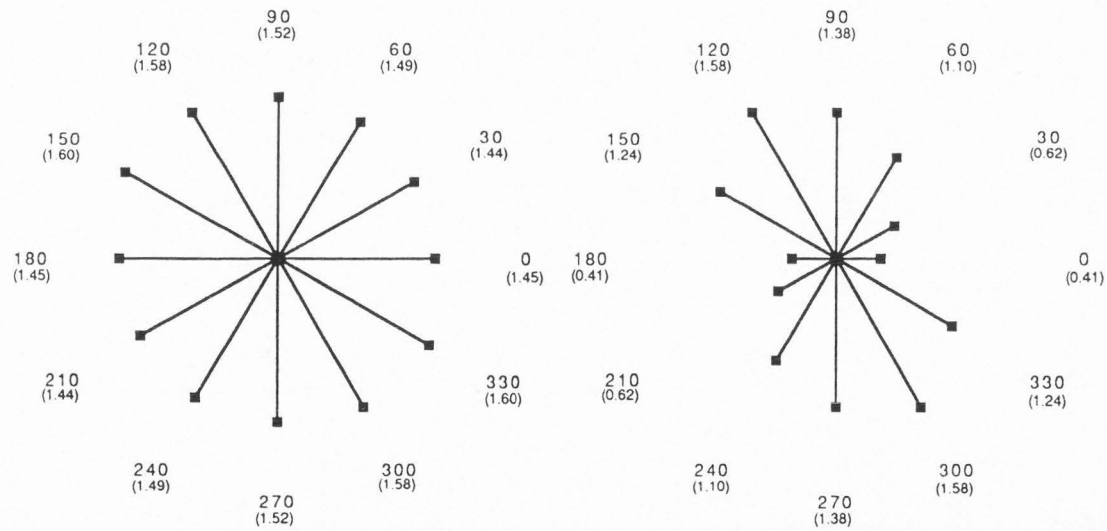

GF91.1 Fractal Ellipse

GF91.1 Normalized Ellipse

Fig. 41. Fracture trace map, orientation frequency histogram, fractal ellipse, and normalized fractal ellipse for thin section sample GF91.1. Map face slabbed parallel to slip direction and perpendicular to the fault plane in the East Fork damaged zone adjacent to a gouge/cataclasite zone. Fractures are transgranular that, in turn, connect zones of intragranular fractures.

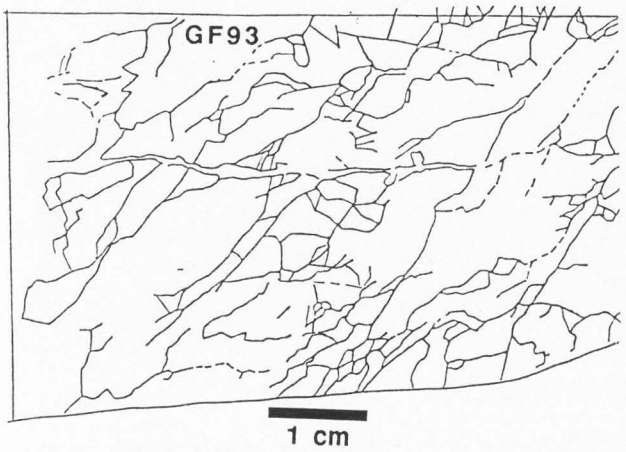

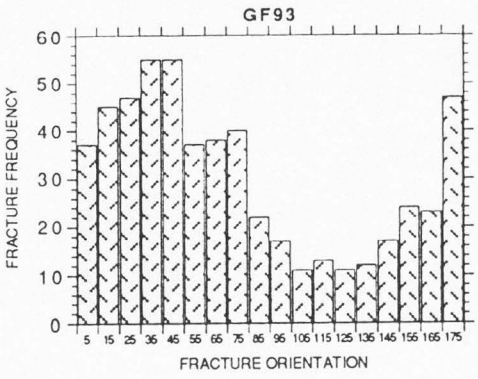

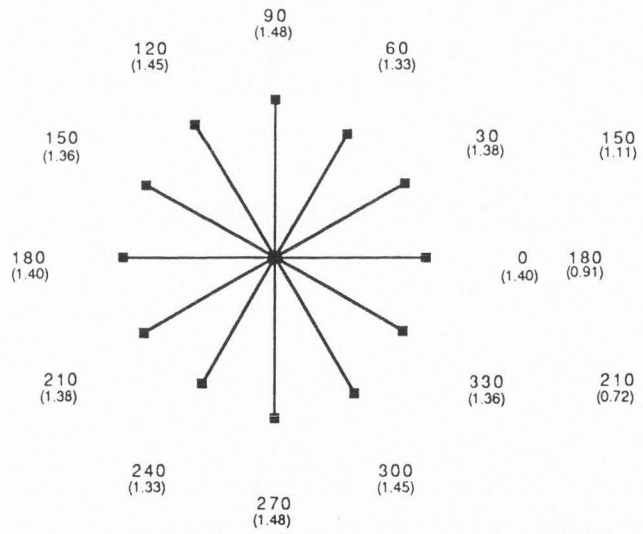

GF93 Fractal Ellipse

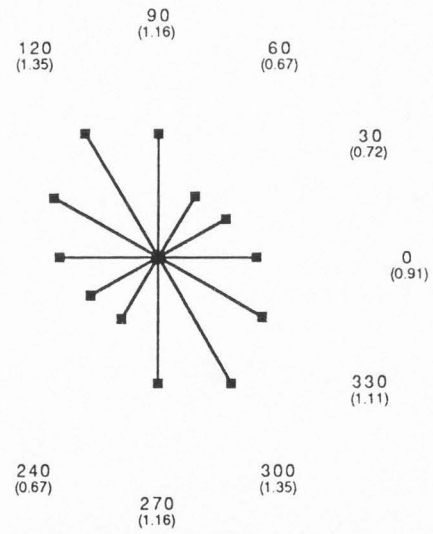

GF93 Normalized Ellipse

Fig. 42. Fracture trace map, orientation frequency histogram, fractal ellipse, and normalized fractal ellipse for thin section sample GF93. Map face slabbed parallel to slip direction and perpendicular to the fault plane in the East Fork damaged zone adjacent to a gouge/cataclasite zone. Fractures are transgranular that, in turn, connect zones of intragranular fractures.

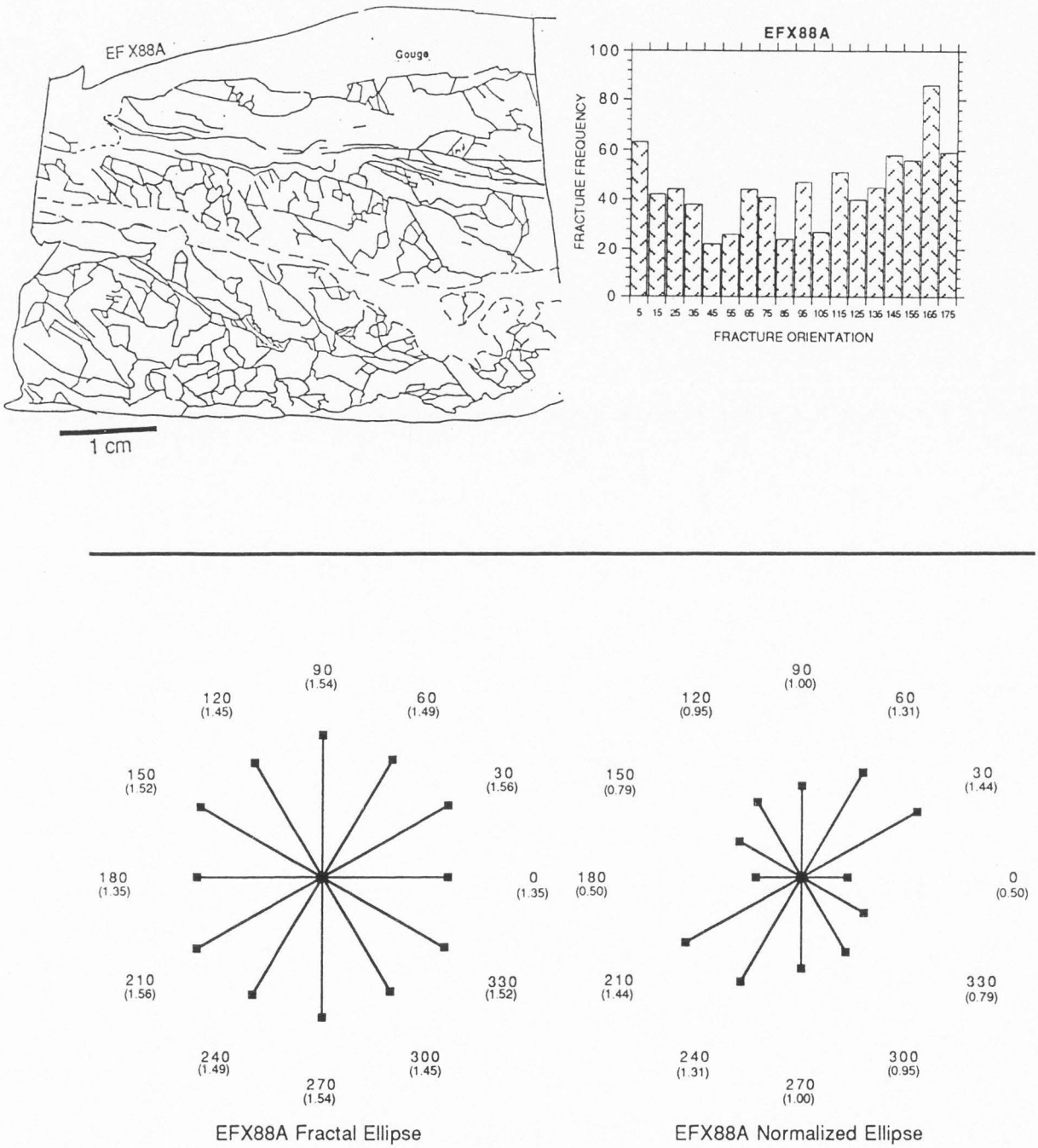

Fig. 43. Fracture trace map, orientation frequency histogram, fractal ellipse, and normalized fractal ellipse for thin section sample EFX88A. Map face slabbed perpendicular to slip direction and perpendicular to the fault plane in the East Fork damaged zone adjacent to a gouge/cataclasite zone. Fractures are transgranular that, in turn, connect zones of intragranular fractures.

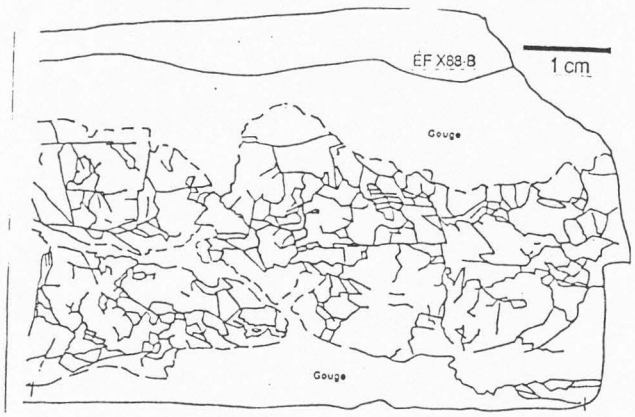

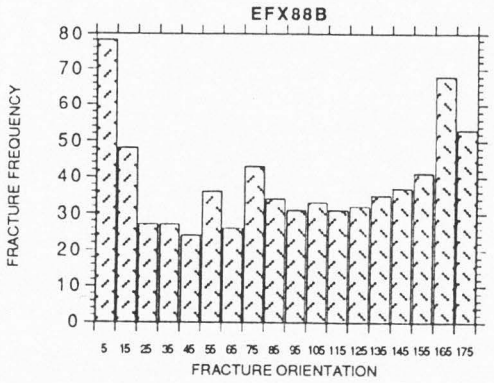

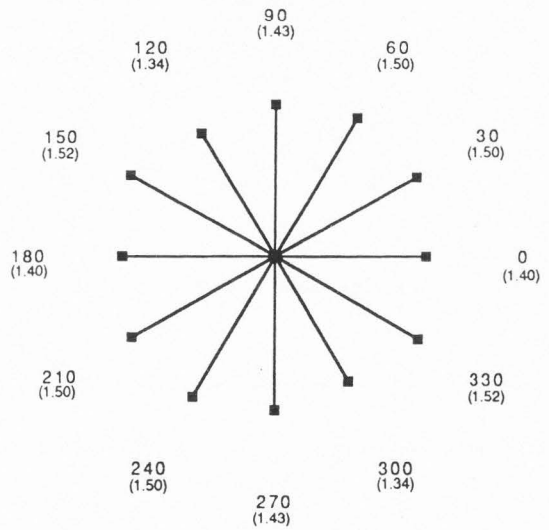

EFX88B Fractal Ellipse

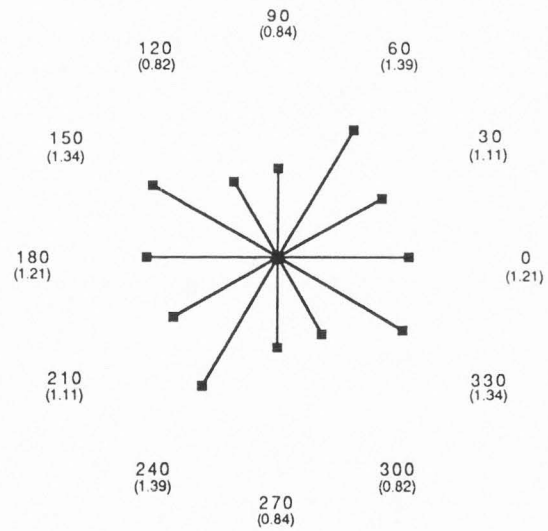

EFX88B Normalized Ellipse

Fig. 44. Fracture trace map, orientation frequency histogram, fractal ellipse, and normalized fractal ellipse for thin section sample EFX88B. Map face slabbed perpendicular to slip direction and perpendicular to the fault plane in the East Fork damaged zone adjacent to a gouge/cataclasite zone. Fractures are transgranular that, in turn, connect zones of intragranular fractures.